

# Sinter-Infiltration of Ti-6Al-4V

by  
Preyin Govender

*Thesis presented in partial fulfilment of the requirements for the  
degree of Master of Engineering (Mechanical) in the Faculty of  
Engineering at Stellenbosch University*



Supervisor: Prof. DC Blaine

March 2020

“The financial assistance of the CSIR-DST Inter-Programme Bursary (IBS) Scholarship towards this research is hereby acknowledged. Opinions expressed and conclusions arrived at, are those of the author and are not necessarily to be attributed to the CSIR-DST Inter-Programme Bursary (IBS) Scholarship”

## Declaration

By submitting this thesis electronically, I declare that the entirety of the work contained therein is my own, original work, that I am the sole author thereof (save to the extent explicitly otherwise stated), that reproduction and publication thereof by Stellenbosch University will not infringe any third party rights and that I have not previously in its entirety or in part submitted it for obtaining any qualification.

Initials and Surname : P. Govender  
Date : March 2020  
Signature : .....

## Abstract

Ti-6Al-4V is a widely used titanium alloy within the aerospace and medical industry with powder metallurgy (PM) becoming a fast growing industry within. The press-and-sinter technique is one such PM process that can be used to manufacture parts. In order to improve mechanical properties, dimensional tolerances and machinability, ferrous PM press-and-sintered parts are often infiltrated with molten Cu during the sintering heat treatment process. This project investigates the feasibility of infiltrating sintered Ti-6Al-4V compacts with molten Al, in order to improve its properties.

Two Ti-6Al-4V powder blends were mixed, namely a blended elemental (BE) blend consisting of elemental Ti, Al and V powder in a 90:6:4 wt% ratios and a master alloy (CPTi+MA) blend consisting of commercially pure Ti (CPTi) powder with a master alloy (MA) powder of Al and V mixed in a 90:10 wt% ratio. These powder blends were compacted in  $\varnothing 10$  mm right cylinders with a relative green density ( $\rho_g$ ) of approximately 75%. The compacts were sintered under high vacuum at temperatures of 1100 °C and 1200 °C, respectively, to achieve relative sintered densities ( $\rho_s$ ) of < 92%. At  $\rho_s > 92\%$ , open pore channels close off preventing infiltration. Infiltration disks were compacted from pure Al spherical powder. The mass of the disks was calculated by taking the residual porosity of the sintered Ti-6Al-4V compacts, and providing enough molten Al to infiltrate the pores exactly. Infiltration took place under a nitrogen atmosphere at various temperatures between 700 °C - 900 °C, above Al melting point (660.6 °C) to ensure melting, and for various dwell times. Slices of wrought Al bar stock were also evaluated for infiltration. Neither the Al powder compacts nor the wrought Al slices melted, with the result that all attempts to infiltrate the Ti-6Al-4V with Al failed.

Characterization of the sintered and infiltrated samples was performed. Optical microscopy as well as energy dispersive X-ray spectroscopy (EDS) analysis was used to view the microstructures and elemental distribution in the microstructures, respectively. From these analyses, it was confirmed that infiltration with Al did not occur for any of the samples. CPTi+MA samples showed, on average a change in relative density from 74.5% to 90.2%, while BE samples showed negligible change from 73.6% to 74.9% relative density. The microstructure of both blends were observed with the CPTi+MA having a  $\alpha+\beta$  microstructure; while the BE having a predominantly  $\alpha$ -microstructure.

EDS imaging for the CPTi+MA samples showed a fairly homogenous elemental distribution for both sintering temperatures. The BE blends showed an inhomogenous distribution at both sintering temperatures. Large pores were visible as Al particles melted and diffused into Ti and V, leaving high Al concentrations surrounding the pores. The results indicate that Ti and V diffuse into the Al disks during the infiltration heat treatment process, raising the melting

temperature of the Al disks. By observing the concentration of Ti in Al disks, we see on the Ti-Al phase diagram that an intermetallic may have formed, thus increasing the melting temperature above the temperatures used for infiltration.

## Abstrak

Ti-6Al-4V is 'n titanium alloori wat gereeld gebruik word in die ruimtevaart- en mediese- bedryf, met poeiermetallurgie (PM) wat 'n groeiende industrie daarin is. Een proses om PM komponente te vervaardig is die pers-en-sinter tegniek. Meganiese eienskappe, afmetingstoleransies en masjienbaarheid van ysteralloori pers-en-sinter onderdele word gereeld verbeter deur dit met gesmelte Cu te infiltreer gedurende die sintersproses. Die projek ondersoek die haalbaarheid om sinter Ti-6Al-4V te infiltreer met Al, om eienskappe te verbeter.

Twee Ti-6Al-4V poeiermengsels is gemeng, spesifiek 'n gemengde elementêre (BE) mengsel, wat uit Ti, Al, en V poeiers in 'n 90:6:4 gewigspersentasie verhouding bestaan, en 'n meesteralloori (CPTi+MA) mengsel van 'n suiwer Ti (CPTi) poeier en 'n meester alloori (MA) poeier van Al en V, wat in 'n 90:10 gewigspersentasie verhouding gemeng word. Hierdie poeiermengsels is in  $\varnothing 10$  mm reghoekige silinders gepers tot 'n relatiewe groen digtheid ( $\rho_g$ ) van ongeveer 75%. Die gepersde silinders is onder hoë vakuum by temperature van 1100 °C en 1200 °C, onderskeidelik, gesinter tot 'n relatiewe sinterdigtheid ( $\rho_s$ ) van < 92%. By  $\rho_s > 92\%$  word oop porie kanale afgesluit en dus is infiltrasie onmoontlik.

Infiltrasie skywe is uit suiwer Al sferiese poeier gepers. Massa van skywe is bereken deur oorblywende porositeit van die gesinterde Ti-6Al-4V silinders te vat en dan net genoeg gesmelte Al te gebruik om hul porieë presies te infiltreer. Infiltrasie het onder 'n stikstof atmosfeer plaasgevind by verskillende woontye, en verskeie temperature (700 °C - 900 °C), wat bo Al se smeltpunt (660.6 °C) is, om smelting te verseker. Snye van gesmeede Al staafvoorraad was ook vir infiltrasie geëvalueer. Nie die Al poeier of die gesmeede Al skywe het gesmelt nie, en gevolglik was alle pogings om Ti-6Al-4V te infiltreer onsuksesvol.

Die gesinterde en geïnfiltreerde monsters is gekarakteriseer. Optiese mikroskopie en 'n energiedispergerende X-straalspektroskopie (EDS) analise is gebruik om mikrostrukture en elementêre samestelling daarvan waar te neem. Analises het bevestig dat infiltrasie met Al nie voorgekom het in enige van die monsters nie. CPTi+MA monsters toon 'n gemiddelde verandering in relatiewe digtheid van 74.5% na 90.2% terwyl BE monsters se relatiewe digtheid toon weglaatbare verandering vanaf 73.6% na 74.9%. Mikrostrukture van beide poeiermengsels is waargeneem, waar CPTi+MA 'n  $\alpha+\beta$ -mikrostruktuur, en BE hoofsaaklik 'n  $\alpha$ -mikrostruktuur getoon het.

EDS beelding vir die CPTi+MA monsters het redelike homogene elementêre verspreiding getoon vir beide sinter temperature. BE monsters het nie homogene verspreiding getoon nie. Groot porieë was sigbaar, aangesien Al partikels gesmelt en in die Ti en V gediffundeer het, wat porieë wat met hoë konsentrasies Al omring word gelos het. Die resultate dui aan dat Ti en V in die Al skywe diffundeer gedurende die infiltrasie hittebehandelingsproses, wat die smeltpunt van Al skywe verhoog. Deur die gewigsverhoudingspersentasie van die Ti in die Al skywe waar te neem, sien ons op Ti-Al fasesdiagramme dat intermetaalverbindinge dalk gevorm het, wat smeltpunte bo die infiltrasietemperature verhoog.

## Acknowledgements

I would like to thank my family and friends for their continuous support and encouragement in these past few years.

I would also like to thank my supervisor, Dr. DC Blaine for her guidance and support throughout my undergraduate and post graduate studies. You have been a true mentor.

I would lastly like to thank the students and staff within the CAF, materials laboratory as well as administration staff of Stellenbosch University of whom helped me throughout my studies and made this project possible.

# Table of contents

	<b>Page</b>
<b>Declaration .....</b>	<b>i</b>
<b>Abstract.....</b>	<b>ii</b>
<b>Abstrak .....</b>	<b>iv</b>
<b>Acknowledgements .....</b>	<b>vi</b>
<b>Table of contents .....</b>	<b>vii</b>
<b>List of figures.....</b>	<b>x</b>
<b>List of tables .....</b>	<b>xiv</b>
<b>Nomenclature .....</b>	<b>xv</b>
<b>1 Introduction.....</b>	<b>1</b>
1.1 Background .....	1
1.2 Objectives.....	2
1.3 Motivation .....	3
1.4 Limitations .....	3
1.5 Hypothesis.....	4
<b>2 Literature Review .....</b>	<b>4</b>
2.1 Titanium and titanium alloys.....	4
2.1.1 Structures and Properties .....	4
2.1.2 Titanium in Industry .....	6
2.2 Phase Diagrams and Diffusivity.....	7
2.2.1 Ti-6Al-4V .....	7
2.2.2 Aluminium-Vanadium (Master alloy).....	8
2.2.3 Titanium-Aluminium.....	9
2.2.4 Titanium-Vanadium .....	11
2.2.5 (Titanium, Aluminium, Vanadium)-Nitrogen .....	11
2.3 Titanium Powder Metallurgy .....	13
2.3.1 Powder Metallurgy Techniques and Processes .....	13
2.3.2 Titanium Alloy Powder Metallurgy Processes.....	15
2.3.3 Advantages and Disadvantages of Titanium and Titanium alloys Powder Metallurgy .....	15
2.4 Sintering Process .....	16



2.4.1	General Sintering.....	16
2.4.2	Titanium and Ti-6Al-4V Sintering.....	17
2.4.3	Aluminium Sintering (During Infiltration Heat Treatment).....	18
2.5	Infiltration Heat Treatment Process .....	19
2.5.1	General Infiltration .....	19
2.5.2	Contact Angles .....	20
2.6	Al Infiltration with Ti and Ti Preforms .....	21
<b>3</b>	<b>Design of Experiments.....</b>	<b>23</b>
3.1	Materials.....	23
3.2	Compaction Process .....	24
3.3	Heat Treatment (Sintering).....	24
3.4	Infiltration Heat Treatment Process .....	25
3.5	Preparation of Samples.....	28
3.5.1	Cutting .....	28
3.5.2	Hot Mount .....	28
3.5.3	Grinding and Polishing.....	28
3.6	Characterization .....	29
3.6.1	Optical Microscopy (OM) .....	29
3.6.2	Scanning Electron Microscopy (SEM).....	29
3.6.3	Energy Dispersive X-Ray Spectroscopy (EDS).....	29
<b>4</b>	<b>Results.....</b>	<b>30</b>
4.1	Vacuum Sinter.....	30
4.2	Infiltration Heat Treatment.....	32
4.3	Microstructural Characterisation.....	33
4.3.1	Sintered samples (BE & CPTi+MA).....	33
4.3.2	1100 °C Sintered and 700 °C Infiltrated Samples (BE and CPTi+MA, Powder Al Compact).....	37
4.3.3	1100 °C Sintered and 750 °C Infiltrated Samples (BE and CPTi+MA, Powder Al Compact).....	41
4.3.4	1200 °C Sintered and 750 °C Infiltrated Samples (BE and CPTi+MA, Wrought Al Disk).....	45
4.3.5	1200 °C Sintered and 900 °C Infiltrated Samples (BE and CPTi+MA, Wrought Al Disk).....	49
4.3.6	1100 °C Sintered and 900 °C Infiltrated Samples (BE and CPTi+MA, Wrought Al Disk).....	53
4.3.7	1100 °C Sintered and 900 °C Infiltrated Samples (BE and CPTi+MA, Powder Al Compact).....	59
4.3.8	1100 °C Sintered and 1150 °C Infiltrated Samples (BE and CPTi+MA, Cu Disk) .....	63
4.3.9	Diffusion Graphs .....	68
4.3.10	Micro Structures of Un-infiltrated Sintered Samples.....	70
4.3.11	SEM Images .....	71

4.3.12 Crack Propagations.....	73
<b>5 Discussion of Results.....</b>	<b>74</b>
<b>6 Conclusion .....</b>	<b>77</b>
<b>7 References.....</b>	<b>80</b>
<b>Appendix A: Sintering and Infiltration Parameters and Results.....</b>	<b>86</b>
<b>Appendix B: Microstructures .....</b>	<b>87</b>
<b>Appendix C: Diffusion graphs .....</b>	<b>92</b>

## List of figures

	<b>Page</b>
Figure 1: Specific strengths against temperatures of various metals including titanium and titanium alloys (Kobelco, 2015) .....	6
Figure 2: Ti-Al-V ternary phase diagram at 600 °C (Raghaven, V., 2012).....	7
Figure 3: Ti-Al-V ternary phase diagram at 1200 °C (Raghaven, V., 2012).....	8
Figure 4: Aluminium-Vanadium binary phase diagram (Okamoto, H., 2012).....	9
Figure 5: Adapted Titanium-Aluminium binary phase diagram (Schuster, J.C., <i>et al</i> 2006) .....	9
Figure 6: Enhanced image of Titanium-Aluminium phase diagram (Schuster, J.C., <i>et al</i> 2006) .....	10
Figure 7: Phase diagram of Titanium-Vanadium (Saunders, 1990) .....	11
Figure 8: Aluminium-Nitrogen binary phase diagram (Pierson, H.O., 1996:201) .	11
Figure 9: Titanium-Nitrogen binary phase diagram (Skulev, H., 2014:57) .....	12
Figure 10: Vanadium-Nitrogen binary phase diagram (Pierson, H.O., 1996: 202) .....	13
Figure 11: Recreated basic process of powder injection moulding (Alcock.J et al, 1996) .....	14
Figure 12: Recreated flow diagram of the process involving sintering (Joong.S et al, 2007) .....	16
Figure 13: Transitional sintering states on a phase diagram (Joong.S <i>et al</i> , 2007)	17
Figure 14: a) Solid state and b) liquid state sintering (Joong.S <i>et al</i> , 2007).....	17
Figure 15: Ternary phase diagram showing diffusion paths at 1100 °C and various dwell times (Xu <i>et al</i> . 2014:994) .....	18
Figure 16: Samples infiltrated under a) nitrogen and b) vacuum at 658 °C (Yu.P, Schaffer.GB, 2008:163) .....	20
Figure 17: Contact angles (Smith. SM, <i>et al.</i> , 2014:2) .....	21
Figure 18: CFD analysis of nitrogen through tube furnace before (top) and after (bottom).....	27
Figure 19: Schematic representing the analyses of a pore with an electron beam	30
Figure 20: EDS map CPTi+MA 1100 °C vacuum sintered, unfiltered .....	34
Figure 21: EDS map BE 1100 °C vacuum sintered, unfiltered .....	35
Figure 22: EDS map CPTi+MA 1200 °C vacuum sintered, unfiltered .....	36

Figure 23: EDS map BE 1200 °C vacuum sintered, uninfiltreated .....	36
Figure 24: EDS map CPTi+MA 1100 °C sintered, 700 °C infiltration heat treatment, no dwell.....	38
Figure 25: EDS line distribution through pore of CPTi+MA, 700 °C infiltration heat treatment, no dwell .....	39
Figure 26: EDS map BE 1100 °C sintered, 700 °C infiltration heat treatment, no dwell.....	40
Figure 27: EDS line distribution through pore of BE, 700 °C infiltration heat treatment, no dwell.....	41
Figure 28: EDS map CPTi+MA 1100 °C sintered, 750 °C infiltration heat treatment, 1 hr dwell .....	42
Figure 29: EDS line distribution through pore of CPTi+MA 1100 °C sintered, 750 °C infiltration heat treatment, 1 hr dwell .....	43
Figure 30: EDS map BE 1100 °C sintered, 750 °C infiltration heat treatment, 1 hr dwell.....	44
Figure 31: EDS line distribution through pore of BE 1100 °C sintered, 750 °C infiltration heat treatment, 1 hr dwell .....	45
Figure 32: EDS map CPTi+MA 1200 °C sintered, 750 °C infiltration heat treatment, 1 hr dwell .....	46
Figure 33: EDS line distribution through pore of CPTi+MA 1200 °C sintered, 750 °C infiltration heat treatment, 1 hr dwell .....	47
Figure 34: EDS map BE 1200 °C sintered, 750 °C infiltration heat treatment, 1 hr dwell.....	48
Figure 35: EDS line distribution through pore of BE 1200 °C sintered, 750 °C infiltration heat treatment, 1 hr dwell .....	49
Figure 36: EDS map CPTi+MA 1200 °C sintered, 900 °C infiltration heat treatment, 1 hr dwell .....	50
Figure 37: EDS line distribution through pore of CPTi+MA 1200 °C sintered, 900 °C infiltration heat treatment, 1 hr dwell .....	51
Figure 38: EDS map BE 1200 °C sintered, 900 °C infiltration heat treatment, 1 hr dwell.....	52
Figure 39: EDS line distribution through pore of BE 1200 °C sintered, 900 °C infiltration heat treatment, 1 hr dwell .....	53
Figure 40: EDS map CPTi+MA 1100 °C sintered, 900 °C infiltration heat treatment, 1 hr dwell .....	54
Figure 41: EDS line distribution through pore of CPTi+MA 1100 °C sintered, 900 °C infiltration heat treatment, 1 hr dwell .....	55

Figure 42: EDS map CPTi+MA Al disk, 900 °C infiltration heat treatment, 1 hr dwell.....	55
Figure 43: EDS map BE 1100 °C sintered, 900 °C infiltration heat treatment, 1 hr dwell.....	57
Figure 44: EDS line distribution through pore of BE 1100 °C sintered, 900 °C infiltration heat treatment, 1 hr dwell .....	58
Figure 45: EDS map BE Al disk, 900 °C infiltration heat treatment, 1 hr dwell ..	58
Figure 46: EDS map CPTi+MA 1100 °C sintered, 900 °C infiltration heat treatment, 1 hr dwell .....	60
Figure 47: EDS line distribution through pore of CPTi+MA 1100 °C sintered, 900 °C infiltration heat treatment, 1 hr dwell .....	61
Figure 48: EDS map BE 1100 °C sintered, 900 °C infiltration heat treatment, 1 hr dwell.....	62
Figure 49: EDS line distribution through pore of BE 1100 °C sintered, 900 °C infiltration heat treatment, 1 hr dwell .....	63
Figure 50: EDS map CPTi+MA 1100 °C sintered, 1150 °C infiltration heat treatment, 1 hr dwell .....	64
Figure 51: EDS map CPTi+MA 1100 °C sintered with Cu disk, 1150 °C infiltration heat treatment, 1 hr dwell .....	65
Figure 52: EDS line distribution through pore of CPTi+MA 1100 °C sintered, 1150 °C infiltration heat treatment, 1 hr dwell .....	66
Figure 53: EDS map BE 1100 °C sintered, 1150 °C infiltration heat treatment, 1 hr dwell .....	67
Figure 54: EDS line distribution through pore of BE 1100 °C sintered, 1150 °C infiltration heat treatment, 1 hr dwell .....	68
Figure 55: Diffusion graph of MA sample after infiltration at 900 °C, 1 hr dwell, sintered at 1100 °C.....	69
Figure 56: Micro structure of BE sample (1100 °C) .....	70
Figure 57: Micro structure of CPTi+MA sample (1100 °C) .....	70
Figure 58: Micro structure of BE sample (1200 °C) .....	71
Figure 59: Micro structure of CPTi+MA sample (1200 °C) .....	71
Figure 60: SEM image wrought Al disk before infiltration.....	72
Figure 61: SEM image Al powder compact after infiltration.....	72
Figure 62: No infiltration disk (1100 °C sintered): Etched CPTi+MA images (top left and top right) and etched BE images (bottom left) with etched Al disk image (bottom right).....	87

Figure 63: Al powder compact (1100 °C sintered): Etched CPTi+MA images (top left and top right) and etched BE image (bottom left) with etched Al disk image (bottom right).....	87
Figure 64: Al powder compact (1100 °C sintered): CPTi+MA etched image (top left) and Al disk (top right). BE etched image (bottom left) and Al disk (bottom right) .....	88
Figure 65: No infiltration disk (1200 °C sintered): CPTi+MA etched image (top left and right) and BE etched images (bottom left and right) .....	88
Figure 66: Wrought Al disk (1200 °C sintered): CPTi+MA image (top left) and etch image (top right) and BE image (bottom left) and etched image (bottom right) .....	89
Figure 67: Wrought Al disk (1200 °C sintered): CPTi+MA etched images (top left and right) with BE etched images (bottom left and right) .....	89
Figure 68: Wrought Al disk (1100 °C sintered): CPTi+MA image (top left) and etched image (top right) with BE image (bottom left) and etched image (bottom right) .....	90
Figure 69: Wrought Al disk (1100 °C sintered): CPTi+MA image (top left) and etched image (top right) with BE image (bottom left) and etched image (bottom right) .....	90
Figure 70: Cu infiltrated (1100 °C sintered): CPTi+MA image (top left) and etched image (top right) with BE image (bottom left) with etched image (bottom right) .....	91
Figure 71: Diffusion graph of BE sample after infiltration at 900 °C sintered at 1200 °C .....	92
Figure 72: Diffusion graph of BE sample after infiltration at 900 °C sintered at 1200 °C .....	92
Figure 73: Diffusion graph of BE sample after infiltration at 900 °C sintered at 1100 °C .....	93
Figure 74: Diffusion graph of BE sample after infiltration at 900 °C sintered at 1100 °C .....	93
Figure 75: Diffusion graph of BE sample after infiltration at 900 °C sintered at 1100 °C .....	94
Figure 76: Diffusion graph of MA sample after infiltration at 900 °C sintered at 1200 °C .....	94
Figure 77: Diffusion graph of MA sample after infiltration at 900 °C sintered at 1200 °C .....	95
Figure 78: Diffusion graph of MA sample after infiltration at 900 °C sintered at 1100 °C .....	95

## List of tables

	<b>Page</b>
Table 1: Basic material properties titanium (ASM Aerospace Specification Metals Inc., [S.a]) .....	5
Table 2: Contact angle and wetting (Khandekar et al., 2010) .....	21
Table 3: Materials specifications .....	23
Table 4: Vacuum Sinter Pump Components.....	25
Table 5: Green and Sintered densities .....	31
Table 6: Infiltration parameters with corresponding Al melt results.....	33
Table 7: Vacuum Sintered results and infiltration parameters .....	86

# Nomenclature

$\alpha$	Alpha Phase
$\beta$	Beta Phase
$\rho_g$	Green Density
$\rho_s$	Sintered Density
Al	Aluminium
BE	Blended Elemental
CPTi	Commercially Pure Titanium
Cu	Copper
MA	Master Alloy
PM	Powder Metallurgy
Ti	Titanium
Ti-6Al-4V	Titanium Alloy
Wt %	Weight percentage
V	Vanadium



# 1 Introduction

This chapter provides the background to the study, in terms of sinter infiltration and how it may have application for the common titanium alloy, Ti-6Al-4V. It presents the motivation and objectives, as well as the limitations of this investigation. It concludes with the hypothesis that will be tested through this study.

## 1.1 Background

Titanium, compared to steel and other elements, is a low density metal (almost half that of steel) with very good corrosion resistance and high temperature properties, and as such, its alloys (with Ti-6Al-4V being the most common) are commonly used in the aerospace, automotive, chemical industry and medical industries, where these properties are required (Anir, A., et al, 2017 & Xu, X., et al, 2013 & Froes, F.H., 2013). Grade 5 titanium, commonly known as Ti-6Al-4V, is the workhorse titanium alloy and consists of the large majority of the titanium manufacturing industry (Liu & Shin, 2019). Typically, wrought Ti-6Al-4V is produced by an expensive and energy-intensive process, involving numerous chemical extraction and mechanical forming techniques (Vladmir, A.J., et al, 2008). Powder metallurgy (PM) has been explored as a viable manufacturing route for titanium and its alloys for the past few decades with the hope that, with its energy and material efficient profile, it will offer a more cost effective solution (Chunxiang, C., et al, 2011). PM Ti-6Al-4V produced from prealloyed Ti-6Al-4V powders currently produced for industry is generally a very expensive process which involves post treatments in order to achieve the required sintered densities (casting, forging, machining); it does not offer significant advantages over wrought Ti-6Al-4V except in materials saving or additive manufacturing advantages. These sintered alloys are then typically subjected to hot isostatic pressing (HIP) or other methods of hot deformation which then complicates the manufacturing process and substantially increases the costs involved which offsets the advantages of the PM processes (Ivasishin, O.M., et al, 2002 & Ye, B., et al, 2011 & Xu, X., et al, 2013).

An alternative method to produce these alloys is through the blended elemental (BE) process, by either using stoichiometric mixtures of elemental powders, or a combination through the master alloy (MA) blend process, where a 60:40 Al:V master alloy powder with CPTi is mixed with commercially pure titanium powder (CPTi) powder in a 10:90 ratio. During the sintering process, these powders shall then diffuse together in the solid state and form a homogenous mixture creating the Ti-6Al-4V alloy (Xu, X., et al 2013 & Ye, B., et al, 2011). This significantly reduces the cost generally involved with conventional Ti-6Al-4V production as the typical BE PM process consists of mixing the elemental powder in the correct composition, cold pressing, vacuum sinter and a stage of HIP. If the HIP stage can

be removed when not necessary then the costs involved dramatically decrease (Ye, B., et al, 2011). The disadvantage of BE produced powders is the high residual porosity formation after the sintering process which in turn reduces the mechanical properties which leads to why the HIP stage is generally necessary for Ti-6Al-4V production. These residual porosities are formed from incomplete densification during sintering and also structural and phase transformations which lead to additional pore formation (swelling) (Ivasishin, O.M., et al, 2002).

Residual porosity is a common artefact of press-and-sinter PM alloys. In the ferrous alloy PM industry, infiltration with Cu is often used to fill the residual pores with Cu, thus improving the overall mechanical properties and machinability (Bernier, F., *et al*, 2011 & Das, J., *et al*, 2008). These improvements are strongly influenced by the apparent increase in density, due to the reduction in porosity. The effective load bearing sectional area is increased and the effect of pores as acting as stress concentrators is reduced, improving both strength and ductility. Fatigue is also strongly influenced as crack initiation occurs at or near the pores (Bernier, F., *et al*, 2011).

These findings initiated the investigation into whether a similar infiltration process may be viable for BE PM Ti-6Al-4V, that offers similar positive attributes as those that occur for Cu infiltration of ferrous alloy PM. In order to preserve the low density characteristic of the Ti-6Al-4V alloy, aluminium was chosen for the infiltrant material. The density of Al is lower than titanium and it has a low melting point, both of which are advantageous for system. Thus, the purpose of this study is to investigate whether infiltrating the sintered Ti-6Al-4V with molten Al is a feasible solution to improving the mechanical properties as well as machinability of the alloy. This process has the potential to open a route for a simple and cost-effective means of Ti-6Al-4V production using PM techniques.

## 1.2 Objectives

The aim of this research is to investigate the feasibility of developing an infiltration process that uses molten Al metal to infiltrate sintered Ti-6Al-4V parts. This aim is achieved through the following objectives:

- Develop a knowledge base on related research fields, comprised of past literature on sintering and infiltration of Ti-6Al-4V and infiltration of ferrous PM parts.
- Develop and evaluate a step-by-step procedure to produce, sinter and infiltrate sintered Ti-6Al-4V samples produced using published press-and-sinter procedures for BE and MA PM powder blends.

- Study the phenomena that affect the process at different steps by characterizing samples using various techniques, such as optical and scanning electron microscopy, and energy dispersive spectroscopy.

### 1.3 Motivation

Even though PM offers a cost effective and “green” manufacturing route for the production of titanium alloys, it has a significant drawback in the inherent residual porosity which is an artefact after the press-and-sinter process. In order to overcome the residual porosity, the ferrous PM industry has successfully made use of the sinter-infiltration process, with copper being the infiltrant metal. The motivation for this study is to investigate the feasibility of using a similar process for press-and-sintered Ti-6Al-4V by developing an infiltration process which uses molten Al to infiltrate the residual porosity of the sintered Ti-6Al-4V performs.

### 1.4 Limitations

This study follows a similar methodology as the study on copper infiltration of ferrous PM alloys during sintering conducted by Scholtz (2018). This study differs from the Fe-Cu system used previously in that the melting temperature of Cu is relatively close to the sintering temperature for ferrous alloys ( $T_{M,Cu} = 1038$  °C vs  $T_{sinter,Fe} = 1100$  °C), whereas for the Ti-6Al-4V:Al system, the melting point of Al is far below that of the sintering temperature parameters ( $T_{M,Al} = 660$  °C vs  $T_{sinter,Ti} > 1200$  °C). In order to avoid evaporation of molten Al during the high temperature Ti-6Al-4V sintering stage, the infiltration process for the Ti-6Al-4V:Al system was designed to be unique and differs from the traditional Fe:Cu system. The infiltration heat treatment process is designed as a separate process, that occurs after sintering, at a temperature just above the melting temperature of Al.

A limitation for this study was that the sintering process was not investigated, but rather extracted from previously published literature with the process parameters selected so as to produce parts with <92% sintered density. Selecting a sintered density below 92% ensures an open pore network which allows infiltration to occur in a separate process at temperatures slightly above the melting temperature of Al (German.R.M., 2005). Two PM Ti-6Al-4V press-and-sinter performs were investigated: a CPTi+MA elemental blend compacted and sintered according to the parameters taken from the work published by Bosman (2016), and a Ti-Al-V elemental blend compact and sintered according to the parameters taken from the work published by Clinning (2012).

Furthermore, as the focus of this study was process development, the microstructural and elemental analysis was limited to optical microscopy (OM), scanning electron microscopy (SEM) and energy dispersive X-ray spectroscopy (EDS) analysis. These techniques provided sufficient information so as to

evaluate the degree to which infiltration has occurred, and to explore why the infiltration was ultimately unsuccessful. The Cu infiltration experiments were included to evaluate whether the inability of the Al to melt was contributed to the furnace temperature, or due to metallurgy effects. This experiment was not included as a potential solution for the infiltration system for PM Ti-6Al-4V.

## **1.5 Hypothesis**

Press-and-sintered PM Ti-6Al-4V master alloy (MA) and blended elemental (BE) powder blend preforms are to be infiltrated with molten Al to significantly reduce the residual porosity with a separate infiltration heat treatment process, as opposed to the conventional process of combining the sintering and infiltration heat treatment processes. The resultant product shall be the infiltrated alloy with a non-stoichiometric Ti-6Al-4V skeletal network with the previous pores being filled with Al. The resultant product shall have improved material properties as well as machinability compared to the original sintered Ti-6Al-4V performs.

## **2 Literature Review**

This section discusses various relevant topics to the project and how sinter-infiltration is involved and discusses various characterization techniques.

### **2.1 Titanium and titanium alloys**

Titanium first became commercially available in 1950 by namely two companies, TIMET and Rem-Cru Titanium. These companies, along with others that followed, allowed aerospace industries to use the desirable properties of titanium, namely its high strength, low density and corrosion resistance. Early applications involved just the aerospace industry, but as industries saw the advanced applications of titanium, commercial and medical industries soon followed the trend (Froes, F.H., 2015:353).

#### **2.1.1 Structures and Properties**

Titanium varies in grade and preparation processes. Table 1 shows various titanium grades and those that are annealed with basic material properties of the ultimate and yield strength, modulus of elasticity, Poisson's ratio and the maximum melting points.

**Table 1: Basic material properties titanium (ASM Aerospace Specification Metals Inc., [S.a])**

<b>Titanium</b>	<b>Ultimate yield strength (MPa)</b>	<b>Ultimate tensile strength (MPa)</b>	<b>Modulus of elasticity (GPa)</b>	<b>Poisson's ratio</b>	<b>Melting point max (°C)</b>	<b>Density (g/cm<sup>3</sup>)</b>
<b>Grade 1</b>	170-310	240	105	0.37	1670	4.51
<b>Grade 1 annealed</b>	240	330	100	0.34	1670	4.51
<b>Grade 2</b>	275-410	344	105	0.37	1665	4.51
<b>Grade 2 annealed</b>	340	430	102	0.34	1665	4.51
<b>Grade 3</b>	377-520	440	105	0.37	1660	4.5
<b>Grade 3 annealed</b>	450	520	104	0.34	1660	4.5
<b>Grade 4</b>	480-552	550	105	0.37	1660	4.51
<b>Grade 4 annealed</b>	590	660	105	0.34	1660	4.51
<b>Ti-6Al-4V</b>	880	950	113.8	0.342	1604-1660	4.43

As seen in Table 1, titanium grades increase in yield and tensile strength as the grade is annealed. This heating process strengthens the properties of the material. The modulus of elasticity and Poisson's ratio remain fairly constant throughout with a relative density of 4.51 g/cm<sup>3</sup>, and melting points ranging from 1660-1670 °C. Ti-6Al-4V is a special alloy that is used widely in industry. As shown, its material properties, especially its strength, are far superior to that of pure titanium. In some cases its yield strength is almost doubled of that of its counterparts. It has a higher modulus of elasticity as well as a lower density. The brittleness compared to most titanium grades is also shown. Ti-6Al-4V is the most popular alloy consisting of the  $\alpha+\beta$  phase microstructures. These alloys are suitable for high

temperature strength applications yet are limited to applications of low temperatures (Coromant.S, 2004). At low temperature ranging between 315-400 °C, characteristics of Ti-6Al-4V are shown to be high strength, good corrosion resistance and high hardenability. Ti-6Al-4V is responsible for the largest percentage of titanium used in industry, with the aerospace industry being the largest consumers (Joubert, 2008).

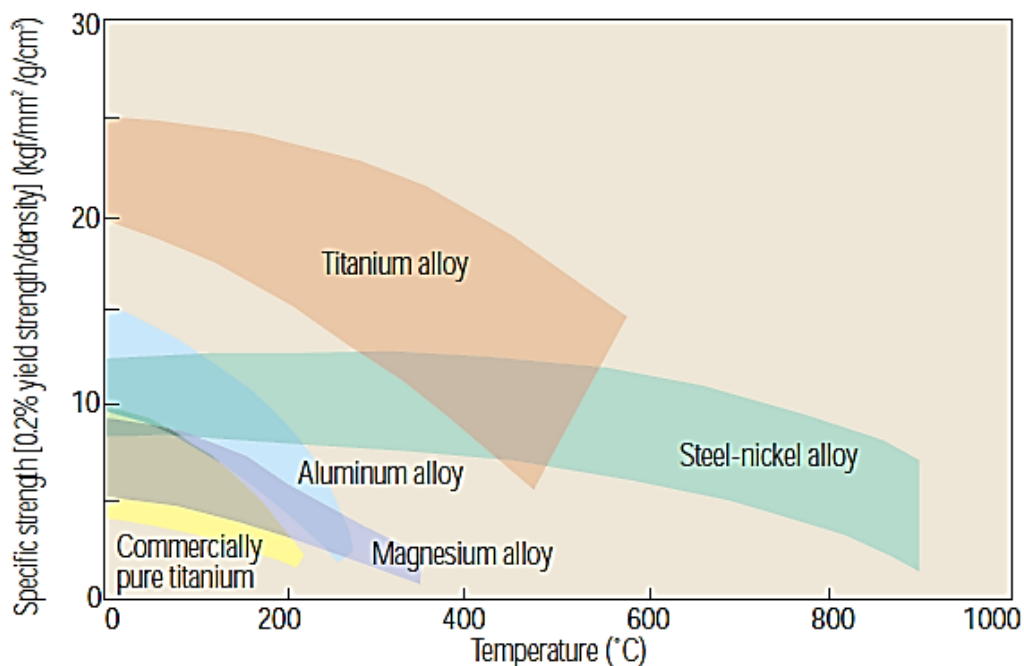


**Figure 1: Specific strengths against temperatures of various metals including titanium and titanium alloys (Kobelco, 2015)**

As seen in Figure 1, titanium alloys exhibit a superior specific strength compared to other metals and metal alloys at temperatures below 600 °C.

### 2.1.2 Titanium in Industry

Titanium is mainly used in the aerospace industry, and due to its high tensile strength and corrosion resistance titanium alloys are predominantly used in aircraft, naval ships, missiles and spacecrafts. About two thirds of titanium produced is used in aircraft engines and frames (Continental Steel & Tube Company, [S.a]). In the medical industry, titanium has become a very favourable metal. Titanium is completely inert to human body fluids, making it ideal for implants. It allows bone growth to stick to the implants very fast, as opposed to other metal counterparts. Other industries make use of titanium such as the armour and power generation (AZO Materials, 2002, [S.a]).

## 2.2 Phase Diagrams and Diffusivity

### 2.2.1 Ti-6Al-4V

Ti-6Al-4V forms a two phase mixture at room temperature of hexagonal close packed (HCP)  $\alpha$ -Ti and body center cubic (BCC)  $\beta$ -Ti, as can be seen by Figure 2. Upon heating above the  $\beta$  transus 980 °C (ASM Aerospace Specification Metals Inc., [S.a]), a complete solid solution of BCC  $\beta$ -Ti is achieved under equilibrium conditions. When sintering elemental or MA powder mixtures of Ti-6Al-4V, the two phase equilibrium microstructure that is predicted below 980 °C will not be present until diffusion between the particles created a homogenous alloy. Thus understanding the diffusion events that occur, leading up to the equilibrium condition is important. For this, the Ti-Al, Al-V, Ti-V systems will be reviewed.

The melting temperature of Ti-6Al-4V is 1660 °C (ASM Aerospace Specification Metals Inc., [S.a]) which indicates that the sintering temperature of a prealloyed Ti-6Al-4V powder should be around 1270 °C (80% of the absolute melting temperature). Pure titanium has a hexagonal close packed (HCP) crystal structure in the  $\alpha$  phase that exists at room temperature.  $\alpha$ -Ti transforms into body centered cubic (BCC)  $\beta$  phase at 882 °C (ASM Aerospace Specification Metals Inc., [S.a]) as seen in Figure 3. The addition of aluminium that is soluble in titanium, up to 6 wt%, remains an  $\alpha$ -phase alloy. It was also noted that the diffusion coefficient of V decreased with increasing Al alloying, which in turns states that Al diffusion hinders the diffusion of V in the Ti-Al-V system (Lindwall.G *et al*, 2018:731).

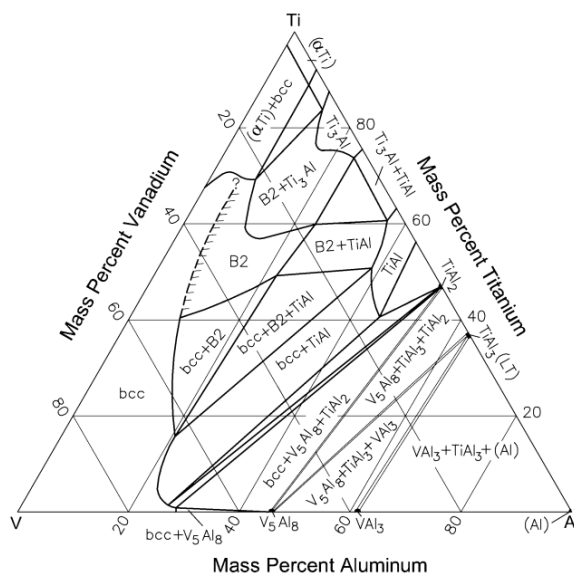


**Figure 2: Ti-Al-V ternary phase diagram at 600 °C (Raghaven, V., 2012)**

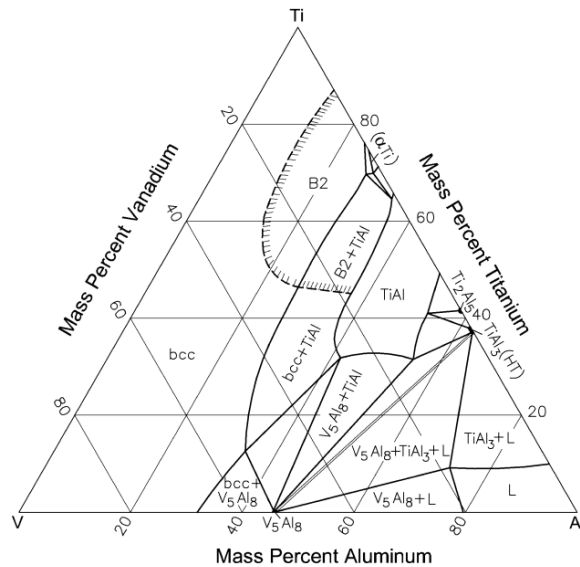


**Figure 3: Ti-Al-V ternary phase diagram at 1200 °C (Raghaven, V., 2012)**

### 2.2.2 Aluminium-Vanadium (Master alloy)

The Al-V binary phase diagram is significant to this study as it provides information regarding pure Al and pure V powders used in the elemental blend for Ti-6Al-4V, and it provides information on the 60:40 Al:V master alloy powder. As can be seen from Figure 4 Al melts at 660.45 °C (Okamoto, H., 2012). There is marginal, <1 at%, solubility of V in Al up to the melting temperature of Al. Vanadium has a melting temperature of 1910 °C (Okamoto, H., 2012) and forms a BCC solid solution with Al over a wide range of compositions (Lindahl, B., *et al.*, 2015). The solubility limit of Al in V is approximately 53 at% Al in V at 1405 °C. It should be noted that the solubility limit, along with the peritectic transformation ( $L+(V) \rightarrow \text{solid solution}$  (approximately 37.5 to 39.5 at% V in Al) at 1405 °C), is a recent update to the Al-V phase diagram (Okamoto, H., 2012). The 60:40 wt% Al:V master alloy should form two intermetallic compounds, namely the  $\text{Al}_3\text{V}$  and the  $\text{Al}_8\text{V}_5$ , under equilibrium conditions for all temperatures relevant to this study (< 1200 °C) (Kenny, D.J., *et al.*, 1953:77). What needs to be noted is the low melting point of aluminium.



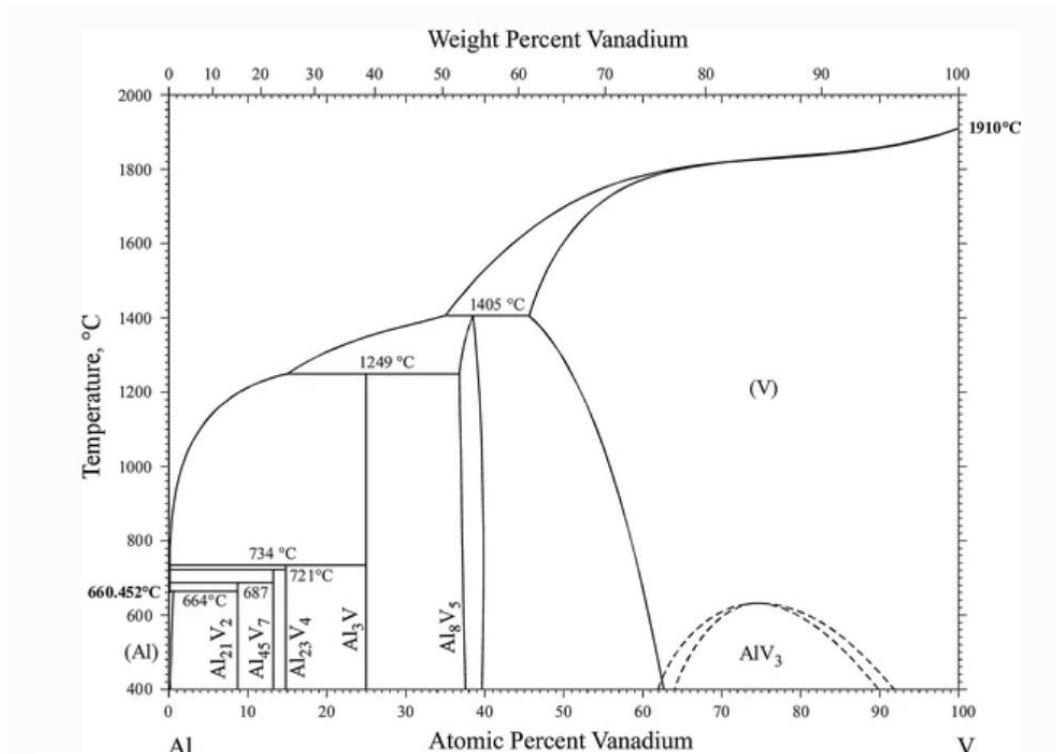


Figure 4: Aluminium-Vanadium binary phase diagram (Okamoto, H., 2012)

### 2.2.3 Titanium-Aluminium

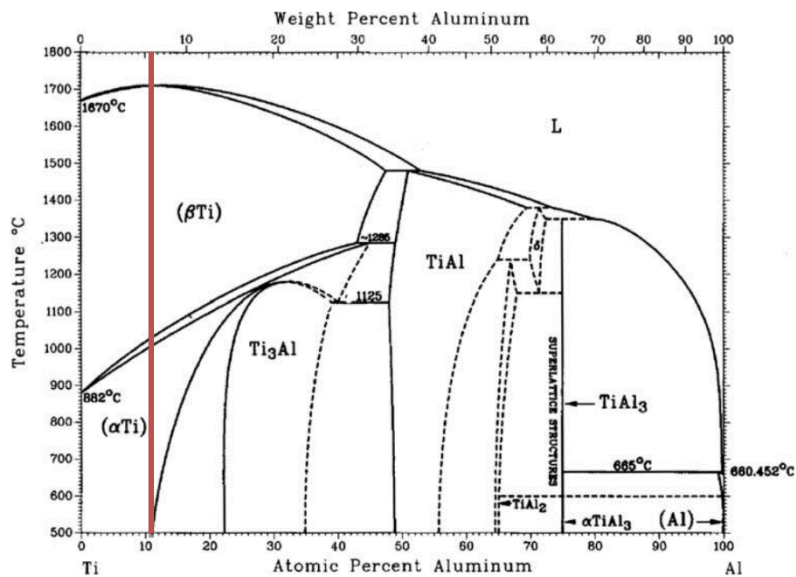
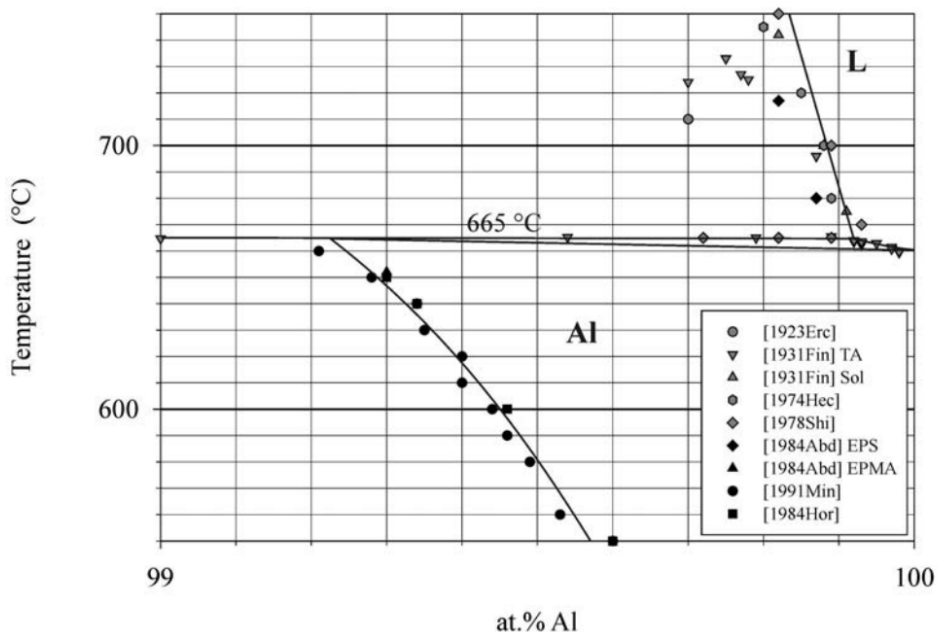


Figure 5: Adapted Titanium-Aluminium binary phase diagram (Schuster, J.C., et al 2006)

Figure 5 shows the binary phase diagram of titanium-aluminium at equilibrium. Aluminium has a very high solubility limit in titanium, reaching 32.4 wt% Al at 1503 °C in the  $\beta$ -phase, and around 36 wt% Al at 1443 °C in the alpha stage (*Titanium-Aluminium (Ti-Al) Phase Diagrams, 2011*). Solubility of Al in Ti at 6 wt% Al in Ti (noting that this would only occur in the absence of V for Ti-6Al-4V) shows the Al is dissolved in Ti to form the  $\alpha$ -Ti solid solution phase as shown in Figure 5. It transforms into  $\beta$ -Ti during heating to around 882 °C. Above this temperature the solubility of Al in Ti increases with temperature to a maximum of approximately 46 at% at approximately 1480 °C.



**Figure 6: Enhanced image of Titanium-Aluminium phase diagram (Schuster, J.C., *et al* 2006)**

As seen in Figure 6, below 665 °C there is very limited solubility of Ti in Al, approximately 0.8 at% Ti in Al maximum at 665 °C. Above 665 °C the Al rich solid phase goes through a peritectic transformation forming L(Al) and  $\text{TiAl}_3$ . The solubility of Ti in L(Al) tends to be lower at <0.1 at% Ti. At compositions above 0.1 at% the  $\text{TiAl}_3$  intermetallic forms with the excess Ti.

## 2.2.4 Titanium-Vanadium

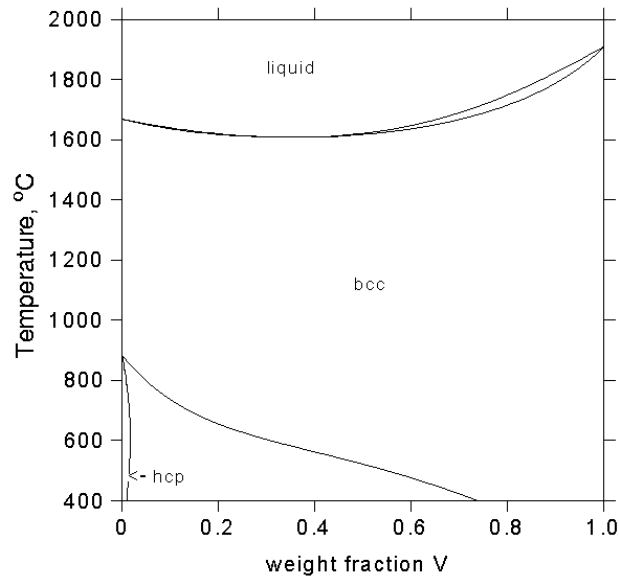


**Figure 7: Phase diagram of Titanium-Vanadium (Saunders, 1990)**

Figure 7 shows the Ti-V phase diagram, indicating that Ti and V are completely soluble in each other, forming  $\alpha$ -Ti (HCP) plus a  $\beta$ -phase at high Ti concentrations and temperatures below the Ti  $\beta$ -transus. On the V rich side, a single  $\beta$ -phase solid solution is formed with Ti.

## 2.2.5 (Titanium, Aluminium, Vanadium)-Nitrogen

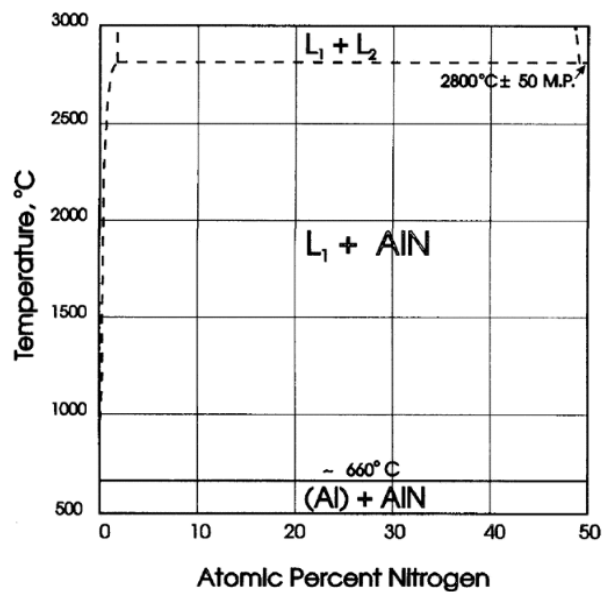


**Figure 8: Aluminium-Nitrogen binary phase diagram (Pierson, HO., 1996:201)**

With the addition of N being the process gas during the infiltration process, there is an expectation of phases forming with the Ti, Al and V with N. There is negligible solubility of N in Al in the solid state, with the solubility barely increasing after Al melts at 660 °C. For all practical purposes, N is insoluble in Al. AlN forms at 50 at% N and coexists with both solid and liquid (L) Al until 2800 °C.

For the Ti-N phase diagram we observe that N is soluble in Ti for a wide range of compositions. N is soluble in  $\alpha$ -Ti up to 882 °C, after which at temperatures higher than 882 °C N is soluble in  $\beta$ -Ti as seen in Figure 9.

Figure 10 shows the binary phase diagram of vanadium and nitrogen. A marginal amount of N is soluble in V, yet increases solubility with temperature. At the various infiltrating temperatures (700 °C to 900 °C) we observe increasing solubility <10 at%.

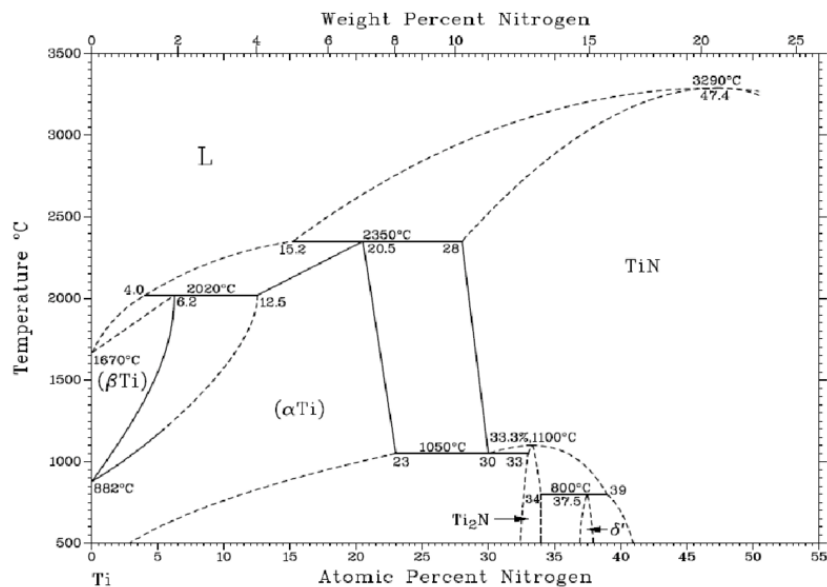


**Figure 9: Titanium-Nitrogen binary phase diagram (Skulev, H., 2014:57)**

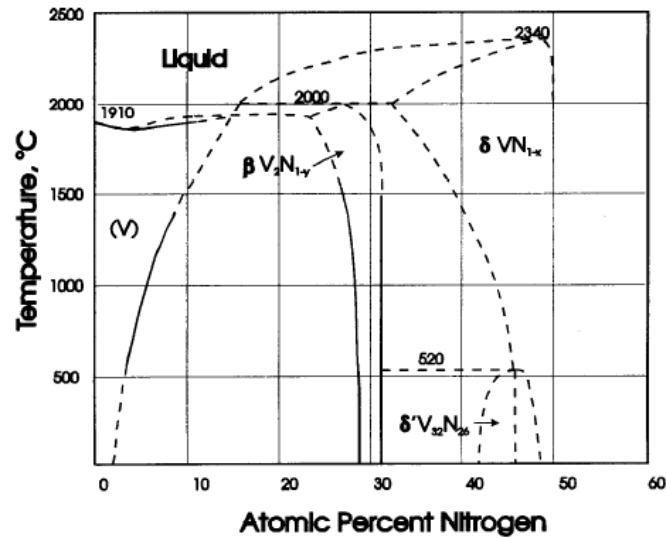


**Figure 10: Vanadium-Nitrogen binary phase diagram (Pierson, H.O., 1996: 202)**

## 2.3 Titanium Powder Metallurgy

### 2.3.1 Powder Metallurgy Techniques and Processes

Powder Metallurgy (PM) is a process which involves creating solid parts from metal powder products. The powder products are created through die compaction then generally heat treated to an elevated temperature below the melting point of the given alloy, also more commonly known as sintering, which induces solid state bonding (Shewman.PG, [S.a]). Ostwald *et al* (1997) describes strength and machinability as the two most important characteristics of metal powder metallurgy.

PM processes are highly used in the aerospace as well as the automotive industry (Froes, F.H., 2013). The ability for this process technique to grow faster than any other conventional process can be explained by its ability to produce very complex parts with unique, desirable properties and also allow for minimal wastage (Ramakrishnan, 1983:111). Complex part manufacturing can be a very costly process which can be performed with minimal waste and ease with PM processes. Grain boundary impurities can be controlled with up to 97% of the properties of the wrought form being achievable (Froes.FH *et al*, 2007). There are various ways to produce metallic powders. Chemical fabrication techniques can be used as the particle shape and size can be controlled. Powders can then be formed from solid, liquid or gas reactions (German.RM, 2005).

Atomization is the most commonly used technique as it is applicable to almost all metals, alloys and pure metals. This process involves the conversion of molten metal into a spray which solidifies into powders. Gas atomization uses a high

velocity gas stream, either air or an inert gas, and is used to atomize the liquid metal (Groover.MP, 2011). There are limitations to atomization techniques such as its limitation of the impact velocities being less than the speed of sound. This limits heat extraction, particle size and the energy efficiency (German.RM, 2005).

Conventional PM techniques consist of the press-and-sinter technique. This technique is performed in three steps, namely blending and mixing of powders, compaction of the powders into the desired shapes, and finally sintering which is heating to a temperature below the melting point which causes solid state bonding of the particles which in turn, strengthens the part (Groover.MP, 2011).

Alternative PM techniques include isostatic pressing, specifically cold isostatic pressing (CIP) and hot isostatic pressing (HIP). CIP is compaction performed at room temperature, with the mould being oversized to compensate for any shrinkage that may occur. CIP advantages include a better uniform density and less expensive tooling. HIP is performed at high temperatures and pressure with helium or argon as the compression gas. It is a very expensive process which applications are mostly used in the aerospace industry, yet it has very high densities which result in near zero porosity, and has very good mechanical strength.

Powder injection moulding (PIM) is another PM technique used. This process involves the metals or metal powders to be mixed with the appropriate binder, from which pellets are formed and melted to be injected into the mould cavity, then cooled and removed to be sintered. PIM is most economical for small, complex parts with high value (Groover.MP, 2011). Figure 11 shows a flow diagram of the basic PIM technique.

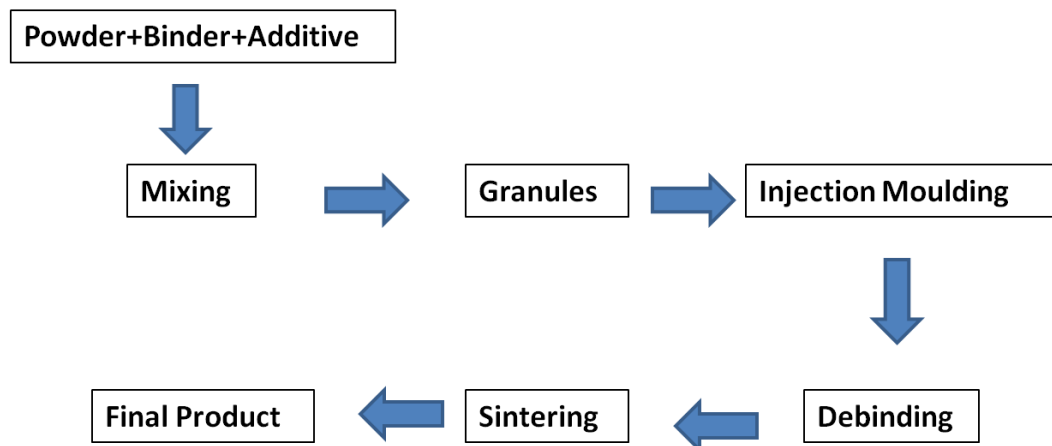


**Figure 11: Recreated basic process of powder injection moulding (Alcock.J et al, 1996)**

### 2.3.2 Titanium Alloy Powder Metallurgy Processes

Goso & Kale (2010:292) stated PM titanium alloys are fabricated with two major production methods, namely the fabrication of pre-alloyed (PA) powder mixture and a blended elemental (BE) powder mixture.

PA powder fabrication uses pre-mixed wrought alloys, and is performed with atomisation techniques, which involve vacuum melted and then atomised using gas. This in turn results in spherical particle shapes and as such this blend would not be suitable for die compaction yet be suitable for laser sintering (Elyon *et al.*, 1998). These blends have better mechanical properties than that of BE blends, yet are more expensive to produce.

BE fabrication is performed by mixing elemental powders, such as Ti, Al and V for Ti-6Al-4V fabrication. Goso & Kale, (2010:292) state the ease of fabrication of compared to PA production yet are restricted in complexity as well as size. BE production is usually performed with sponge fines which has a high concentration of chloride residuals which prevents full density being achievable, which affect mechanical properties. To improve mechanical properties and increase density, these BE blends generally go through a secondary process of hot forging (Eylon *et al.*, 1998:788). A more modern approach to producing BE alloys is through the hydrogenation-dehydrogenation method which produces high strength Ti-6Al-4V alloys by introducing hydrogen to the green compacts (Liu, J., *et al.*, 2018 & Cao, F., *et al.*, 2017).

### 2.3.3 Advantages and Disadvantages of Titanium and Titanium alloys Powder Metallurgy

PM techniques provide a number of advantages over traditional machining techniques, yet there are disadvantages or challenges that need to be overcome when using PM manufacturing techniques. The advantages of PM techniques as mentioned earlier by Froes *et al.* (2007) are that the grain boundary impurities can be controlled; along with up to 97% of the wrought form properties being achieved through PM. PM techniques has its main economic advantage in minimizing machining as some manufacturing techniques require machining such as broaching or tapping. Skilled machinist are not needed therefore labour costs are low and controlled porosity parts can be produced (Ostwald *et al.*, 1997).

Some limitations of PM are high density uniform products that are difficult to produce as metals in powder form are more expensive produce and need specialized equipment, therefore equipment costs are high. The difficulty to store powders with deterioration and thermal difficulties can occur within sintering operations for metals with low melting points (Ostwald *et al.*, 1997).

As also mention by Klar and Pransan (2007) PM parts produced are generally < 50 cm with the major dimension, making these parts very small with larger parts

not being economically practical. In the aerospace industry, titanium and titanium alloyed parts are vastly bigger to structural parts, hence PM are not generally used for general maintenance and repair. It is also noted that titanium powder is highly reactive therefore storage and production on a large scale can be dangerous.

## 2.4 Sintering Process

### 2.4.1 General Sintering

Sintering is a high temperature process through which powders bond together, usually by solid state sintering, to form a continuous solid material at temperatures below their melting points (Schaschke.C, 2014). Sintering powders and other elements is evident on a micro structural level as necks begin to form between molecules. Figure 12 shows the general flow diagram process involving sintering. Sintering is a process used to create density controlled materials from metal/ceramic powders by applying thermal energy. There are two types of sintering namely solid state and liquid state sintering. Solid state sintering occurs as the powder in use densifies at the sintering temperature; while liquid state sintering occurs when densification occurs in the present of a liquid phase (Joong.S *et al*, 2007). There are other transitional states included which are shown in Figure 13. Figure 14 shows examples of solid and liquid state sintering where one can observe in Figure 14 b) the liquid structures present from liquid state sintering. Groover (2011) stated that the general sintering temperature range takes place at 0.7 and 0.9 of the powder metal's melting temperature.

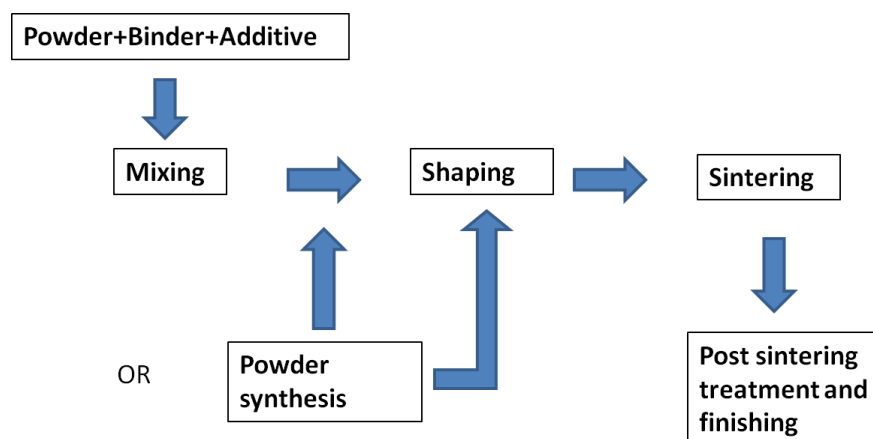


**Figure 12: Recreated flow diagram of the process involving sintering (Joong.S et al, 2007)**



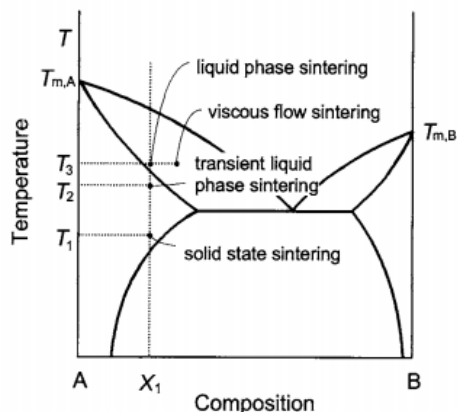


**Figure 13: Transitional sintering states on a phase diagram (Joong.S *et al*, 2007)**

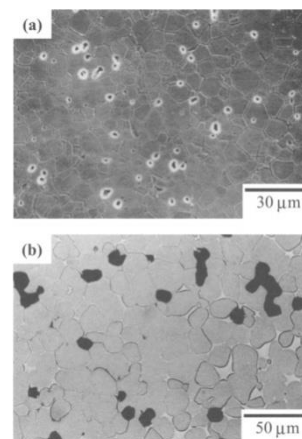


**Figure 14: a) Solid state and b) liquid state sintering (Joong.S *et al*, 2007)**

#### 2.4.2 Titanium and Ti-6Al-4V Sintering

A study by Xu *et al.* (2014:994) was performed to investigate sintering behaviour of blended Ti-6Al-4V powder compacts. One of the Ti-6Al-4V compacts consisted of a master alloy (MA) of 60% Al and 40% V. The compact was mixed in a 90:10 ratio of commercially pure (CP) Ti and MA respectively. The samples were pressed in a floating die configuration and pressed at 690 MPa. The samples were heated to various temperatures and then quenched in order to preserve the instantaneous microstructure to be studied. It was found that no transient liquid phase took place during the sintering of the blended compacts as the master alloy did not melt at a sintering temperature of 1260 °C.

This is due initially to the decrease of aluminium from the master alloy via diffusion into the Ti-6Al-4V blend, which leads to a higher vanadium content in prior MA particles which increases the melting temperature of said particles. The centre compositions were investigated to determine the amount of aluminium and vanadium diffuses with various sintering temperatures. It was seen the centre compositions were all in the solid state region as shown in Figure 15. The diffusion paths of the samples show that they tend to move in the direction of the lower aluminium concentration as at higher sintering temperatures sufficient aluminium has diffused.

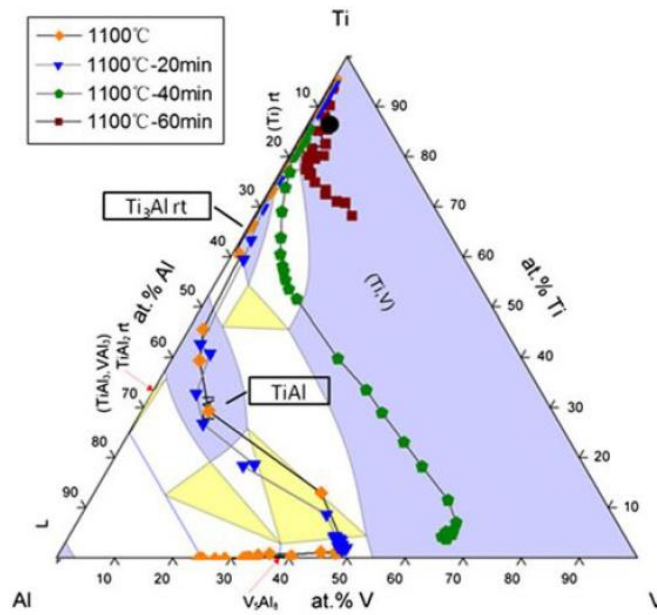


**Figure 15: Ternary phase diagram showing diffusion paths at 1100 °C and various dwell times (Xu *et al.* 2014:994)**

### 2.4.3 Aluminium Sintering (During Infiltration Heat Treatment)

Moisture has a reportedly significant effect on the successful sintering of aluminium powder. A very low dew point of  $-51\text{ }^{\circ}\text{C}$  or lower is required, which can correspond to 34 ppm moisture by volume (Qian, M., *et al.*, 2010:289). Sintering in argon does produce adequate results, yet is less effective than sintering under nitrogen. A nitrogen atmosphere, with low dew points and high purity, was found to consistently produce the highest strength for sintered aluminium PM parts (Qian, M., *et al.*, 2010:289). Nitrogen is considered to be a more effective sintering atmosphere than argon or vacuum; the beneficial effect is attributed to the formation of AlN (Schaffer, GB *et al.*, 2006:131). Schaffer, GB *et al.* (2006:131) suggest that during nitrogen sintering of aluminium, pores are filled with nitrogen; nitrogen subsequently reacts with Al to form AlN, thus consuming the nitrogen and decrease the pressure within the pores.

Qian, M *et al.* (2010:289) noted that each aluminium powder particle was coated with a layer of alumina (aluminium oxide). This oxide film acts as a barrier against aluminium sintering and diffusion between particles, and effects the liquid phase sintering due to the limited wetting. A way to rupture the oxide film with a mechanical means was to compact the powder via the press process. The film ruptures at points where the particles touch each other forming metal contact

points, and allow the particles to cold weld at these oxide free points where diffusion can occur (Qian.M et al, 2010:289). It should be noted though during conventional pressing the oxide film, although cracked, shall remain on the particle boundaries. The benefits of using nitrogen as a process gas during sintering of aluminium are multiple; it is also known to dissolve these passive oxide layers (Schaffer. GB et al, 2006:131).

By studying phase diagrams of nitrogen with titanium, aluminium and vanadium respectively, it is evident at what temperature and mass/atomic percentages nitrides between the metals start to form. From studies performed by Pierson. HO (1996:238), it was determined that vanadium nitrides are produced from V powder under nitrogen or ammonia at 1200 °C. From the Ti-N phase diagrams one can conclude titanium nitrides begin to form at 500 °C with a mass percentage of approximately 2.5% nitrogen. At the desired temperature of 700 °C, approximately 4.5 wt% can be consumed before nitrides form (Computational Thermodynamic, [S.a]). From the Al-N phase diagram, nitrides begin to form below 500 °C, and with the desired temperature liquid phase aluminium shall form with AlN (Pierson. HO, 1996:238) as seen in Figure 8, Figure 9 and Figure 10.

## **2.5 Infiltration Heat Treatment Process**

### **2.5.1 General Infiltration**

Infiltration can be defined as filling up a porous material with that of a material with a lower melting point, in the liquid phase, to produce a composite and to improve properties such as tensile strength, hardness, ductility and improve machinability (Suresh.S *et al*, 1993). Liquid infiltration has been around for decades in order to strengthen porous metal parts (Lenel.FV, 1980). Vacuum driven infiltration and pressure driven infiltration are simple processes to perform the infiltration needed. The vacuum infiltration is completed by creating a vacuum around that part to be infiltrated with the infiltrating metal, and the vacuum creates a pressure drop large enough from infiltration to take place. Pressure infiltration is supplied by gas or mechanical ways. With gas the metal is forced into the infiltrated part by an inert gas, while the mechanical process uses a hydraulic press to create higher pressure. The pressure method has advantageous benefits over the vacuum process, such as increased processing speed, better soundness and chemical reaction control (Suresh.S *et al*, 1993).

The resulting product after infiltration is relatively nonporous, with the infiltrated sample having higher uniform density as well as an improvement in both strength and toughness (Groover.MP, 2011). German.RM (2005) stated that for a sample to be porous enough for infiltration to take place, the sintered density of said sample needs to be <92% sintered density. Above these sintered densities are where the pore channels begin to close off.

Infiltration is caused due to a capillary effect with the capillary induced pressure driving the fluid into the skeleton of some sort. Infiltration will continue in a non-reactive system until the gravitational head balances the capillary forces (Lorenz.AM, S.a). Yu & Schaffer (2009:163) noted that during infiltration under nitrogen and vacuum, the sample pores tend to fill from the surface inwards for the nitrogen infiltration, and conversely for vacuum infiltration takes place from the interior outwards. Figure 16 shows the surfaces of a sample infiltrated under nitrogen (left) and vacuum (right).

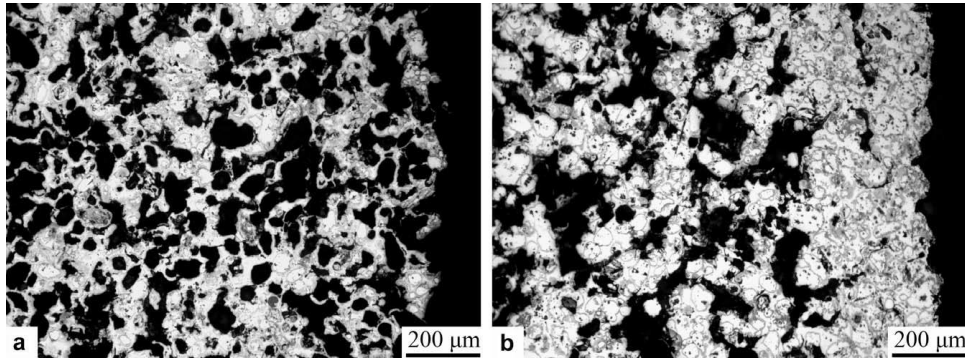


**Figure 16: Samples infiltrated under a) nitrogen and b) vacuum at 658 °C (Yu.P, Schaffer.GB, 2008:163)**

### 2.5.2 Contact Angles

The spread of a molten metal on a solid metal is determined by the wetting/contact angle (Bao.S *et al*, 2011:1358). This contact angle, ( $\theta$ ) is a term used to describe the angle the liquid drop makes with a surface (Tadmor and Yadav, 2008:241), as illustrated by Figure 17. Table 2 shows the relationship between the contact angle and the degree of wetting. As mentioned in section 2.5.1 the driving force for infiltration is the capillary forces which continue until the gravitational head balances the capillary forces. These forces are determined by the contact angle which is also an indication of whether infiltration shall take place.

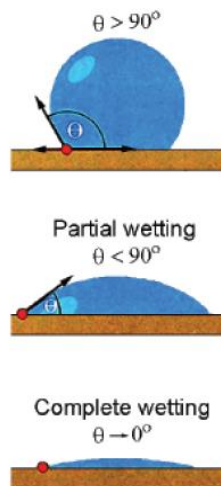


**Figure 17: Contact angles**  
(Smith. SM, *et al.*, 2014:2)

**Table 2: Contact angle and wetting**  
(Khandekar *et al.*, 2010)

Contact Angle	Degree of Wetting
$0^\circ$	Perfect wetting
$0^\circ < \theta < 90^\circ$	High wettability
$90^\circ < \theta < 180^\circ$	Low wettability
$180^\circ$	Perfectly Non-wetting

As mentioned in literature, there are various methods for measuring the contact angle of a medium (Smit, S.M., *et al* 2014:2). These methods can be performed with simple equipment, such as tensiometer or even a digital camera. Common techniques using these include the sessile drop method and the Wilhelmy plate method. Other techniques may also be used such as displacement of mutually immiscible fluids in a capillary or the capillary rise of a liquid in a partially submerge plate (Dussan.EB, 1979:371). To date there have been no studies on the contact angle of molten Al on Ti.

## 2.6 Al Infiltration with Ti and Ti Preforms

Two studies that investigate the infiltration of Ti-alloy preforms with molten Al were found. The first studied two injection moulded and sintered Ti-based preforms that were subsequently infiltrated with molten Al, and then subjected to a precipitation hardening heat treatment (Kim. S., *et al*, 2018:775). The second studied Ti-coated diamond particles over which Al is melted to form a metal matrix composite (Che. Z., *et al*, 2017:285).

Kim, S., *et al* (2018) initially used either pure Ti, or TiH<sub>2</sub> and V powders that were mixed in a 45:2 wt % ratio, and combined with polymer binders to produce samples using injection moulding. The samples were thermally de-bound and then sintered under vacuum at 1200 °C for 2 hours, producing a 90 % sintered density preform (10% residual porosity). The sintered samples were immersed in a bath of molten Al at 730 °C for 5, 10 and 15 s under an argon atmosphere, allowing the liquid Al to infiltrate the pores. After the Al infiltration process, the samples were subjected to precipitation hardening heat treatments of a solution heat treatment at 1000 °C for 3 hrs, followed by aging. Microscopic analysis of the final

microstructures showed that two distinctly different behaviours occurred, depending on whether the preform contained Ti only or Ti + V.

For the pure Ti samples, the molten Al that filled the pores completely diffused into the Ti sintered matrix after the heat treatment process. The resulting microstructure consisted of the brittle intermetallic  $TiAl_3$  and included large pores. Explanations for pore formation was attributed to diffusion/evaporation of Al, difference in molar volumes and the Kirkendall effect caused by dissimilar diffusion rates of the Ti and Al. Kim, S., et al (2017) explains, with regards to the Kirkendall effect, that Al has a faster diffusion rate into Ti than Ti has into Al. Hence the Al rapidly diffuses into the Ti-matrix, leaving voids in its wake. In contrast, Ti has no time to diffuse into the Al before it has diffused into the Ti.

In contrast, the Ti-V alloy (hydrogen is removed from the alloy during the vacuum sintering process) displayed a markedly different microstructure. There are no large pores and the material appears to be fully dense. This behaviour is explained by the influence of V in solid solution with Ti retarding the diffusion rate of Al into the sintered matrix. The resultant microstructure is a dual phase  $\alpha+\beta$  microstructure, with areas of high Al – low V concentration correlating to the  $\alpha$ -phase, and areas of low Al – high V concentrations correlating to the  $\beta$ -phase. It is suggested that this microstructure evolves by the following naturally occurring mechanisms: (1) the diffusion of Al, from previous pores that are now filled with Al, into the Ti-V sintered matrix is retarded by the presence of V in the matrix; at the same time (2) the increased time for diffusion allows Ti and V to diffuse into the Al filled pores. This indicates that in prior pores that were filled with molten Al during infiltration (high Al concentration)  $\alpha$ -phase regions evolve, whereas areas with higher V concentration,  $\beta$ -phase regions evolve where Al has diffused into the Ti-V matrix, resulting in the dual phase microstructure. It should be noted that there are no observable pores in the final Ti-V-Al microstructure, suggesting that there was no melting-evaporation or rapid diffusion behaviour that would result in void formation, as is the case in the Ti-Al system.

This study shows that the presence of even a slight amount of V (<4 wt%) can affect the diffusion of Al into the Ti-alloy matrix.

Che, Z., et al (2017) investigated the production of a metal matrix composite (MMC) by placing Ti-coated diamond particles underneath an Al block, and then subjecting the system to a pressure induced heat treatment where the Al melts and forms around the diamond particles, creating a diamond reinforced Al-MMC. Initially a vacuum was pulled after which heat treatment was performed to 800 °C. High purity argon was then pumped into the system until the pressure reached 1 MPa and was held there for 20 min to ensure infiltration occurred, after which the samples were furnace cooled. It was found that a continuous microstructure formed between the diamond particles and Al matrix. Microscopic  $Al_3Ti$  particles were found embedded in the Al matrix formed by the reaction of molten Al and isolated Ti layers present on the coating surface. This was observed to occur at the beginning of the infiltration process. During the sintering period, it was found that

Al<sub>4</sub>Ti forms along the grain boundaries of the columnar TiC grain layer, through the grain boundary diffusion of Al within the TiC columnar layer.

### 3 Design of Experiments

In order to achieve the objectives set out in Section 1.2, a set of experiments was designed, the details of which are presented in this section. Ti-6Al-4V PM samples, using two different powder blends, were die-compacted and vacuum sintered to 1100 °C and 1200 °C, respectively, in order to produce samples with different sinter density. These samples were used at the substrates or matrix samples for infiltration. Al disks were placed on top of the samples and they were subjected to the infiltration heat treatment process. Various characterisation and analysis techniques were used in order to evaluate the results of each process step.

#### 3.1 Materials

Two powder blends were designed to meet the standard of PM Grade 5 Ti-6Al-4V standard specifications (ASTM B988-13, 2013). Ti, Al, and V powders were mixed in a 90:6:4 weight percentage ratios in order to prepare a blended elemental (BE) Ti-6Al-4V powder mixture. Commercially pure Ti (CPTi) and 60:40 Al:V master alloy (MA) powders were mixed in a 90:10 weight percentage ratio in order to prepare a CPTi+MA Ti-6Al-4V powder blend, as seen in Table 3.

**Table 3: Materials specifications**

Powder	Supplier	Mesh Size	Notes
Ti	Global Titanium	-200	Commercially Pure (CP)
Al	Alfar Aesar	-100+325	99.5% metal basis
V	Alfar Aesar	-325	99.5% metal basis
60:40 Al-V Master Alloy	Reading alloys: USA	-200	-
Al	Valimet Inc.	-	Infiltration disks
Al wrought	-	-	Infiltration disks
Cu disks	Bleistahl-Produktions GmbH & Co.	-	Infiltration disks

## 3.2 Compaction Process

The Ti-6Al-4V samples were pressed using a Carver 12 ton Hydraulic Press at 400 MPa using a  $\varnothing 10$  mm cylindrical die with a height of 10 mm while the Al powder samples were pressed at 100 MPa using the same die. According to Bosman (2016) the Ti-6Al-4V samples would have an approximate green density ( $\rho_g$ ) of 75%, which was used in equation 1 to determine the mass of the powder needed to obtain the required Ti-6Al-4V green height ( $h_g$ ).

$$m = A * h_g * \rho_g \quad (1)$$

Where,

$m$  is the mass of powder,  $A$  is the cross sectional area,  $h_g$  is the green height and  $\rho_g$  is the green density.

The Al samples were pressed after the sintered densities of the Ti-6Al-4V samples were calculated to determine the porosity within those samples and thus the mass of Al can be calculated with equation 2.

$$m_{Al} = \rho_{Al} * V_{pores} * V_{sample} \quad (2)$$

Where,

$m_{Al}$  is the mass of aluminium,  $\rho_{Al}$  is the density of wrought aluminium,  $V_{pores}$  is the volume percentage of aluminium and  $V_{sample}$  is the volume of the sample.

With

$$V_{pores} = 1 - \left(\frac{\rho_s}{\rho_{th}}\right) \quad (3)$$

Where,

$\rho_s$  is the sintered density and  $\rho_{th}$  is the theoretical or wrought density of Ti-6Al-4V,  $4.43 \text{ g/cm}^3$ .

## 3.3 Heat Treatment (Sintering)

The sintering heat treatment took place under vacuum. This method took place in a horizontal tube furnace (Elite TSH 15/25/180) connected to an argon gas supply which was used to flush out any oxygen within the system. The components of the system are listed in Table 4. Densities were measured after the samples were sintered by measuring the new volume and mass after the sintering process.



**Table 4: Vacuum Sinter Pump Components**

<b>Components</b>	<b>Model</b>	<b>Manufacturer</b>
Horizontal tube	Elite TSH 15/25/180	Elite Thermal
Furnace	TSH 15-50-180	Systems
Argon/Nitrogen Supply	-	AFROX
Turbo Pump	Turbo-V 81-M	Varian
Rotary Vane Pump	Pascal 2012 SD	Adixen
Vacuum Gauge	ACS 2000	Adixen

Both Ti-6Al-4V compact blends (CPTi+MA and BE) were sintered under vacuum with an argon supply running through the furnace initially to flush out any oxygen residing within the system. From previous studies performed by Bosman (2016), it was noted that master alloy samples sintered at 1300 °C result in a sintered density >92%; this density results in closed pores which prevents infiltration. Therefore, the sintering parameters for the samples were chosen as to produce sintered densities <92%. The samples were sintered under vacuum, at temperatures of 1100 °C and 1200 °C, respectively, with a 2 hour dwell at the peak temperatures. A heating rate of 10 °C/min was used until the samples reached the peak temperatures. The samples were then furnace cooled until they reached room temperature.

### **3.4 Infiltration Heat Treatment Process**

The purpose of the infiltration heat treatment process is to heat pure Al in contact with the sintered Ti-6Al-4V preform to above the melting temperature of Al (660.6 °C), so that once the Al melts, liquid Al is drawn into the residual porosity of the sintered Ti-6Al-4V samples by pressure driven capillary forces.

Infiltration took place in the same horizontal tube furnace as described in Section 3.3 with the exception that the system was flushed with a constant flow of either argon or nitrogen. The Ti-6Al-4V sintered samples were placed in the horizontal tube on yttria-stabilised zirconia substrates, with the compacted Al or wrought Al samples placed above or below the Ti-6Al-4V sintered sample. The furnace was heated up to 700 °C, 750 °C and 900 °C with a 0 hr, 1 hr and 1 hr dwell time, respectively. Once the required temperature is reached and the dwell time has finished, the samples are furnace cooled to room temperature.

Infiltration under vacuum was not considered, due to the risk of contaminating the vacuum system with Al vapour that may condense inside the pumps. Initially, infiltration was evaluated under an argon atmosphere in order to prevent reaction of the Ti-6Al-4V with the process gas; however, the Al disk showed no signs of melting under these parameters. Reasons for this were investigated and mitigation actions planned, as reported in the following paragraphs.

#### **Possible Reason 1: Oxide formation on Al particles**

Aluminium spontaneously forms a passive oxide layer of  $\text{Al}_2\text{O}_3$  of a few nanometres thick in the presence of air (Lohrey, M., *et al*, 2015). Thus it is typical for Al powder particles to be encased by a thin  $\text{Al}_2\text{O}_3$  layer. In studies on the sintering of Al, this has been cited as a deterrent to the formation of sinter-bonds between particles and can impede the sintering of Al (Schaffer, GB *et al* 2006). The expected, persistent  $\text{Al}_2\text{O}_3$  layer was considered as a possible reason for the absence of melting.

The first approach to overcoming the oxide layer hindrance was based on studies on the sintering of Al, discussed in section 2.4.3. The study indicates that during compaction of Al powder, the alumina layer present around the Al particles is disrupted and the Al particles cold-weld to each other (Qian, M., *et al*, 2010:305). This is sufficient in order to allow for sintering to occur at elevated temperatures. Another study used nitrogen as the process gas during sintering and showed that the formation of AlN disrupts the oxide layer and assists in sintering by reducing the pressure within the pore spaces which leads to an unbalance in the meniscus forces. This leads to pore filling which ultimately aids sintering (Schaffer, G.B., *et al*, 2006).

As the Al disks were already made from compacted powder, it was expected that the oxide layer was already mechanically disrupted and should ensure metal-to-metal contacts between powder particles. Nevertheless, the subsequent infiltration tests were performed under nitrogen, in order to investigate whether a similar disruption of the oxide layer as realized in sintering study referenced above, would be realized for melting the Al compact.

#### **Possible Reason 2: Insufficient flushing of furnace tube**

A previous study that investigated the flow of argon in the furnace tube, showed that due to the density difference between argon and air, a straight inlet flow of argon was ineffective for flushing the tube of air (Terblanche, 2014). This was shown using a computational fluid dynamics (CFD) analysis. A similar CFD analysis was performed to simulate the system using nitrogen as a process gas, to determine whether air was fully flushed from the tube. It was found that all the air was evacuated and the system was filled with nitrogen as seen in Figure 18, indicating that the gas inlet system (using a conical inlet-outlet system) was suitable. No further investigation into this reason was pursued.

### Possible Reason 3: Cooling due to flow rate of process gas

Another possible reason for the absence of melting that was investigated was the potential cooling of the system, to below the melting temperature of Al, due to flow rate of cold nitrogen entering the furnace tube. In order to evaluate this, a stagnate nitrogen atmosphere was created in the tube by closing the inlet and outlet valves once the tube had been flushed with flowing nitrogen.

### Possible Reason 4: Contact angle

The contact angle of molten Al on Ti-6Al-4V is unknown, therefore a different approach was investigated in order to see whether the combination of Al with Ti-6Al-4V may be the reason for the absence of infiltration. An experimental setup where a copper disk was placed above the Ti-6Al-4V sample and heated to above the melting temperature of Cu was designed, based on the study by Scholtz (2018) for Cu infiltration of ferrous PM. The system was heated to 1150 °C under a nitrogen atmosphere, and held at the peak temperature for 1 hour, followed by furnace cooling. The results of this experiment are discussed further on.

DSC analysis of a sample of the Al powder was conducted in nitrogen, heating from room temperature to 750 °C. It should be noted that as the DSC sample holder is aluminium, and the equipment warned against heating to temperatures above 660 °C. The results did not show any distinct peaks and were inconclusive. This could be due to contamination of the chamber from previous experiments. The equipment is currently scheduled for maintenance due to contamination and therefore, these results were not included in the study.

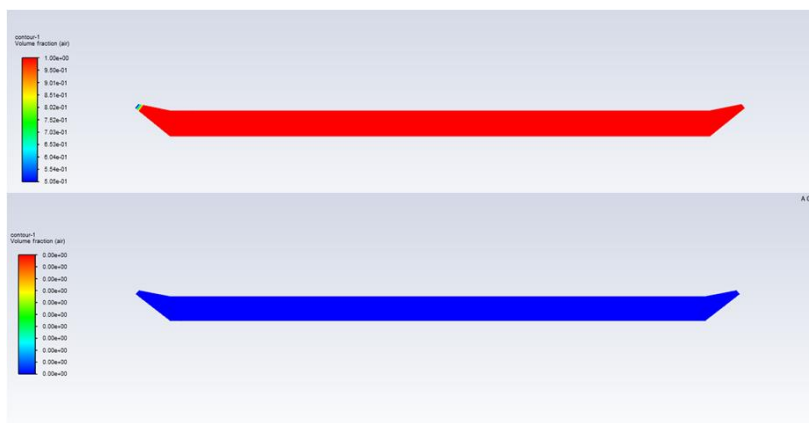


**Figure 18: CFD analysis of nitrogen through tube furnace before (top) and after (bottom)**

## **3.5 Preparation of Samples**

The following process describes how the sample is prepared in order to characterize it with various microscopy techniques.

### **3.5.1 Cutting**

The samples are cut at various depths with a BUEHLER IsoMet low speed saw and serviced by Apollo Scientific cc and a MICRACUT 150 Precision cutter supplied and serviced by MICRO MET SCIENTIFIC cc. The samples are placed in a rig and cut with a diamond impregnated blade at a constant rpm to ensure a uniform surface.

### **3.5.2 Hot Mount**

Once the samples have been cut they were mounted. This was performed with a Buehler SimpliMet 1000 Automatic Mounting Press supplied and serviced by Apollo Scientific cc. Buehler Epomet Modling. A compound resin PolyFast hot mounting resin was used to hot mount the sample in the mounting press with the sample being placed with the surface of interest faced down.

### **3.5.3 Grinding and Polishing**

After mounting, the samples were ground and polished before characterization could be performed. A Buehler Alpha 2 Speed Grinder-Polisher was used in conjunction with a Buehler Vector Power Head with both being supplied and serviced by Apollo Scientific cc for the grinding process. Initially a 600 grit SiC sandpaper plate was used at 15-25 kN for 90 seconds and opposite rotation for the head and base was used, after which a the grit sizes increases in increments of 200 until finally a 1200 grit SiC sandpaper plate was used with the same parameters, sometimes more than once to eliminate any uneven surfaces and scratches.

Once the grinding was completed, the samples were cleaned in the ultrasonic cleaner by placing the samples in isopropanol. Polishing then took place using a Struers Labopol Automatic Grinder-Polisher. Two steps needed to be performed for polishing. Firstly a Green Honeycomb diamond impregnated composite disk (Struers MD-Allergo/Largo) was used with a 9  $\mu\text{m}$  diamond suspension at 25 kN force for 5 minutes. The samples were cleaned in the ultrasonic cleaner after this step. Secondly a polishing cloth disk (Struers MD-Nap) with a 0.04  $\mu\text{m}$  colloidal silica suspension (Struers OP-U or OP-S) at 25 kN force for 5 minutes was used. The samples were cleaned again in the ultrasonic cleaner after this step. If it happened the Al slug was still present after infiltration, only the polishing cloth was used with the accompanying suspension for a longer polishing period as the diamond suspension scratches the soft Al. The samples were then rinsed with methanol and immediately dried with a flow of heated air.

If the grain boundaries needed to be observed as well as to see the boundary of the sample for oxidation that may have taken place, the sample shall then be etched with Kroll's Reagent by swabbing it with a cotton bud and then rinsing with water and methanol. Immediately after, the sample is to be dried with a flow of heated air. High caution is to be practiced whilst working with these chemicals.

## **3.6 Characterization**

The following processes describe the characterization techniques used for the samples metallographic properties.

### **3.6.1 Optical Microscopy (OM)**

An OLYMPUS GX51 microscope using the Stream Essentials program was used to observe the porosity and microstructure of the sample. The porosity is observed with phase analysis function while the grain boundaries are physically seen under the microscope after the samples have been etched.

### **3.6.2 Scanning Electron Microscopy (SEM)**

Imaging of the sample surface needed to be performed to observe the topography of the infiltrated sample. The infiltrated pores were also observed with this device as well as the depth of the infiltration. The ZEISS MERLIN SEM with the GEMINI II was used to perform the above mentioned tests. The SEM has a resolution up to 0.6nm with a probe current of up to 300nA and an acceleration voltage of 20V-30kV.

### **3.6.3 Energy Dispersive X-Ray Spectroscopy (EDS)**

Electron dispersive spectroscopy (EDS) mapping detects the sample by means of an electron beam that characterizes the composition of the analysed sample by hitting the sample surface and detecting the difference in density to determine elements (Materials Evaluation and Engineering Inc., 2014). EDS mapping was performed to detect the depth of infiltration from the Al slug. Oxidation or the formations of nitrides were also observed using this device. One can investigate the change in concentration of aluminium through areas of interest using this technique. The ZEISS MERLIN SEM with the GEMINI II was also used to perform the above mentioned tests as well as a ZEISS EVO MA15VP SEM which was used for elemental composition through the interface of the Ti-6Al-4V sample and the Al disk, from which diffusion graphs could be plotted as seen in Section 4.3.9 and Appendix C: Diffusion graphs. Figure 19 displays the surface at which the electron beam from the EDS analysis that shall be investigated. As seen the pore surface is being analysed.

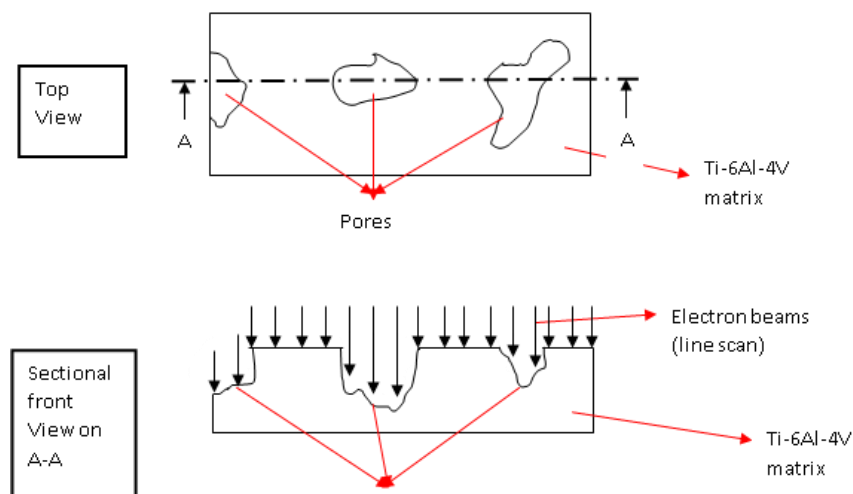


**Figure 19: Schematic representing the analyses of a pore with an electron beam**

## 4 Results

This chapter shows the results obtained from the vacuum sinter and infiltration processes conducted. The microstructural analysis is presented along with the elemental analysis of the sinter-infiltrated samples with a short explanation as to what the results entail.

### 4.1 Vacuum Sinter

A summarised table of results for the sample preparation process is shown in Table 5. Samples from the two Ti-6Al-4V blends, namely the master alloy (MA) and elemental blend (BE) blends, were die compacted and sintered as described in Section 3.2 and Section 3.3. The average and standard deviation of relative density after compaction (green) and sintering, respectively, as well as the absolute change in density during sintering is shown for each sample set. The full results are presented in Appendix A. Two sintering temperatures were chosen so as to evaluate two different final densities.

As seen in Table 5, the relative green density for all the samples was reasonably consistent between 73% and 75%, with standard deviations around 1%. The MA samples all densified to a mean relative sinter density of 90%, although the standard deviation of the data was higher for the samples sintered at 1200 °C. The standard deviation for the MA, 1200 °C indicates that some samples reached 94% relative density after sintering; however, this is due to the small size of the data set (6 samples). In fact, the highest density reached was 92.2%. Nevertheless, this is

above the theoretical limit for open porosity (92%). The BE samples showed negligible densification during sintering. As seen in Appendix A, the mass before and after sintering for the BE samples remains fairly constant. This indicates that there was no loss of mass during sintering, as may have occurred due to the evaporation of aluminium at high temperatures. The MA densities are in close relation to results by (Bolzoni, L., *et al*, 2011) and (Qangule & Knutsen, 2015) with a deviation of approximately 3 %. According to Robertson and Schaffer (2010:154), the presence of elemental Al powder in titanium powder blends, coupled with a high heating rate, may cause swelling of the compact. As the Al melts, it coats the titanium particles and leads to a rapid formation of  $TiAl_3$ , pushing the particles apart and causing swelling, which effectively decreases the density. Thus the use of a MA blend was used to avoid this which resulted in significantly higher sintered densities. As mention by Clinning and Knutsen (2012), the sintered density of a BE sample shown reached 88 %. It is noted that the heating rate used was half of that of this investigation, namely 5 °C/min, which could support the notion by Robertson and Schaffer (2010) that swelling occurred reducing the density of the sintered BE sample.

**Table 5: Green and Sintered densities**

Relative density %	Green density %		Sintered density %		Change in Density	
	Average	std dev	Average	std dev	Average	std dev
MA - 1100 °C	74.1	1.32	90.0	2.23	15.9	1.9
MA - 1200 °C	74.9	0.72	90.3	4.35	15.3	4.9
BE - 1100 °C	73.7	0.98	74.2	0.97	0.5	0.8
BE - 1200 °C	73.5	1.04	75.5	1.33	2.0	1.1

## 4.2 Infiltration Heat Treatment

Infiltration heat treatment was performed at various temperatures and dwell times as seen in Table 6. In order to evaluate whether the oxide layer on the aluminium powder particles of the compacted infiltration disks was preventing melting and the formation of a continuous liquid phase that would infiltrate the Ti-6Al-4V sample, slices of wrought aluminium disks were used as alternative infiltration disks with the mass calculated in the same manner as per the compact Al disks. The wrought Al disks showed some melting, as was observed by significant plastic deformation of the disks after the heat treatment, when heated to 900 °C under a nitrogen atmosphere with a 1 hour dwell. However, the wrought Al disks did not melt fully or infiltrate into the Ti-6Al-4V samples even at this high temperature.

Visual observation at 700 °C after the infiltration heat treatment showed that the Al infiltration disks had not melted. A higher temperature was used with a longer dwell time, which resulted with very little melting. Two possible reasons for this behaviour were considered, as presented in section 3.4. Firstly, aluminium is highly reactive so it is typical for Al powder particles to form a persistent passive oxide layer on their surface. If this oxide film is persistent during heating, it may prevent sintering and coalescence of the molten aluminium particles during heating. As mentioned in 3.4, nitrogen was used as a process gas during infiltration after no melting was observed when using argon. It was hoped that AlN would form on the pore surfaces inside the compacted Al disk, reducing the pore pressure and aiding sintering and eventual melting. However, no melting was observed when heating to 700 °C, no dwell or even to 750 °C with a 1 hour dwell under nitrogen either.

In order to evaluate whether the oxide layer on the aluminium powder particles of the compacted infiltration disks was preventing melting and the formation of a continuous liquid phase that would infiltrate the Ti-6Al-4V sample, slices of wrought aluminium disks were used as alternative infiltration disks with the mass calculated in the same manner as per the compact Al disks. The wrought Al disks showed some melting, as was observed by significant plastic deformation of the disks after the heat treatment, when heated to 900 °C under a nitrogen atmosphere with a 1 hour dwell. However, the wrought Al disks did not melt fully or infiltrate into the Ti-6Al-4V samples even at this high temperature.



**Table 6: Infiltration parameters with corresponding Al melt results**

<b>Infiltration Temperature (°C)</b>	<b>Disk Type</b>	<b>Dwell Time (hours)</b>	<b>Result</b>
700	Compact	0	No melt
750	Compact	1	Little/no melt
900	Wrought	1	Reasonable melt
900	Compact	1	Reasonable melt
900	Wrought (bottom)	1	Reasonable melt

### 4.3 Microstructural Characterisation

All samples were characterized using optical microscopy, as described in 3.6.1, as well as using SEM/EDS, as described in 3.6.3, for compositional characteristics of the microstructure. Samples from the infiltration study that occurred at 700 °C with no dwell period, and 750 °C and 900 °C both with dwell periods of 1 hour under nitrogen, were analysed as described in 3.6.1 and 3.6.3. All results showed the significant diffusion of Ti, and marginal diffusion of V, into the Al disks. By observing the wt% of Ti and V in the Al compacts using EDS analysis, and relating the data to the relevant phase diagrams, possibilities for the formation of different phases and compounds were considered. No XRD analysis was performed as the facilities are not readily available and it was considered outside of the scope of the study.

#### 4.3.1 Sintered samples (BE & CPTi+MA)

Both the BE and CPTi+MA powder blends, were vacuum sintered at 1100 °C and 1200 °C, respectively, as described in Section 3.3. No infiltration heat treatment was performed on these samples. The compositional characteristics of the sintered microstructures were analysed in terms of microstructural homogeneity and diffusion gradients for the respective elements Ti, Al, and V.

#### 4.3.1.1 1100 °C vacuum sintered

Figure 20 shows the back scatter (BS) image and elemental distribution of Ti, Al and V for the CPTi+MA sample after sintering at 1100 °C which reached a sintered density of 85.4%. A fairly homogeneous distribution is observed. High concentrations of V are found within the matrix. Al has a high solubility in Ti, and therefore it is probable that Al leached out of the MA powder particles into the Ti powder particles. Figure 21 shows the back scatter image and elemental distributions of the BE sample, sintered at 1100 °C which reached a sintered density of 72.9%. The microstructure has a significantly more inhomogeneous composition as compared to the CPTi+MA sample 1. Large concentrations of Al are present around the larger pores, indicating that individual Al particles melt and rapidly diffuse into the matrix, leaving behind large pores. High concentrations areas of V are observed, due to the diffusion of Al out into the matrix. Literature has indicated that the diffusion of V is hindered as the diffusion of Al increases; hence the V has not fully diffused into the Al or the Ti.

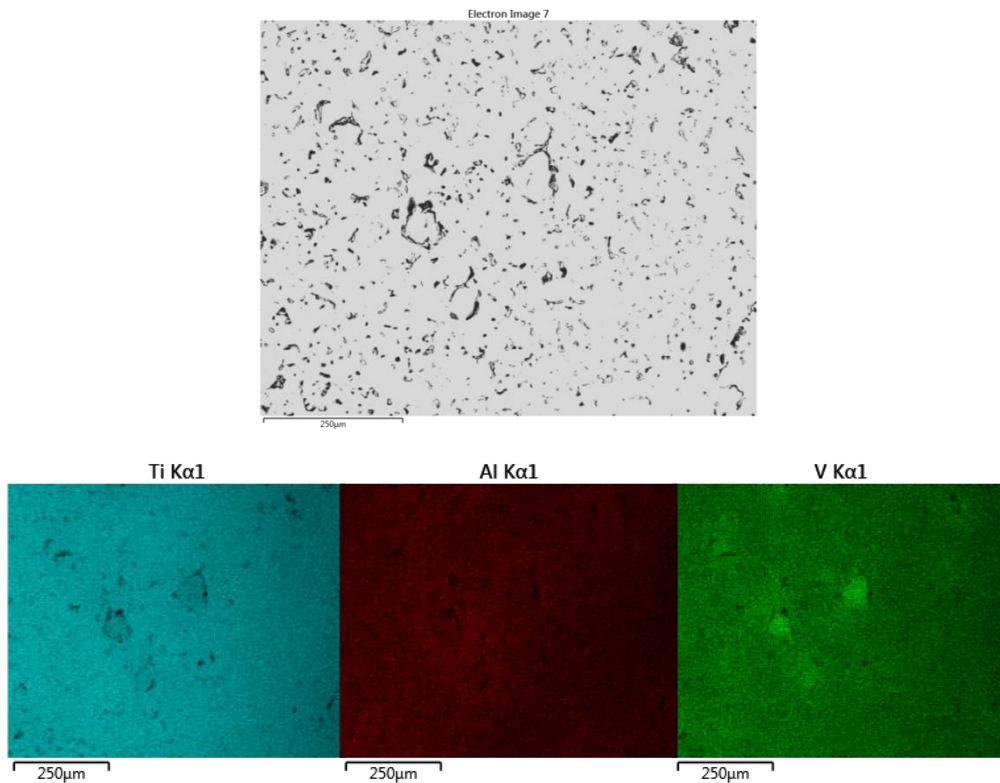


**Figure 20: EDS map CPTi+MA 1100 °C vacuum sintered, unfiltered**

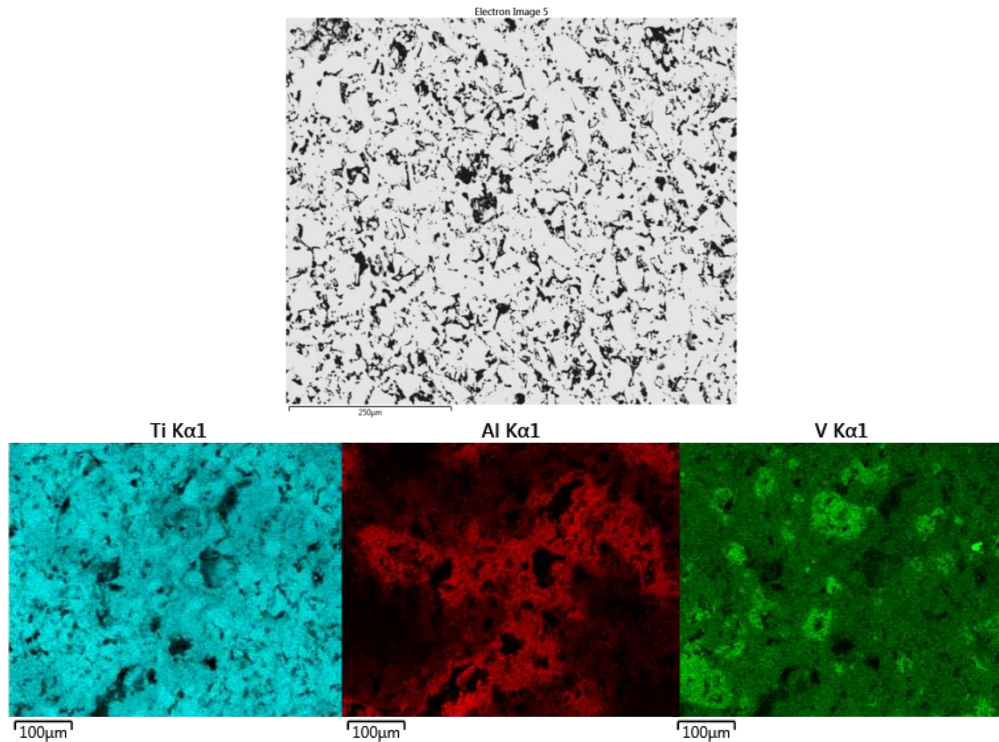


**Figure 21: EDS map BE 1100 °C vacuum sintered, unfiltered**

#### 4.3.1.2 1200 °C vacuumed sintered

Figure 22 and Figure 23 show the BS images and elemental distribution of Ti, Al, and V, for the MA and BE samples, respectively, after sintering at 1200 °C as compared to 1100 °C (Figure 20 and Figure 21). The samples had a relative sintered density of 92.2% and 74.4%, respectively. It is evident that the elements are more homogeneously distributed. At a higher sintering temperature, there is a higher diffusion rate which would aid in evening out elemental concentration gradients, resulting in a more homogeneous elemental distribution. Figure 22 shows that the MA particles have diffused well into the Ti matrix, creating a fully alloyed Ti-6Al-4V microstructure, with little to no high concentration pockets visible. Figure 23 shows that the BE sintered microstructure is still inhomogeneous, but is better as compared to the sample sintered at 1100 °C (Figure 21). Large pores compared to the CPTi+MA samples are still visible from Al diffusing into the matrix as well as high concentrations of V present as the diffusion rate of V was hindered by the diffusion rate of Al.

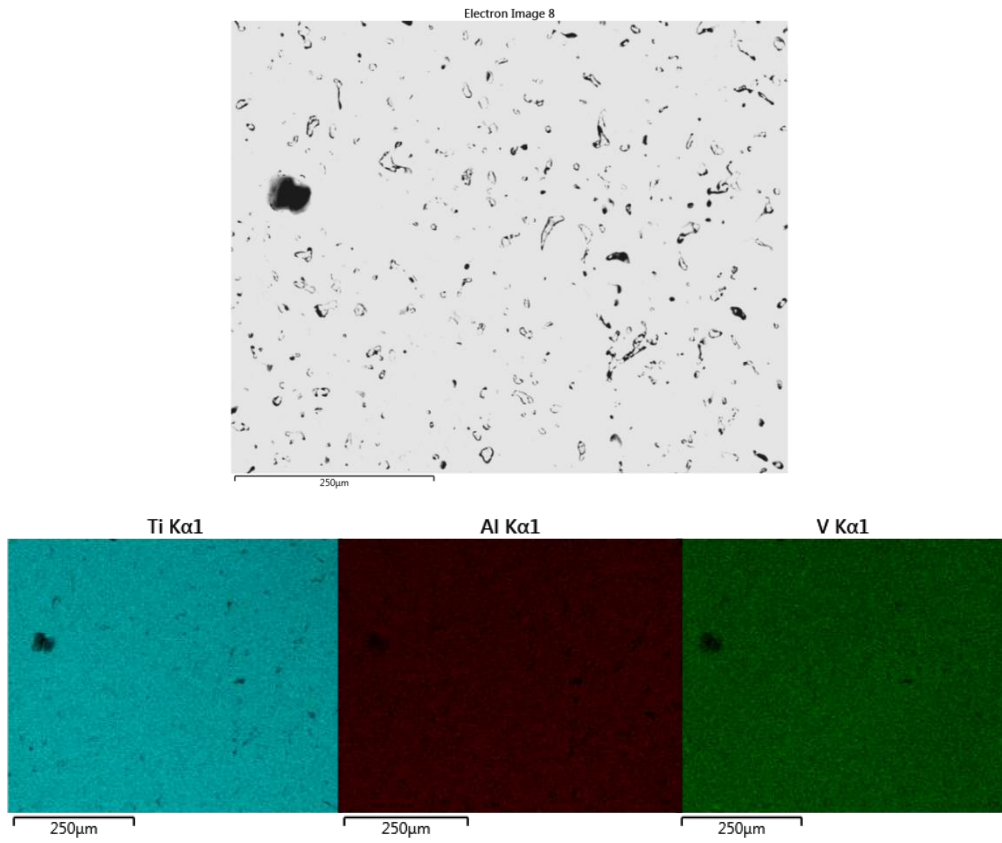


**Figure 22: EDS map CPTi+MA 1200 °C vacuum sintered, uninfiltred**

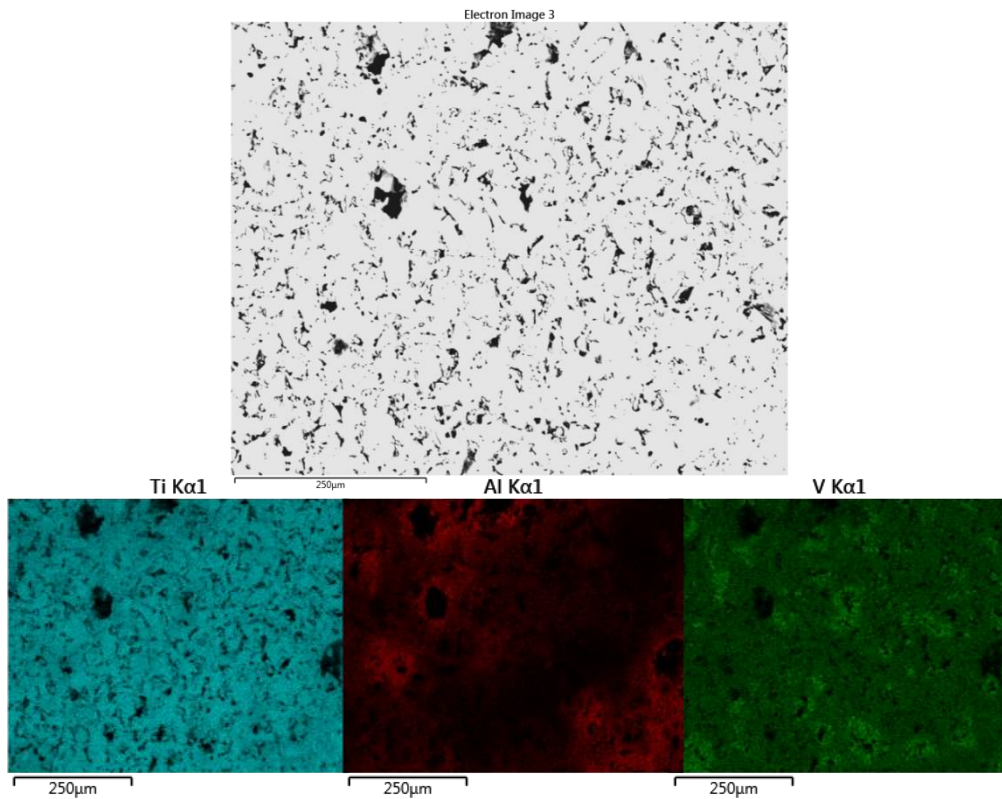


**Figure 23: EDS map BE 1200 °C vacuum sintered, uninfiltred**

### 4.3.2 1100 °C Sintered and 700 °C Infiltrated Samples (BE and CPTi+MA, Powder Al Compact)

Both CPTi+MA and BE powder blends were vacuum sintered at 1100 °C for 2 hours and then furnace cooled, after which the infiltration attempt was performed at 700 °C with no dwell period i.e. cooled immediately after the peak temperature was reached, with a compacted piece of aluminium placed above the Ti-6Al-4V sintered sample. Nitrogen was included in the EDS analysis of the infiltrated samples, Sections 4.3.2 to 4.3.8, in order to determine whether the nitrogen atmosphere during the infiltration heat treatment affected the chemical composition of the sample.

#### 4.3.2.1 CPTi+MA sample

Figure 24 shows the BS images and elemental map of the Ti-6Al-4V sample (sintered density of 89.5%) at the edge that had been in contact with the compacted Al disk, with the compositions of Ti, Al, V and N. The bottom of the images represents the top of the sample where the interface of the Al compact was in contact with the Ti-6Al-4V sample. The Al powder compact did not melt during the infiltration heat treatment. From the images it is seen that a fairly homogeneous composition is present with the nitrogen having infiltrated throughout the entire matrix. The small pores present, as compared with the previous CPTi+MA sintered at 1100 °C shown in Figure 20, are an indication of the increased sintered density. The fact that pores are present in all images indicates infiltration with molten Al did not occur. The high concentration of Al seen may be from the Al within the master alloy present, and not from infiltration. Figure 25 is the EDS line analysis showing compositional variation in the region of a pore within the Ti-6Al-4V matrix. As seen there is increased nitrogen detected on the pore surfaces, that corresponds with increased levels of Ti and Al. Where higher concentration of V is observed, the N concentration decreases.

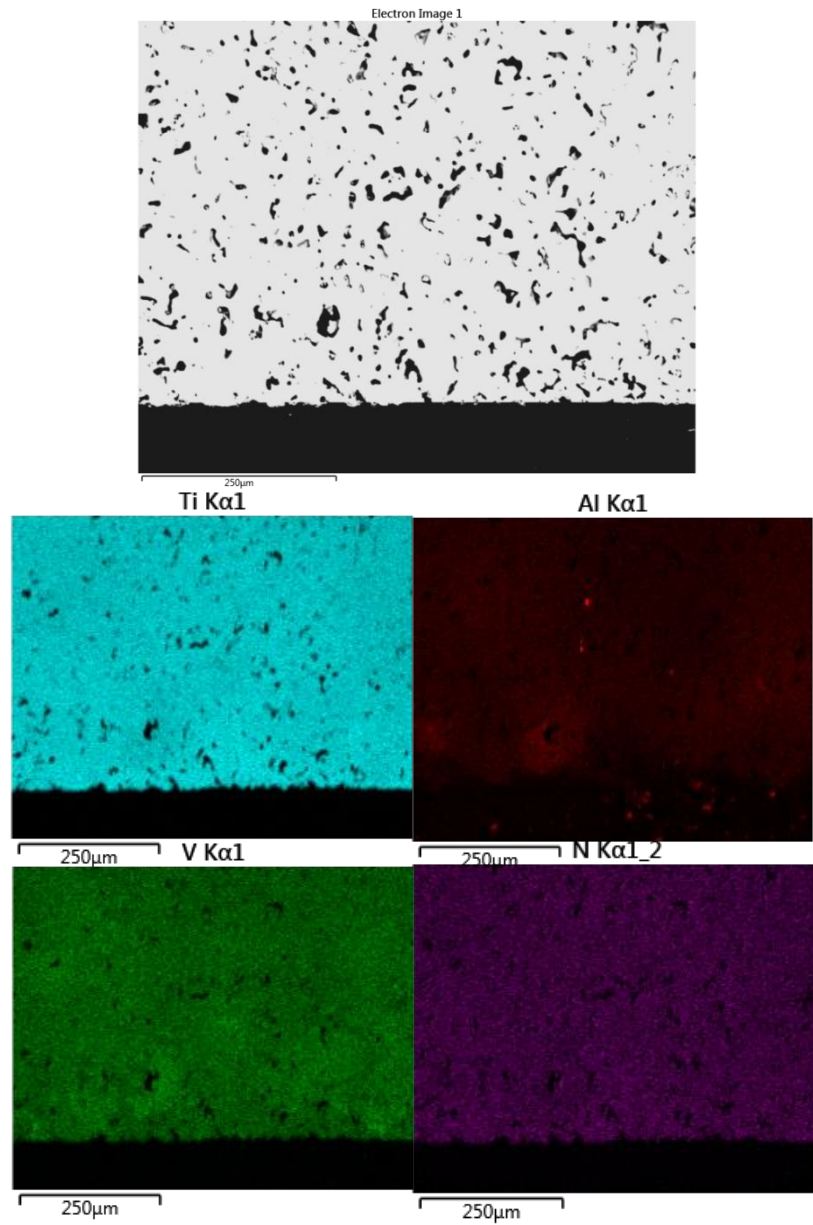


**Figure 24: EDS map CPTi+MA 1100 °C sintered, 700 °C infiltration heat treatment, no dwell**

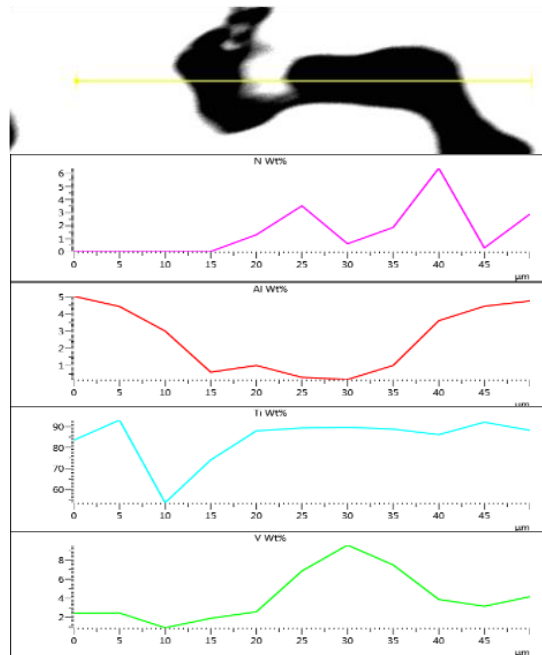


**Figure 25: EDS line distribution through pore of CPTi+MA, 700 °C infiltration heat treatment, no dwell**

#### 4.3.2.2 BE sample

Figure 26 shows the BS images and elemental distribution of the 1100 °C sintered, 700 °C infiltration heat treated BE sample, within the Ti-6Al-4V matrix which reached a sintered density of 75.0%. The presence of unfilled large pores, as compared to the previous BE sample sintered at 1100 °C shown in Figure 21, explains the low density. The presence of these large pores indicates that as the Al powder particles melted, the liquid Al diffused rapidly into the surrounding Ti and V particles, leaving large pores behind. This hypothesis is supported by the high concentrations of Al outside the pores, seen in Figure 26. High V concentrations can be seen on smaller pores. This is an indication of the V diffusing in the solid state into the Ti particles, but its diffusion hindered by the presence of Al as explained in section 2.2.1.

Nitrogen is seen to have infiltrated through the matrix. Figure 27 shows the EDS line scan composition through a pore in the matrix. Higher N concentrations are present along the pore surface, with N peaks corresponding to higher concentrations of Al and Ti, and practically no N found in high V regions.

The large crack present in this case occurred during the metallographic preparation stage when high forces were used to polish and grind the sample. When the grinding forces was reduced, subsequent samples did not show similar cracks.

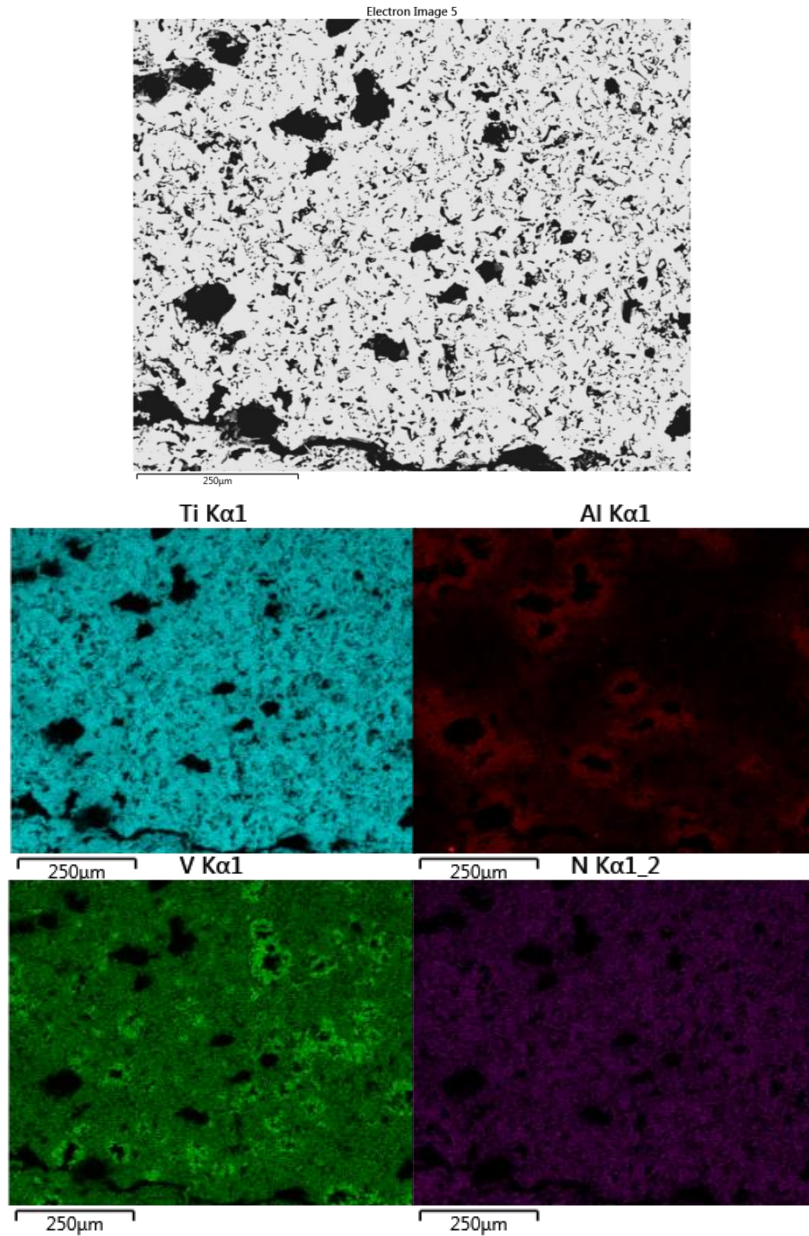


**Figure 26: EDS map BE 1100 °C sintered, 700 °C infiltration heat treatment, no dwell**



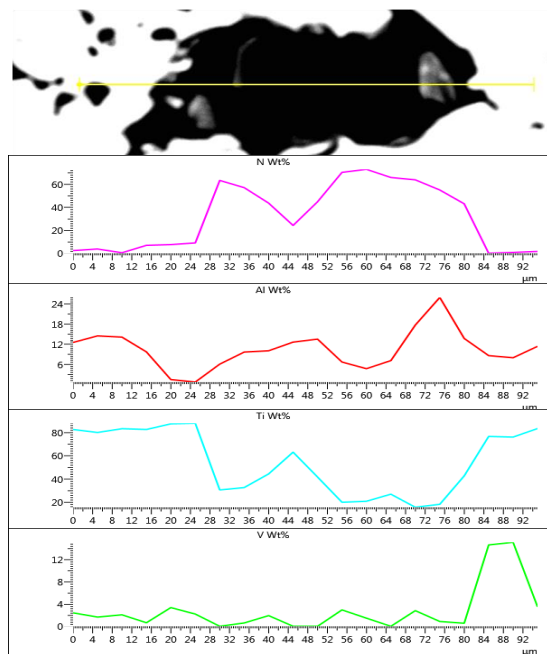


**Figure 27: EDS line distribution through pore of BE, 700 °C infiltration heat treatment, no dwell**

#### 4.3.3 1100 °C Sintered and 750 °C Infiltrated Samples (BE and CPTi+MA, Powder Al Compact)

CPTi+MA and BE powder blends were vacuum sintered at 1100 °C for 2 hours and then furnace cooled, after which the infiltration attempt was performed at 750 °C with 1 hour dwell period with a compacted piece of aluminium placed above the Ti-6Al-4V sintered sample.

##### 4.3.3.1 CPTi+MA sample

Figure 28 shows the BS images and elemental maps of Ti, Al, V and N of the MA blend which reached a sintered density of 90.3%. The figure shows a very homogeneous composition as the master alloy diffused into the Ti during the sintering process. The Al disk did not melt enough to infiltrate. The N has infiltrated throughout the entire matrix which suggest the diffusion of N in Al within pores. Figure 29 shows the EDS line scan through a pore, showing peaks of N and Al occurring at the same place, corresponding to a drop in Ti and V. A high concentration of V is observed outside the pore to the left suggesting diffusion of the V out of the MA particles into the Ti. On the right side of the pore we see an increase of V diffusion as the Al diffusion decreases.

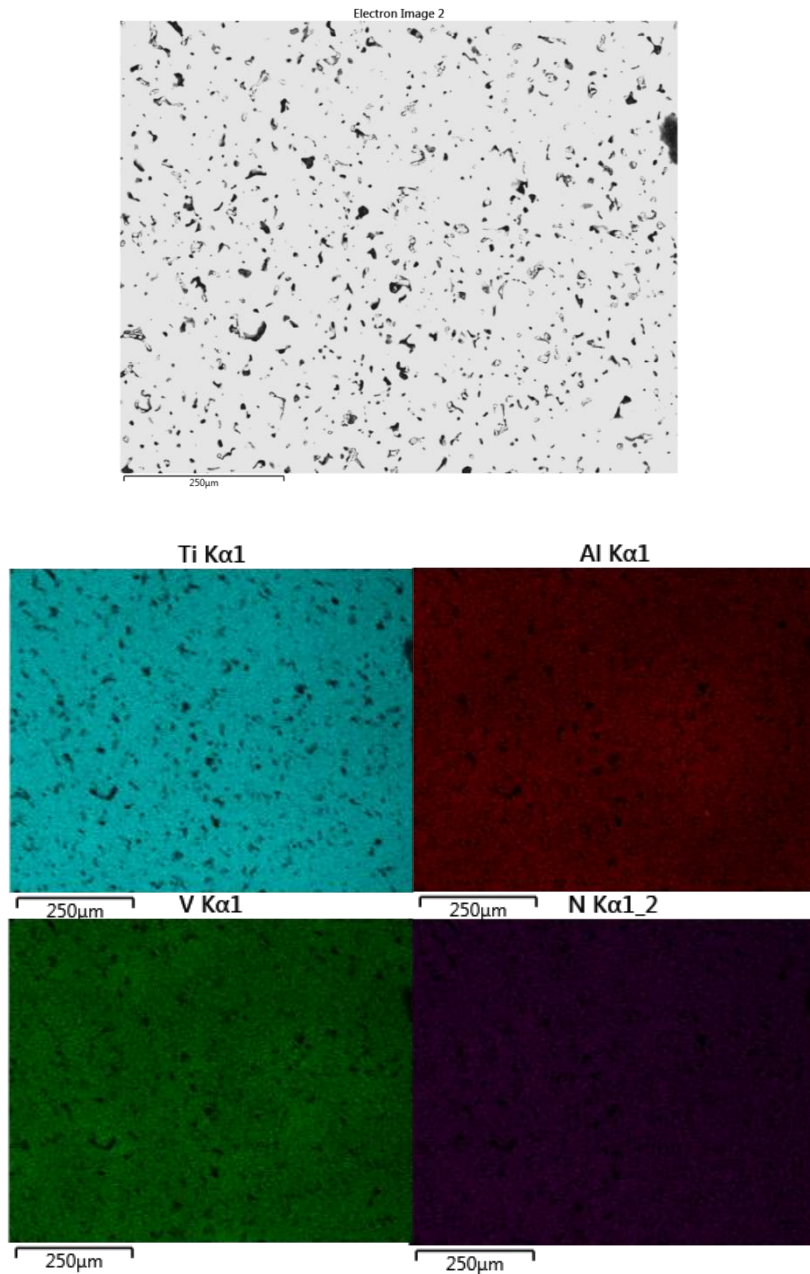


**Figure 28: EDS map CPTi+MA 1100 °C sintered, 750 °C infiltration heat treatment, 1 hr dwell**

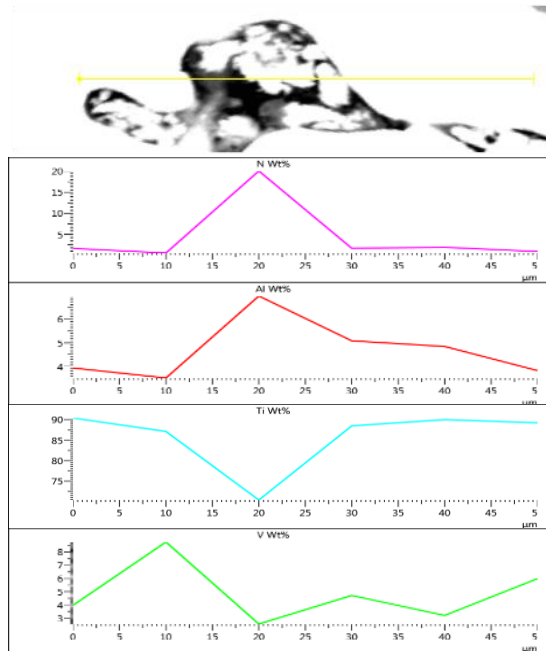


**Figure 29: EDS line distribution through pore of CPTi+MA 1100 °C sintered, 750 °C infiltration heat treatment, 1 hr dwell**

#### 4.3.3.2 BE sample

Figure 30 shows the BS images and elemental distribution of the BE sample, sintered at 1100 C and infiltration heat treated at 750 C, which reached a sintered density of 73.1%. It can be observed that the Al and V not having diffused completely into the Ti, leaving high concentrations of Al and V. Large pores as compared to previous BE samples are visible from the diffusion of Al particles out into the matrix as the temperature of infiltration and sintering were that above the melting point of Al. The high concentration of Al outside the pores show as the Al particles rapidly diffused into Ti and V large pores were present as a result. The V is seen to diffuse into the matrix but is hindered by the increasing Al diffusion. Figure 31 shows the diffusion of N at the pore surface. Here we see the line scan peaks aligned suggesting diffusion of N into Al and V.

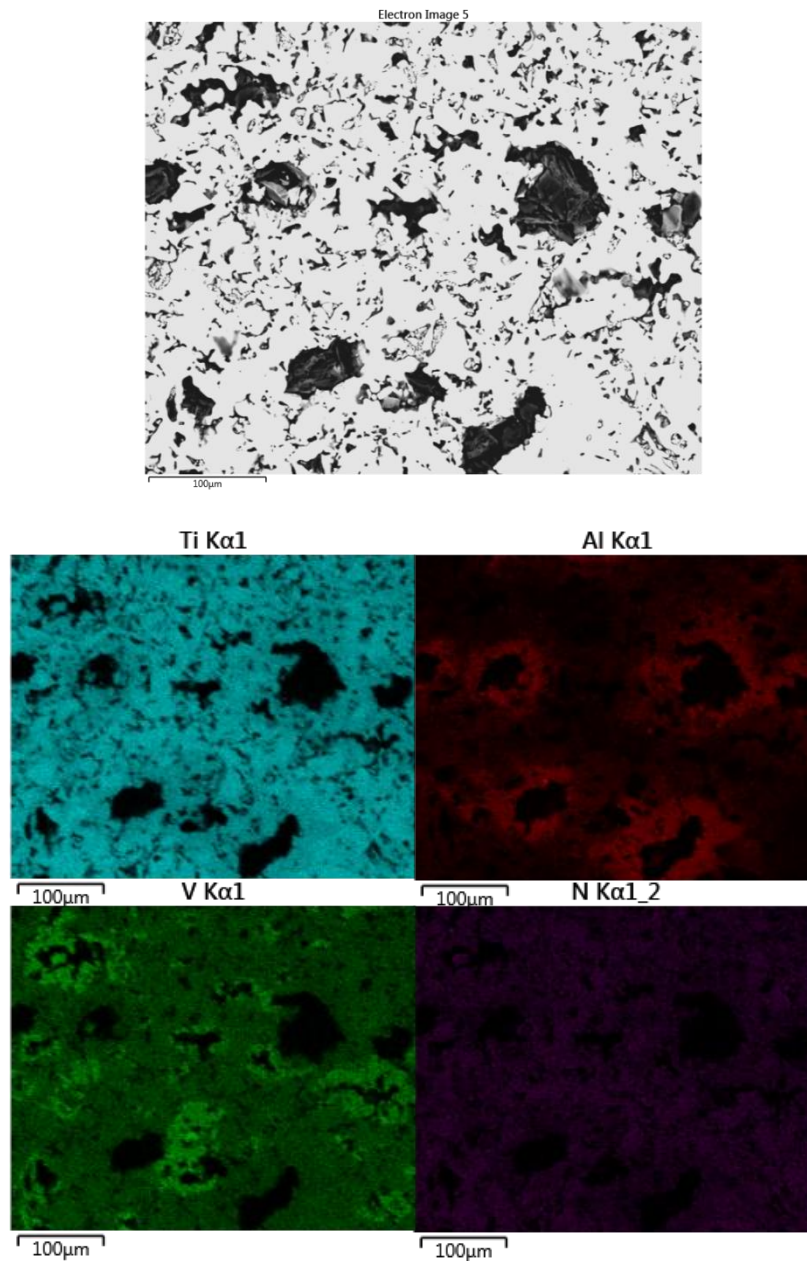


**Figure 30: EDS map BE 1100 °C sintered, 750 °C infiltration heat treatment, 1 hr dwell**

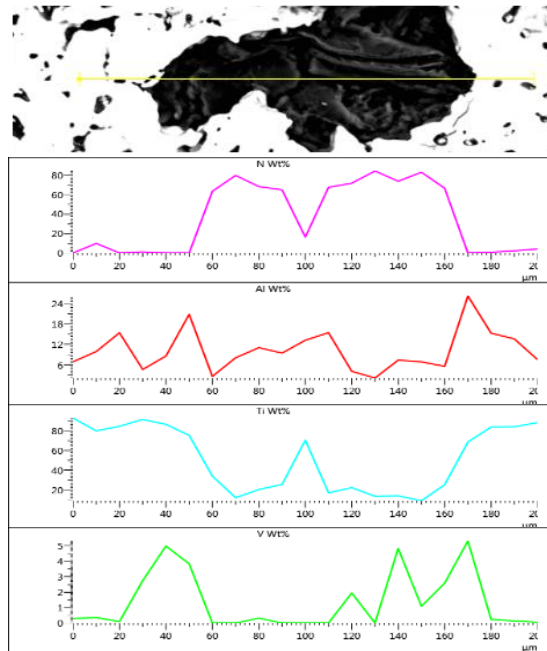


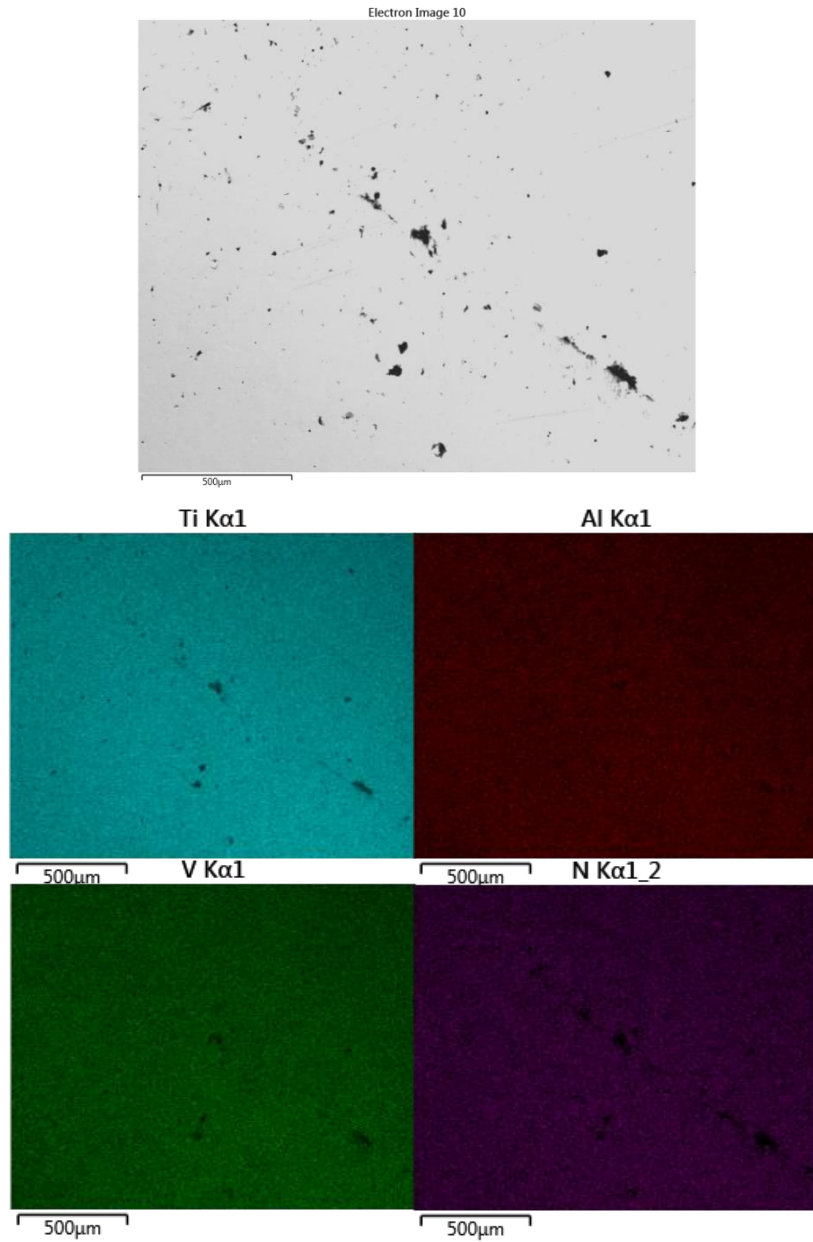
**Figure 31: EDS line distribution through pore of BE 1100 °C sintered, 750 °C infiltration heat treatment, 1 hr dwell**

#### 4.3.4 1200 °C Sintered and 750 °C Infiltrated Samples (BE and CPTi+MA, Wrought Al Disk)

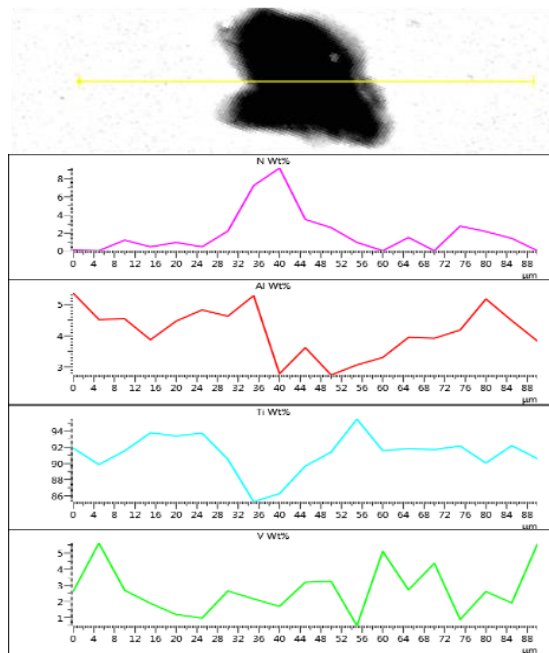
CPTi+MA and BE powder blends were vacuum sintered at 1200 °C for 2 hours and then furnace cooled, after which the infiltration attempt was performed at 750 °C with 1 hour dwell period with a wrought piece of aluminium placed above the Ti-6Al-4V sintered sample. The Al disk did melt somewhat, yet did not infiltrate.

##### 4.3.4.1 CPTi+MA sample

Figure 32 is that of the CPI+MA sample BS images sintered at a higher temperature to samples mentioned previously, hence showing the homogenous composition and a sintered density of 82.3% was achieved. For this sample a wrought Al disk was placed on top of the sample rather than a compacted Al disk. N infiltrated the matrix, as presently seen. Figure 33 shows the EDS line scan through a pore. Again, it appears that N has diffused onto the pore surface with high concentrations of N aligning with high Al concentrations. High V concentrations are seen in the region of the pore inside the Ti-6Al-4V matrix, indicating that Al diffused out of the MA particle leaving the prior MA particle with a higher concentration of V.



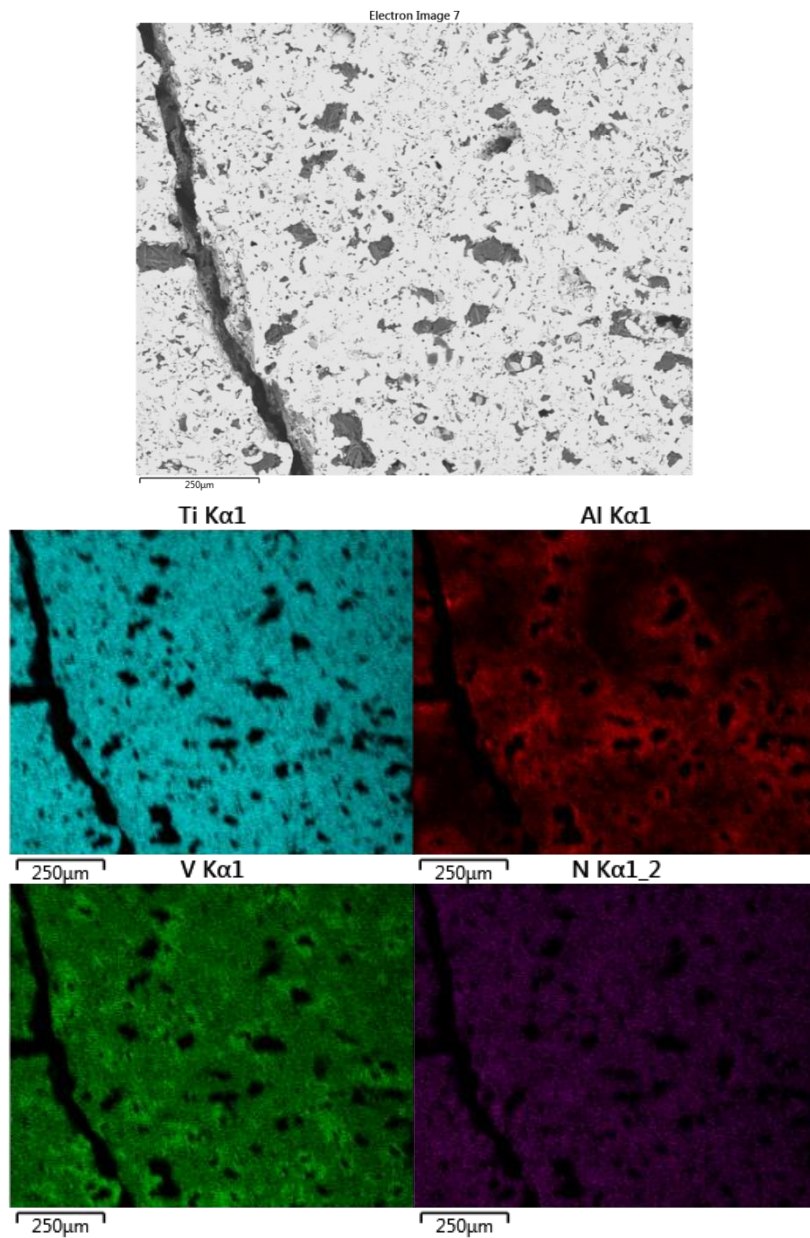
**Figure 32: EDS map CPTi+MA 1200 °C sintered, 750 °C infiltration heat treatment, 1 hr dwell**



**Figure 33: EDS line distribution through pore of CPTi+MA 1200 °C sintered, 750 °C infiltration heat treatment, 1 hr dwell**

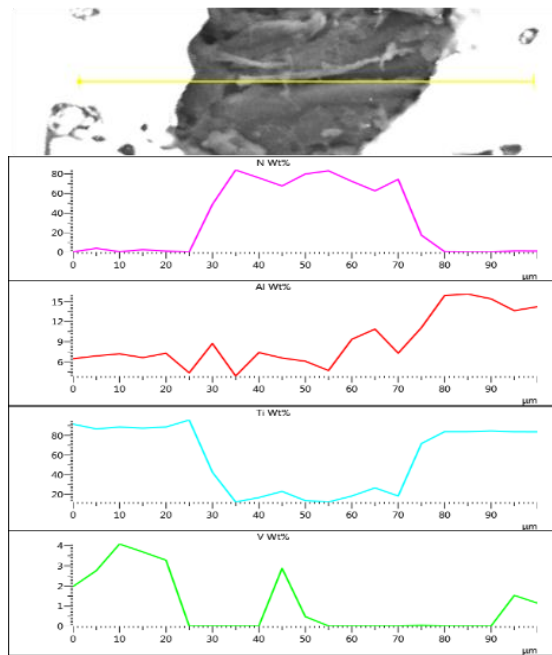
#### 4.3.4.2 BE sample

Figure 34 shows the BS images and elemental distribution of the BE blend of sample 5 which reached a sintered density of 74.2% with large concentrations of Al surrounding large pores, in comparison to previous BE samples characterized, of which were created by Al particles rapidly diffusing into the matrix. Again, the large crack was attributed to the low sintered density of the elemental blend being subjected to a high force during metallographic processes. Figure 35 shows the EDS line distribution through a pore. Here, high concentrations of N align with Al and low levels of V. Ti is not present along the pore surface but high concentrations are found outside the pore in the sintered matrix, along with increasing Al, probably an artefact of the diffusion of molten Al during sintering.



**Figure 34: EDS map BE 1200 °C sintered, 750 °C infiltration heat treatment, 1 hr dwell**





**Figure 35: EDS line distribution through pore of BE 1200 °C sintered, 750 °C infiltration heat treatment, 1 hr dwell**

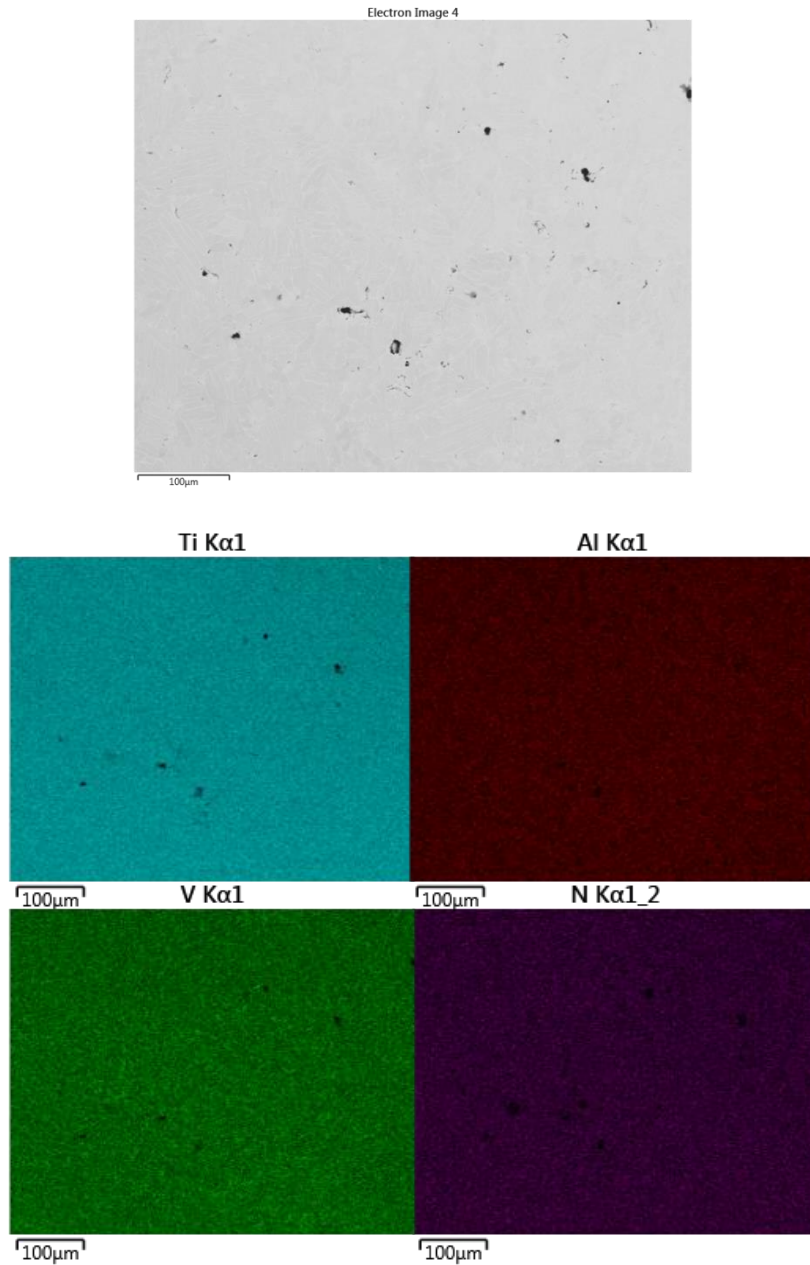
#### 4.3.5 1200 °C Sintered and 900 °C Infiltrated Samples (BE and CPTi+MA, Wrought Al Disk)

CPTi+MA and BE powder blends were vacuum sintered at 1200 °C for 2 hours and then furnace cooled, after which the infiltration attempt was performed at 900 °C with 1 hour dwell period with a wrought piece of aluminium placed above the Ti-6Al-4V sintered sample. At a higher infiltration temperature the Al disk melted more so than before, but did not infiltrate the matrix. Nevertheless, it was clear that some diffusion bonding between the Al disk and the Ti-6Al-4V sample had occurred which was a noticeable difference to the samples that were subjected to the infiltration heat treatment at lower temperatures.

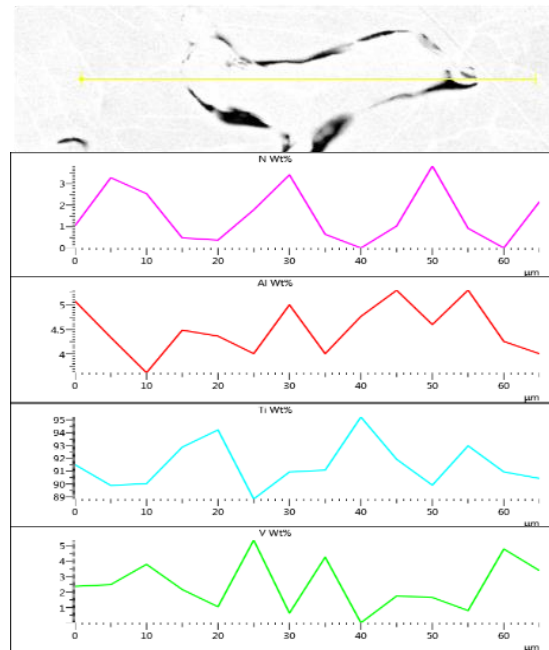
##### 4.3.5.1 CPTi+MA sample

Figure 36 shows the BS images and elemental map for the CPTi+MA blend which reached a sintered density of 89.9%. It should be noted that the microstructure shown in Figure 36 indicates a lower residual porosity than expected when considering the sintered density. However, there were other areas of the samples that displayed higher levels of residual porosity which would account of the bulk density of the entire sintered sample. As seen a homogeneous composition is visible with very small pores present, as apparent in previous CPTi+MA samples sintered at 1200 °C, as a result of the high sintered density. No visible pockets of

elements have formed. As no Al pockets have formed no infiltration has taken place even at higher infiltrating temperatures. N is seen to have infiltrated throughout the matrix leading to the suggested diffusion of N within the matrix.



**Figure 36: EDS map CPTi+MA 1200 °C sintered, 900 °C infiltration heat treatment, 1 hr dwell**



**Figure 37: EDS line distribution through pore of CPTi+MA 1200 °C sintered, 900 °C infiltration heat treatment, 1 hr dwell**

#### 4.3.5.2 BE sample

Figure 38 shows the BS images and elemental map of the BE blend which reached a sintered density of 74.1%. The density is similar to the original green density. Large pores, as similar to previous samples investigated, have formed once again from Al particle melting and rapidly diffusing into the matrix. High Al concentrations are found in the matrix in the region of the pore surface. High concentrations of V are found to correspond with low Al concentrations, as V diffusion was hindered by the presence of Al in the microstructure. N has infiltrated throughout the matrix suggesting diffusion of N within the matrix as seen in Figure 39. On the pore surface small amounts of N are detected that align with higher levels of Al and V, while no Ti is present at this pore surface.

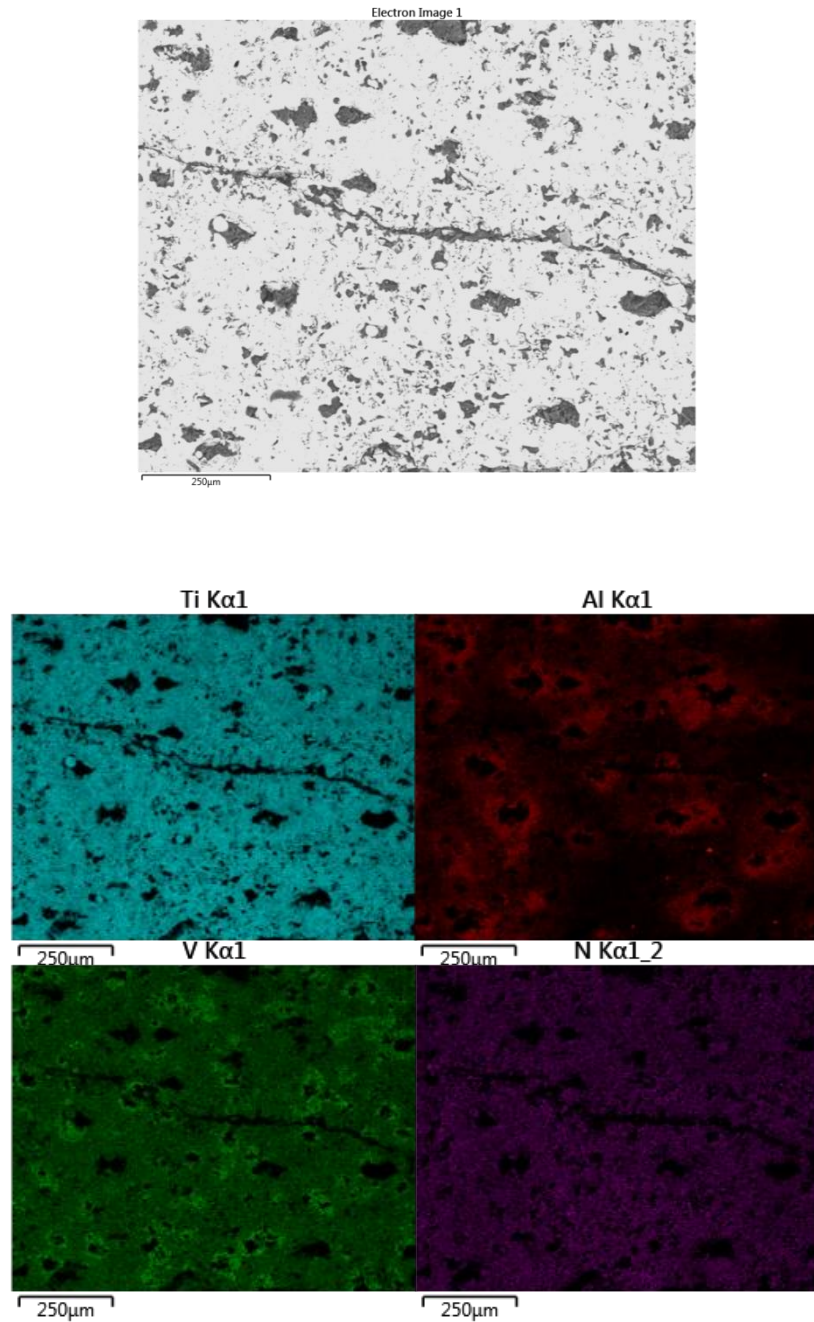


**Figure 38: EDS map BE 1200 °C sintered, 900 °C infiltration heat treatment, 1 hr dwell**

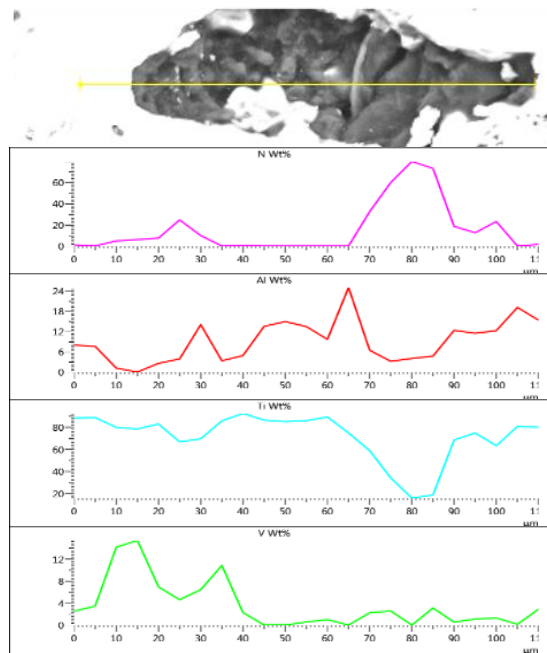


**Figure 39: EDS line distribution through pore of BE 1200 °C sintered, 900 °C infiltration heat treatment, 1 hr dwell**

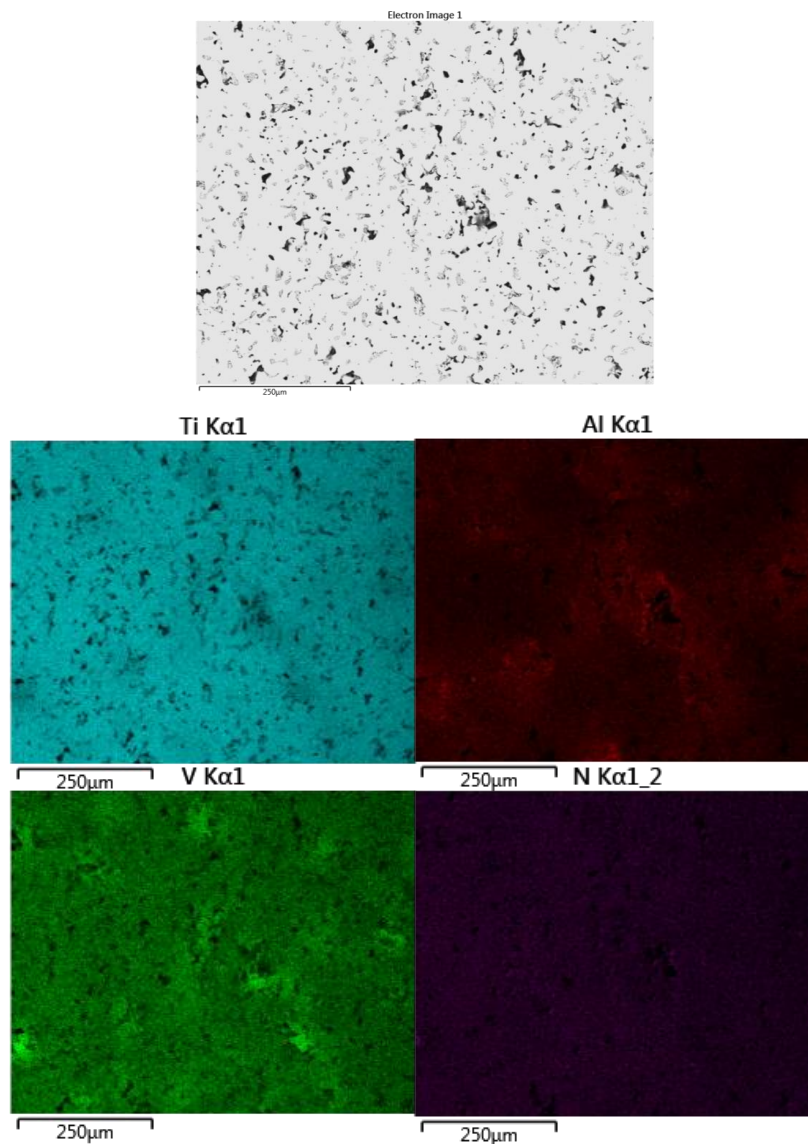
#### 4.3.6 1100 °C Sintered and 900 °C Infiltrated Samples (BE and CPTi+MA, Wrought Al Disk)

CPTi+MA and BE powder blends were vacuum sintered at 1100 °C for 2 hours and then furnace cooled, after which the infiltration attempt was performed at 900 °C with 1 hour dwell period with a wrought piece of aluminium placed below the Ti-6Al-44V sample.

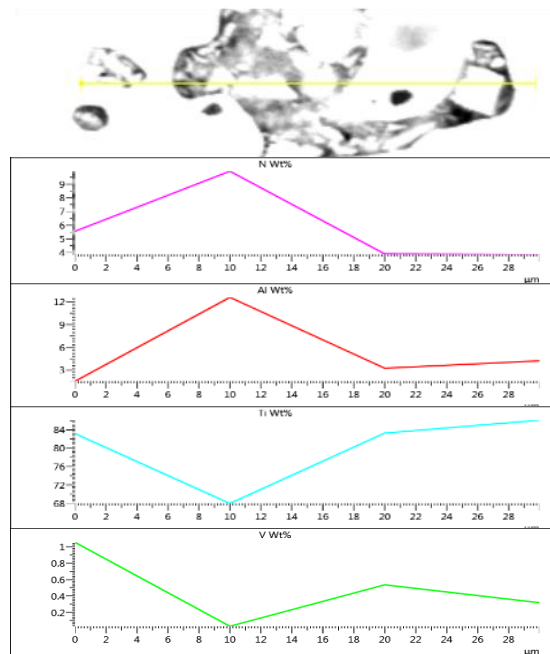
##### 4.3.6.1 CPTi+MA sample

Figure 40 and show the BS images and elemental map of the CPTi+MA blend which reached a sintered density of 91.9% hence the presence of small pores. For this sample, the matrix does not seem as homogeneous as previous samples investigated. There are high concentration pockets of Al, yet no pores are filled indicating no infiltration. The high V concentrations relate to the Al diffusing out of the master alloy leaving high concentrations of V in the prior master alloy particle. N has infiltrated the matrix, and Figure 41 shows the EDS line scan composition through a pore. Again, high concentrations of N align with Al peaks on the pore surface, and peaks of V and Ti correspond to low N concentration.

Figure 42 shows the SEM/EDS analysis of the Al disk that was placed beneath the Ti-6Al-V sample during the 900 °C infiltration heat treatment. Here we can clearly see that, even though the Al disk did not melt and so no infiltration took place, Ti, V and N from the system have diffused into the Al disk. The diffusion of Ti into Al, although limited, was also observed in the studies by (Xu, L., *et al* 2006) and (Xu, X., *et al* 2014). By observing the wt% of Ti in the Al disks, which is found in Figure 77 as around 35 wt% Ti, and relating it to the Ti-Al phase diagram, we see in theory that an intermetallic may have formed with a melting temperature >1000°C which gives reason as to why the Al disks do not melt fully. At the top of the sample we see a high concentration of N that corresponds to a high concentration of Al, and almost no Ti or V. Given the negligible solubility of N in Al, this would indicate that AlN has formed as a new phase. This corresponds with the dark grey region seen on the BS image. It is noted that the bottom of Figure 42 corresponds to the top of the Al sample exposed to the furnace.



**Figure 40: EDS map CPTi+MA 1100 °C sintered, 900 °C infiltration heat treatment, 1 hr dwell**



**Figure 41: EDS line distribution through pore of CPTi+MA 1100 °C sintered, 900 °C infiltration heat treatment, 1 hr dwell**

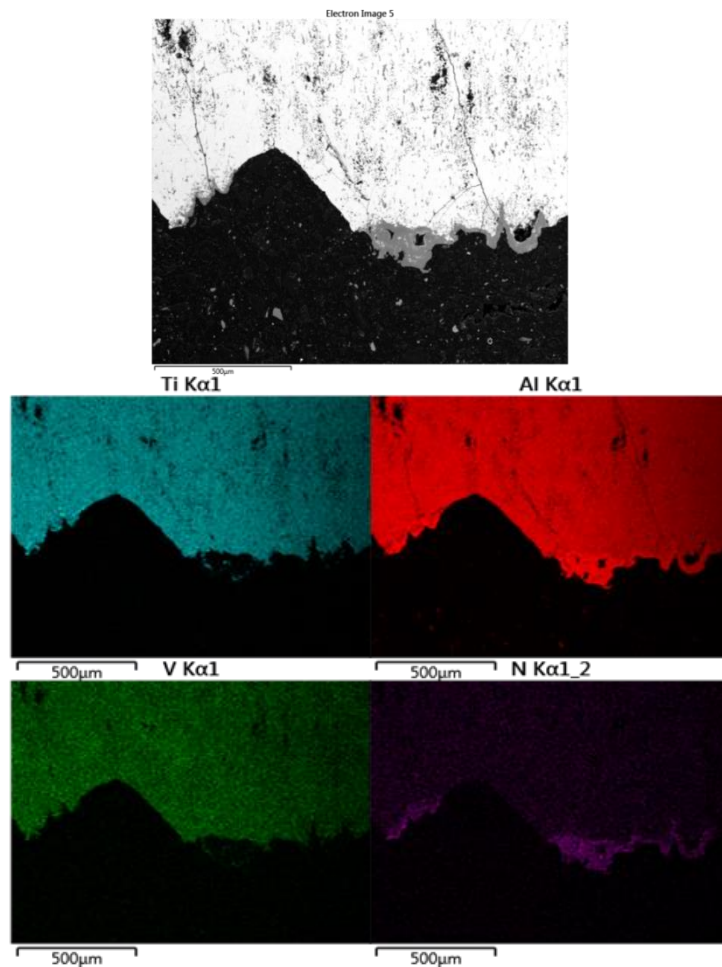


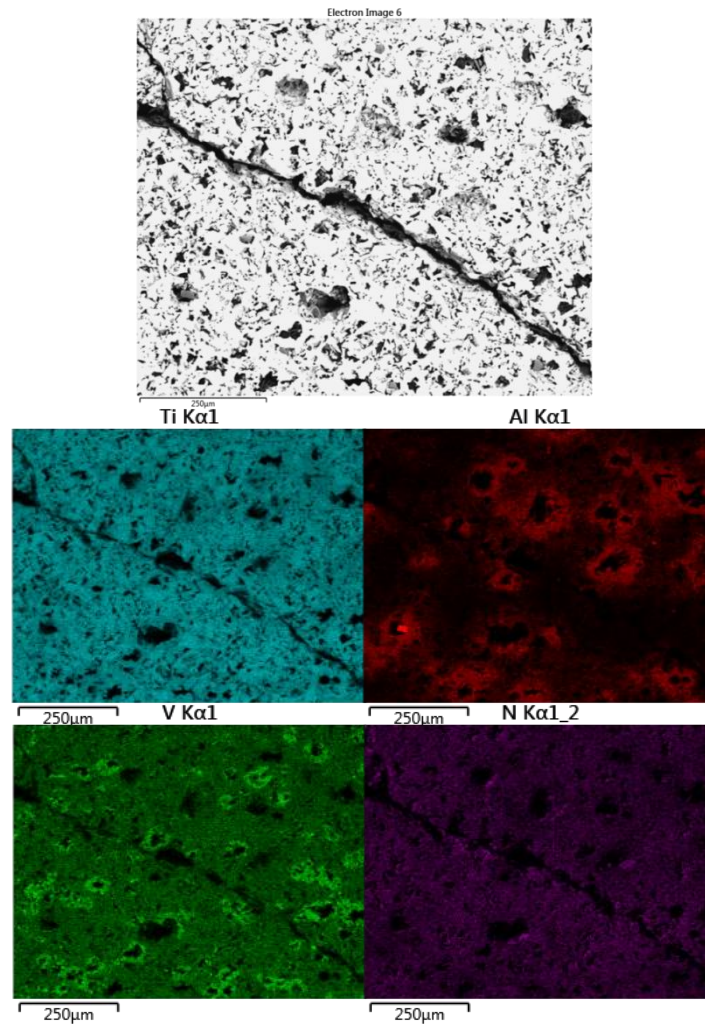
**Figure 42: EDS map CPTi+MA Al disk, 900 °C infiltration heat treatment, 1 hr dwell**

#### 4.3.6.2 BE sample

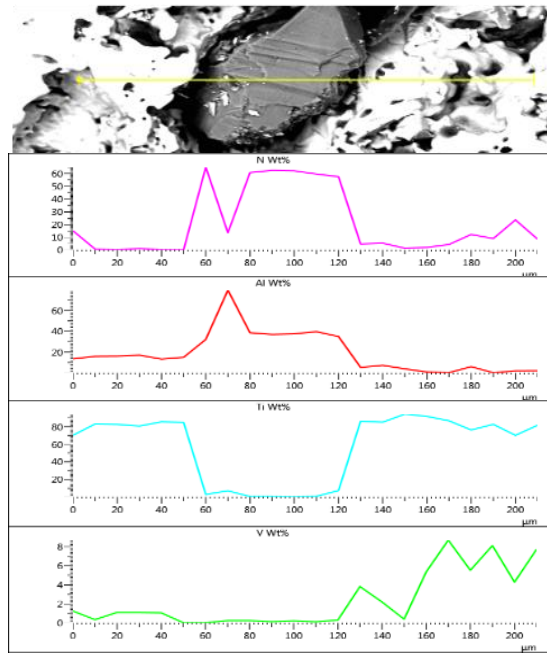
Figure 43 and Figure 45 show the BS images and elemental map of the BE blend and Al disk, respectively, with the BE sample reaching a sintered density of 73.9%. We observe the large pores from the Al particles, as compared to previous BE samples investigated, diffusing into the matrix creating these pores, hence the high Al concentration outside the visible pores. High concentrations of V are observed as it begun diffusing out yet was hindered from Al diffusing. Since the sintered density was so low, the strength of the material did not change much from the compacted sample, hence the presence of a large crack which was formed from the high rotational force applied during mettalographic processes. Figure 45 shows the Al disk with clear indication of the diffusion of Ti and V into the Al. It is evident Ti and V diffused into the Al disk however the disk did not melt or infiltrate the pores of the Ti-6Al-4V sample. As the solubility of both Ti and V in Al are very low, it is possible that intermetallic compounds  $TiAl_3$ , and  $Al_{21}V_2$  may have formed, thus raising the melting temperature of the Al disk above the heat treatment temperature. This would explain why none of the Al disks melted. Further phase analysis, using XRD, would confirm this hypothesis.

Figure 44 shows the EDS line scan through a pore in the BE Ti-6Al-4V matrix. A clear second phase particle is shown within the pore that corresponds to peaks of Al and N, again pointing to the formation of AlN on the pore surface.





**Figure 43: EDS map BE 1100 °C sintered, 900 °C infiltration heat treatment, 1 hr dwell**



**Figure 44: EDS line distribution through pore of BE 1100 °C sintered, 900 °C infiltration heat treatment, 1 hr dwell**

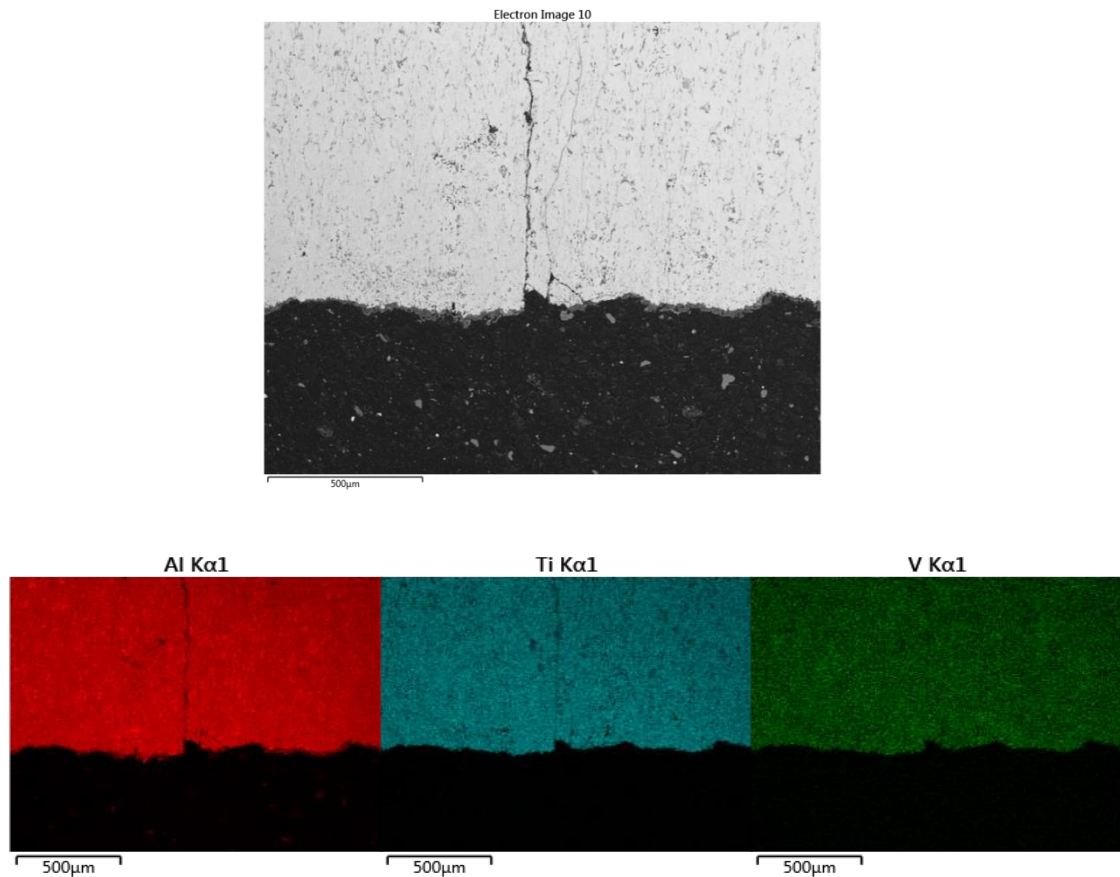


**Figure 45: EDS map BE Al disk, 900 °C infiltration heat treatment, 1 hr dwell**

#### **4.3.7 1100 °C Sintered and 900 °C Infiltrated Samples (BE and CPTi+MA, Powder Al Compact)**

CPTi+MA and BE powder blends were vacuum sintered at 1100 °C for 2 hours and then furnace cooled, after which the infiltration attempt was performed at 900 °C with 1 hour dwell period with a compacted piece of aluminium placed above the Ti-6Al-4V sintered sample.

##### **4.3.7.1 CPTi+MA sample**

Figure 46 shows the BS images and elemental distribution of Ti, Al, V and N of the CPTi+MA blend. As this was taken at a much higher magnification the pores look much larger in comparison to other CPTi+MA samples. The small pores relate to the high sintered density which was 90.6%. The sample is seen to be homogeneous with no infiltration occurring. One may also notice the small spots of V which have a high concentration, which is due to the Al diffusing out of the master alloy. N has diffused throughout the matrix. As observed from Figure 47, which shows the EDS line scan through a pore in the Ti-6Al-4V matrix, high concentrations of Al and N occur in the same region, close to the pore surface in the matrix. Other images show concentrations of Ti and V aligning with N along the pore surface.

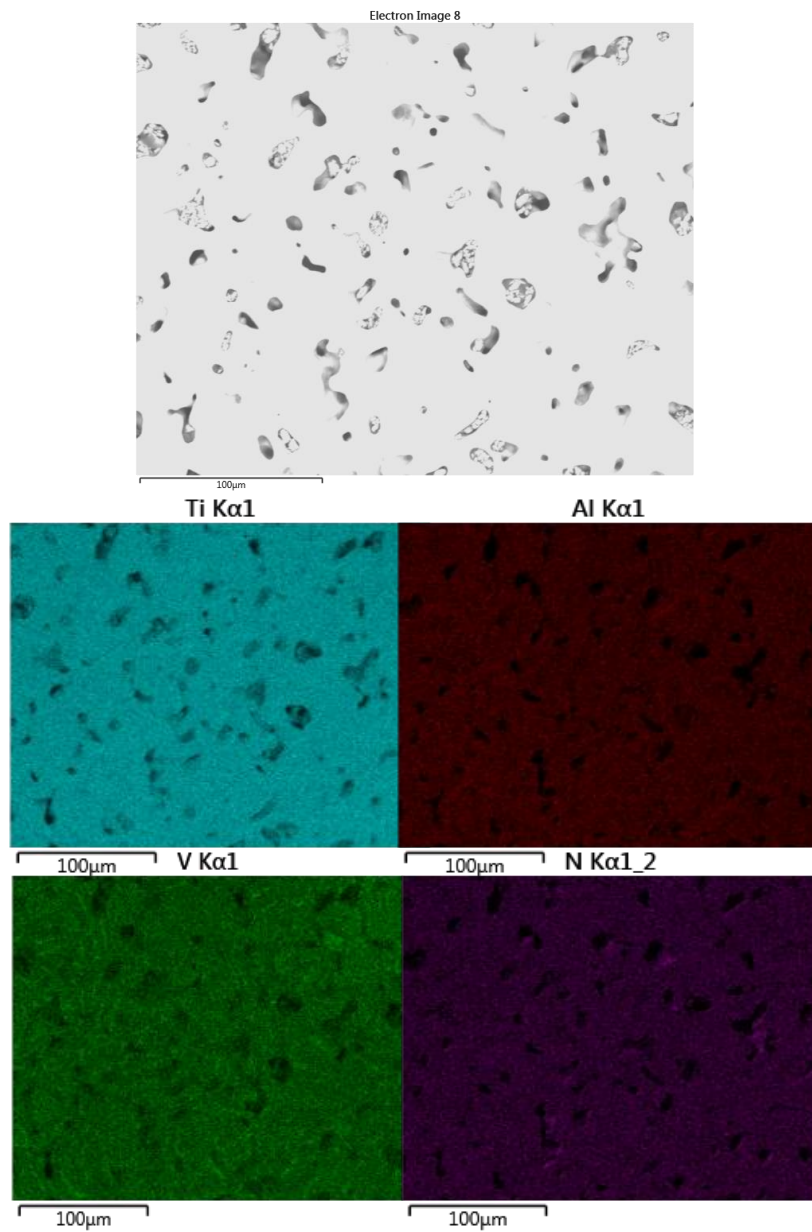


**Figure 46: EDS map CPTi+MA 1100 °C sintered, 900 °C infiltration heat treatment, 1 hr dwell**

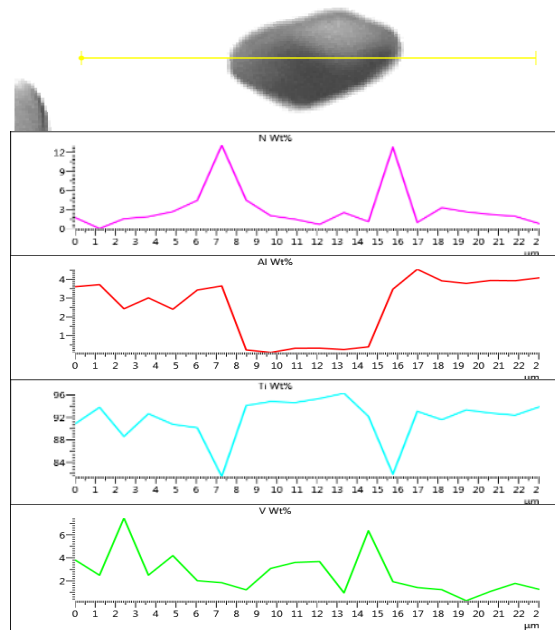


**Figure 47: EDS line distribution through pore of CPTi+MA 1100 °C sintered, 900 °C infiltration heat treatment, 1 hr dwell**

#### 4.3.7.2 BE sample

Figure 48 shows the BS images and BE elemental composition which had a sintered density of 74.8%. Very high concentrations of Al are visible outside the pores from the diffusion of Al particles into the matrix. We observe V pockets formed as V started to diffuse yet hindered by Al diffusion. N has diffused into the entire matrix. Figure 49 shows the suggested diffusion of N in Al and V within the matrix at 20 μm with no signs of N diffusion into Ti forming.

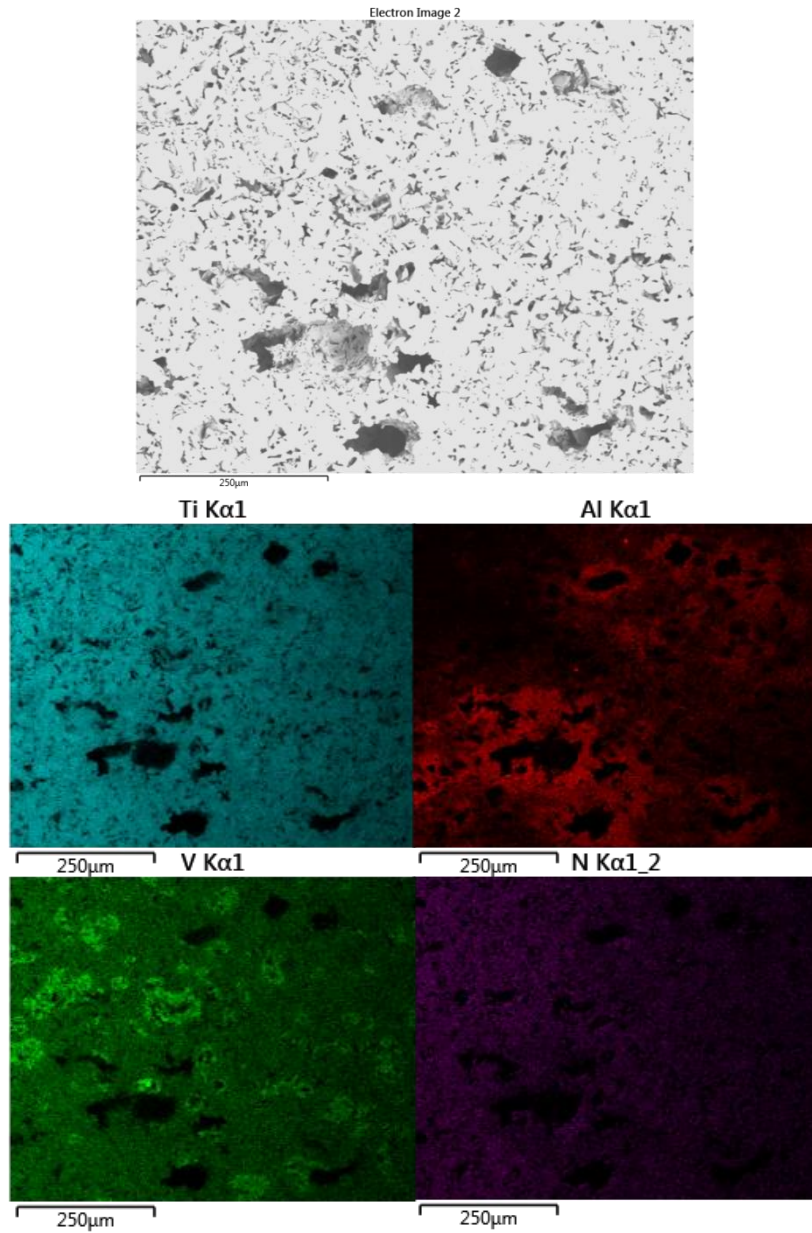


**Figure 48: EDS map BE 1100 °C sintered, 900 °C infiltration heat treatment, 1 hr dwell**

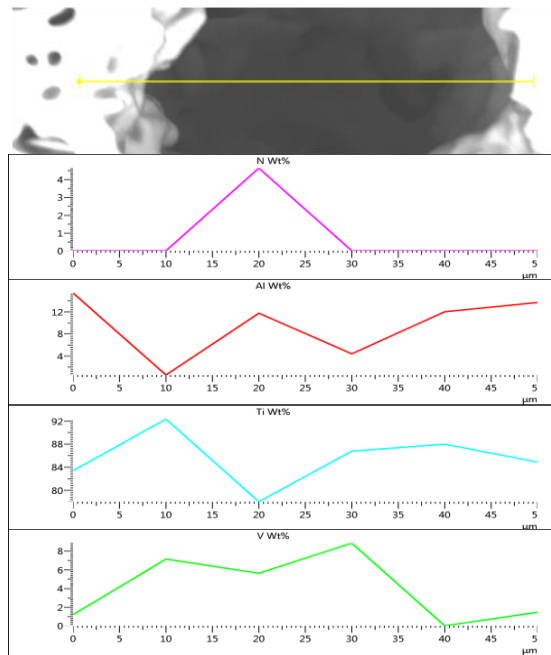


**Figure 49: EDS line distribution through pore of BE 1100 °C sintered, 900 °C infiltration heat treatment, 1 hr dwell**

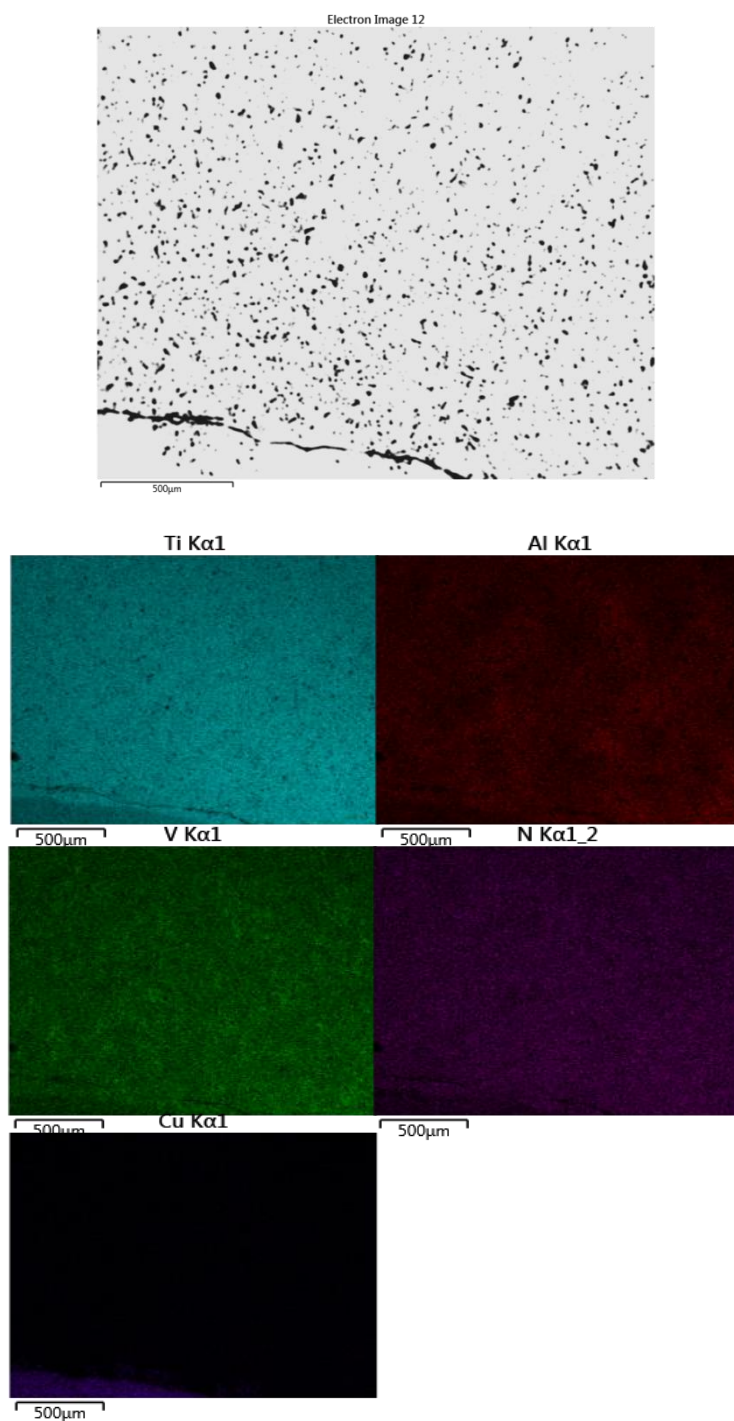
#### 4.3.8 1100 °C Sintered and 1150 °C Infiltrated Samples (BE and CPTi+MA, Cu Disk)

CPTi+MA and BE powder blends were vacuum sintered at 1100 °C for 2 hours and then furnace cooled, after which the infiltration attempt was performed at 1150 °C with 1 hour dwell period with a copper disk placed above the Ti-6Al-4V sintered sample. This was attempted to view the infiltration capability into the Ti-6Al-4V and to observe whether the Al was the issue or the Ti-6Al-4V sample, as Cu has been known to infiltrate into CPTi (Scholtz & Blaine, 2018).

##### 4.3.8.1 CPTi+MA sample

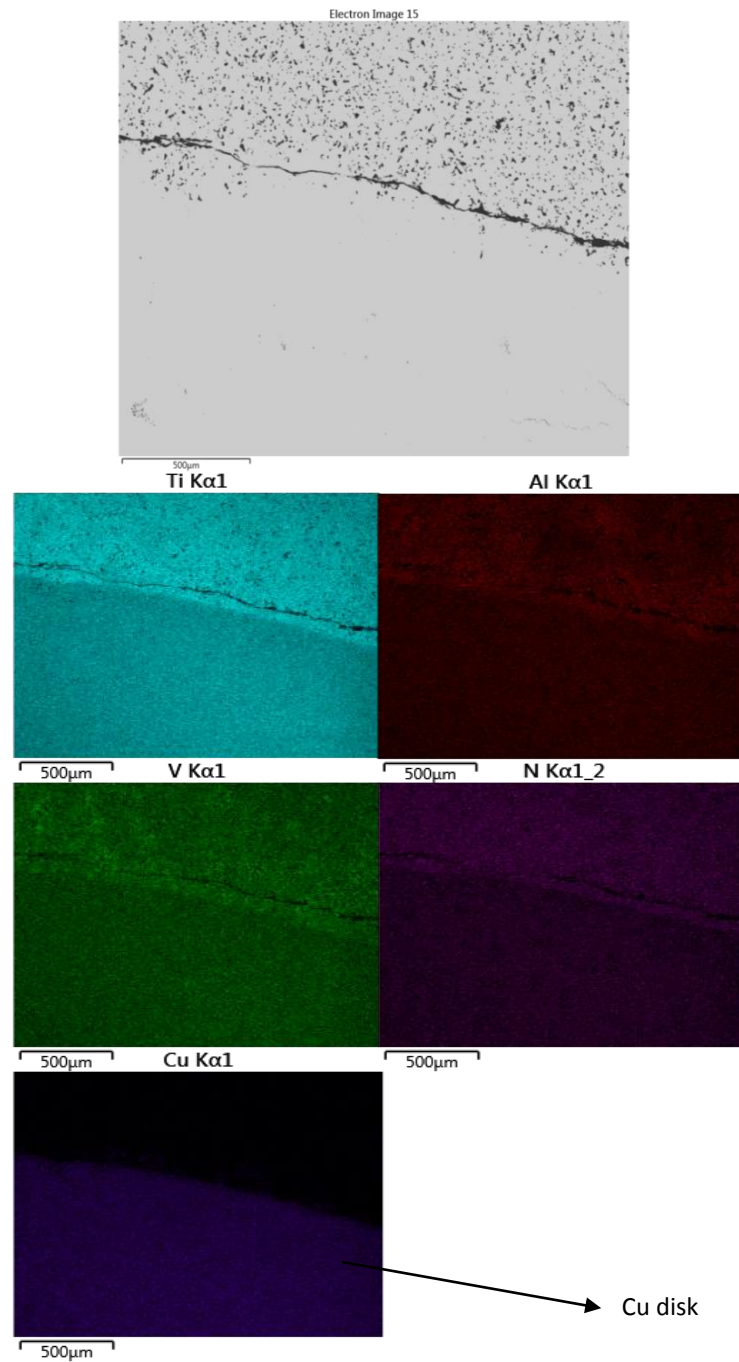
Figure 50 and Figure 51 shows the BS images and elemental distribution of Ti, Al, V, N and Cu of the CPTi+MA sample sintered to 92.1% hence. Figure 50 shows the typically homogeneous microstructure of the CPTi+MA sample and no evidence of Cu within this sample. No infiltration of the CPTi+MA sample blend was seen, yet this may be due to the high sintered density of the Ti-6Al-4V compact reaching 92.1%, bordering over the closed pore parameter (German.RM 2005). Figure 51 shows the Cu disk (placed on top yet viewed from the bottom in figure). It is evident that Ti, Al, V and N have diffused into the Cu disk, similarly to what is observed for the Cu disk in Figure 50.

Figure 52 shows the EDS line scan through a pore in the Ti-6Al-4V matrix. N is present throughout the matrix. It is seen that very little Cu is present within the matrix, which means small amounts did diffuse into the matrix but not enough for infiltration to be confirmed. The crack present may have been due to metallographic preparation or due to the separation of the Cu disk and the Ti-6Al-4V sample, as this crack was only apparent in the CPTi+MA sample where infiltration did not occur.



**Figure 50: EDS map CPTi+MA 1100 °C sintered, 1150 °C infiltration heat treatment, 1 hr dwell**





**Figure 51: EDS map CPTi+MA 1100 °C sintered with Cu disk, 1150 °C infiltration heat treatment, 1 hr dwell**

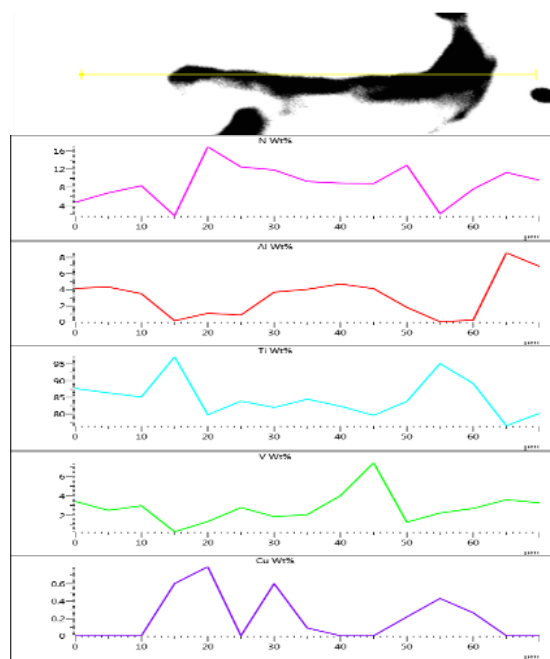


**Figure 52: EDS line distribution through pore of CPTi+MA 1100 °C sintered, 1150 °C infiltration heat treatment, 1 hr dwell**

#### 4.3.8.2 BE sample

Figure 53 has the BS images and elemental composition of Ti, Al, V N and Cu of the BE blend which has a corresponding sintered density of 75.6%. The Cu has infiltrated throughout the matrix, yet instead of filling the pores it has seemed to have alloyed with Al. Cu is highly soluble in Al as seen in literature with Zhu, M., *et al* (2002) after sintering at sintering temperatures above 550 °C. As can be see from Figure 53, high concentrations of Ti, V and N correlate to areas where no Al or Cu is found. It is suggested that when the Cu melts, it rapidly diffuses into the Ti-6Al-4V matrix, alloying with the Al and drawing any free Al out of the Ti-6Al-4V matrix leaving behind high concentrations of Ti and V. Figure 54 shows the distribution through a pore in the prior Ti-6Al-4V matrix. High concentration of N correspond to high concentration of Ti and V. Peaks of Al and Cu concentration correspond to low concentrations of Ti, V and N.

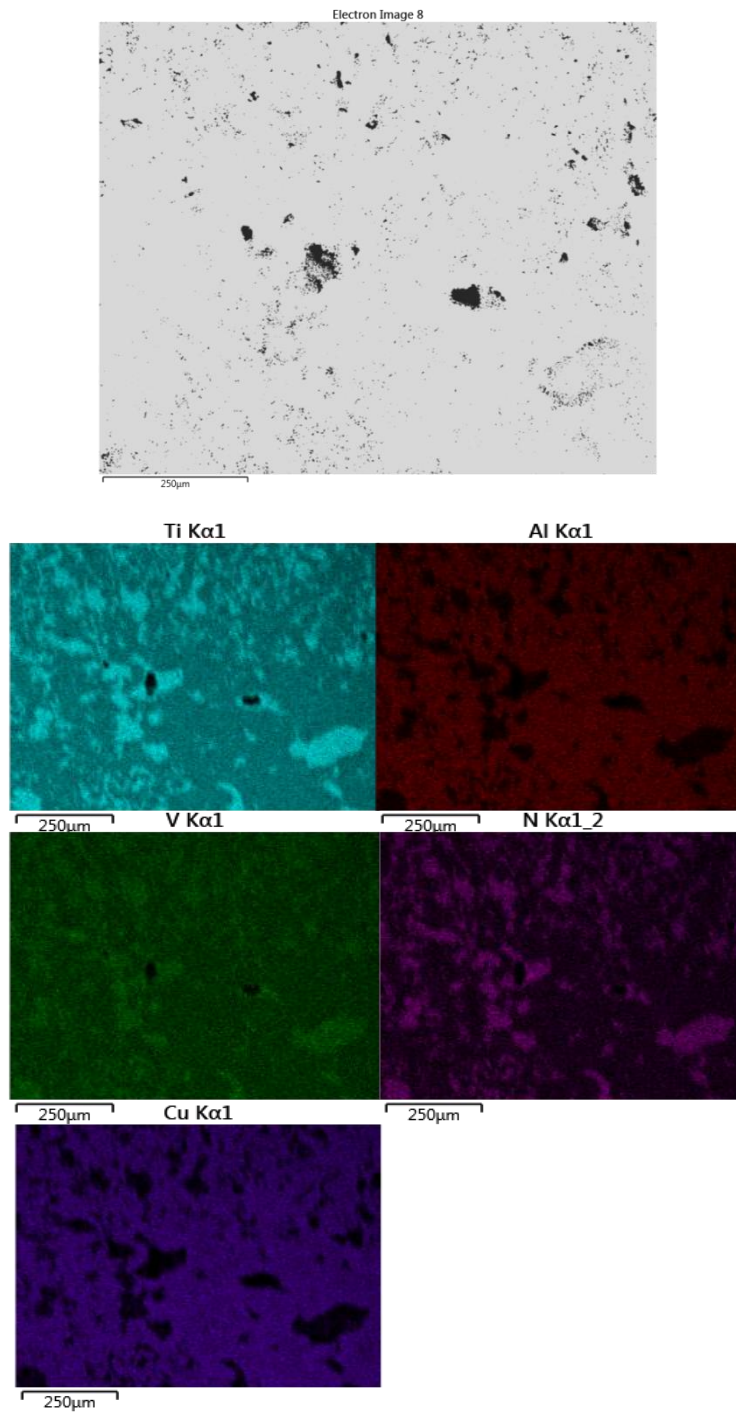


**Figure 53: EDS map BE 1100 °C sintered, 1150 °C infiltration heat treatment, 1 hr dwell**

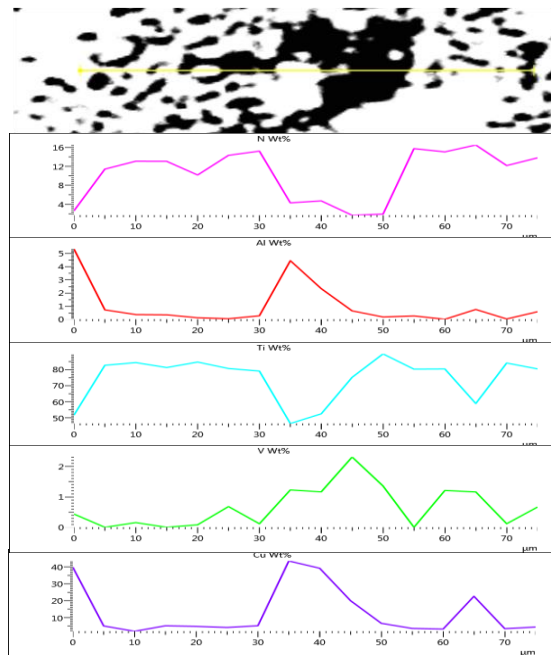


**Figure 54: EDS line distribution through pore of BE 1100 °C sintered, 1150 °C infiltration heat treatment, 1 hr dwell**

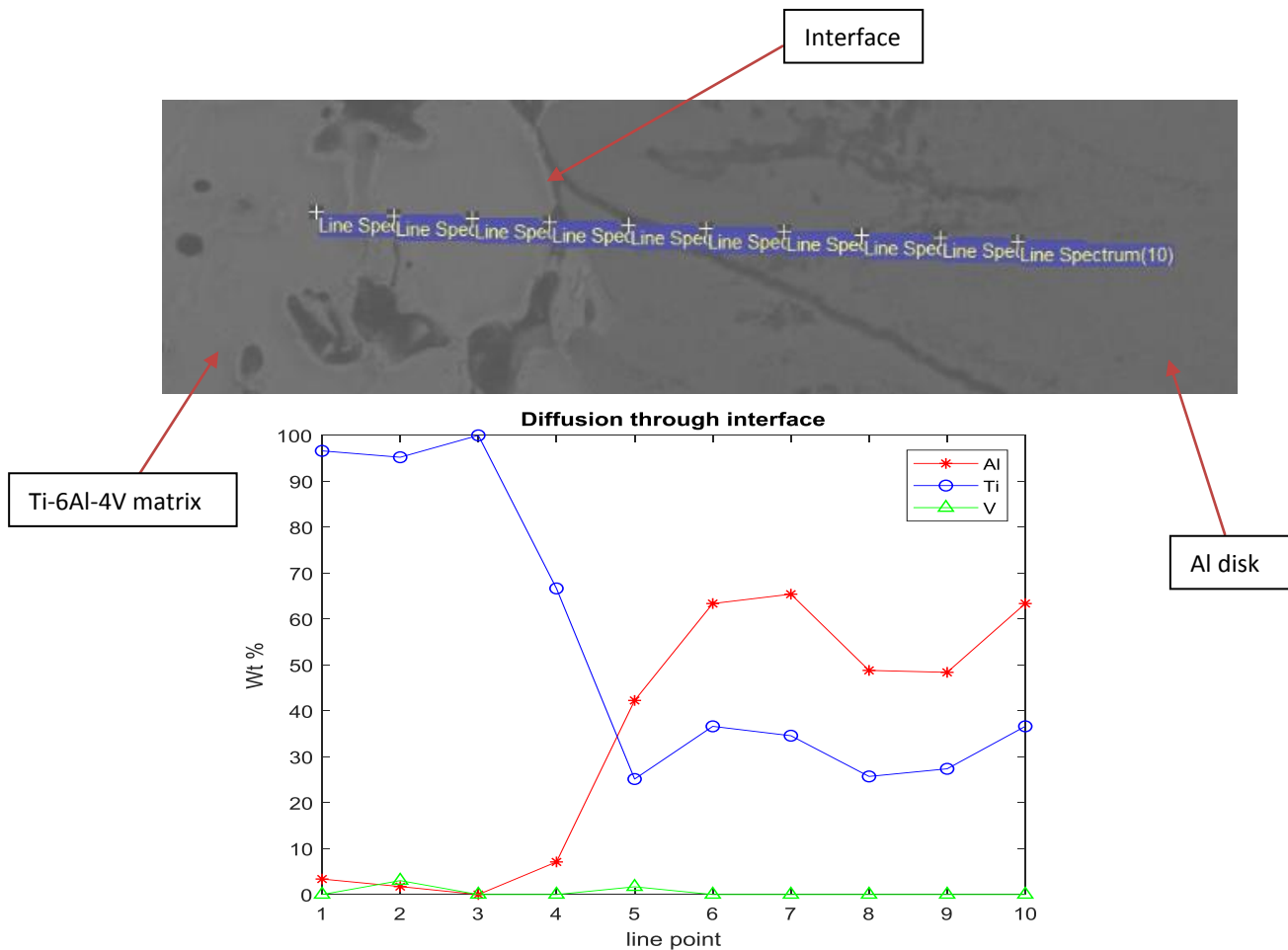
#### 4.3.9 Diffusion Graphs

Figure 71 to Figure 78 shows the diffusion graphs of samples sintered at 1100 °C and 1200 °C for both the CPTi+MA and BE samples found in Appendix C: Diffusion graphs. EDS analysis of the interface of the sintered Ti-6Al-4V samples and the Al disk was performed by means of a line scan that detected the elemental composition through the interface. Areas of interest included the amount of Ti and V that diffused into the Al disks.

BE samples sintered at 1200 °C were found to have areas within the Al disk that contained approximately 34 wt% Ti gradually decreasing further into the Al disk. By looking at the Ti-Al phase diagram at the infiltration temperature, (700 °C, 750 °C and 900°C), with the relevant wt%, we observe a possible formation of intermetallics with a melting temperature >1200 °C. MA samples sintered at 1200 °C seem to have the same experience with Ti diffusion into the Al disk with the composition increasing to approximately 36 wt%. In these cases we see marginal diffusion of V compared to Ti diffusion in the system.

Samples sintered at 1100 °C experience the same diffusion of Ti varying from 30-38 wt% of Ti in the Al disk which gives rise to the possible formation of TiAl<sub>3</sub> observed on the binary phase diagram. To definitively observe these intermetallics, the use of XRD would have to be performed, yet those experiments

were outside the scope of this investigation. With these samples sintered at 1100 °C we see the amount of V diffusion is almost negligible compared to the Ti diffusion into Al. Figure 55 shows a MA sample analysed through the interface showing the compositions of Ti, Al and V from within the Ti-6Al-4V matrix into the Al disk. The CPTi+MA sample sintered at 1100 °C showed an inhomogeneous distribution at the outer edge, with predominantly  $\alpha$ -phase present indicating the lack of V diffusion throughout the matrix especially at the edge of the samples, hence the low V content.



**Figure 55: Diffusion graph of MA sample after infiltration at 900 °C, 1 hr dwell, sintered at 1100 °C**

### 4.3.10 Micro Structures of Un-infiltrated Sintered Samples

Figure 56 to Figure 58 shows the etched, un-infiltrated samples sintered at 1100 °C and 1200 °C. These samples were etched to observe the different microstructures and grain boundaries.

#### 4.3.10.1 1100 °C Sintered Temperature

Figure 57 shows the CPTi+MA sample. As seen a dual phase  $\alpha+\beta$  microstructure is present within the system. What is interesting to note is the predominantly  $\alpha$ -phase present at the outer edge of the sample. This supports the previous results stating that V did not fully diffuse throughout the entire system, as Al is an  $\alpha$  stabilizer and V is a  $\beta$  stabilizer. In Figure 56 we see the BE etched sample. A predominantly  $\alpha$ -phase microstructure is present throughout the entire system, with  $\beta$ -phase only present around V particles. This is evident from EDS analysis as the V did not diffuse throughout the system as Al diffusion has hindered V diffusion, leaving high concentrations of V which then formed  $\beta$ -phase around those V particles.

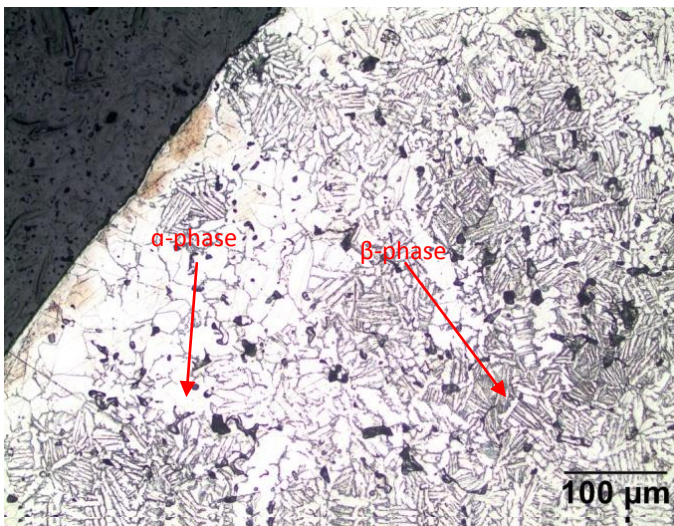


**Figure 57: Micro structure of CPTi+MA sample (1100 °C)**

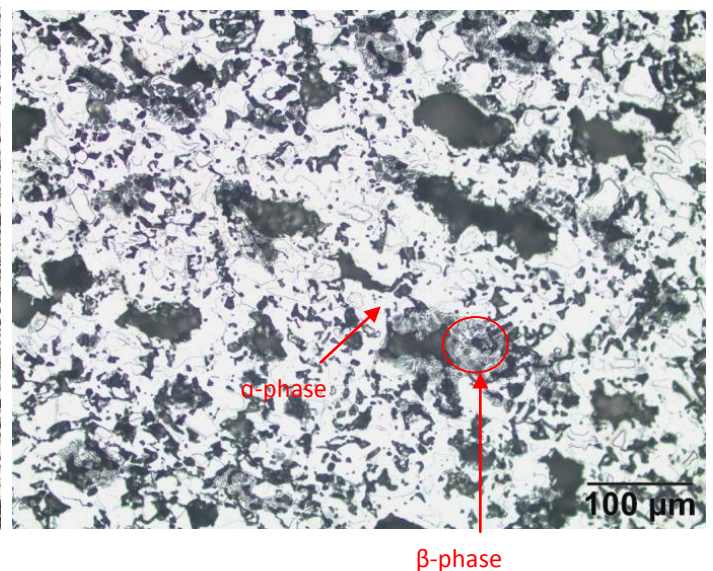


**Figure 56: Micro structure of BE sample (1100 °C)**

#### 4.3.10.2 1200 °C Sintered Temperature

Figure 58 shows the etched CPTi+MA sample. Observed is the dual phase  $\alpha+\beta$  microstructure present throughout the entire system, even at the outer edge unlike the previous sample sintered at 1100 °C. This shows that at a higher sintering

temperature, V diffuses throughout the system creating a more homogenous composition. Figure 62 shows the etched BE sample. Similar to the sample sintered at 1100 °C, we see a predominantly  $\alpha$ -phase microstructure with  $\beta$ -phase present only around V particles.

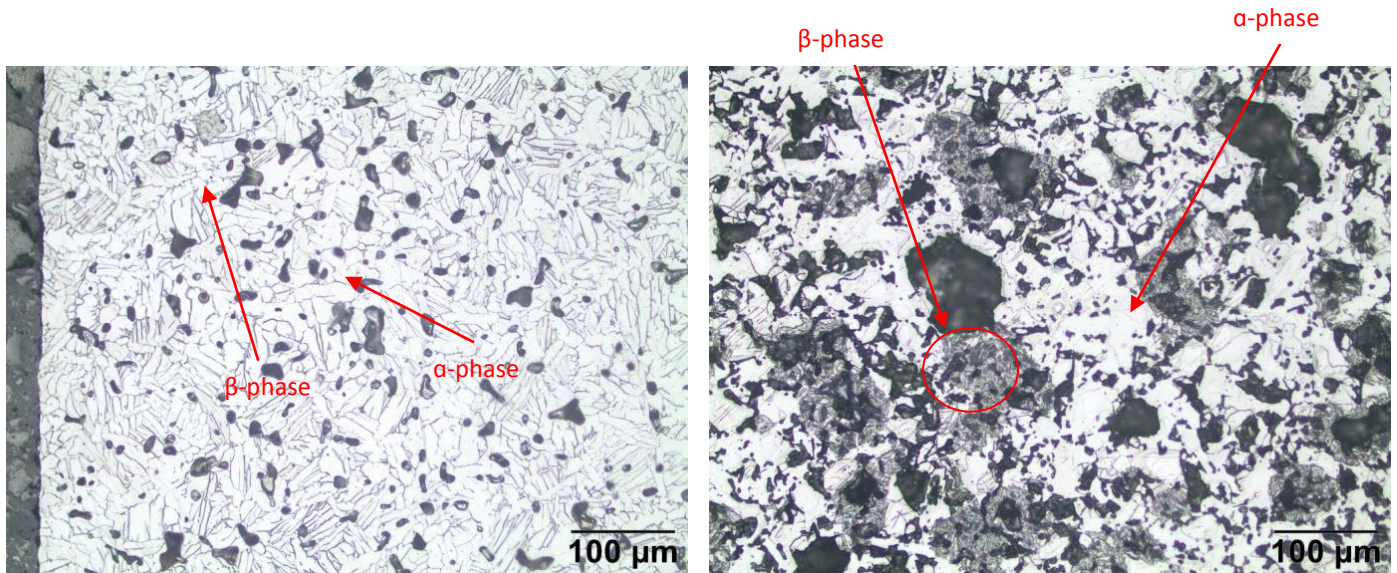


**Figure 59: Micro structure of CPTi+MA sample (1200 °C)**

**Figure 58: Micro structure of BE sample (1200 °C)**

#### 4.3.11 SEM Images

Figure 60 shows SEM images of the wrought Al disk before an infiltration attempt occurred (before melting) at different magnifications. The grooves present occurred from the cutting process of the Al disk and shows the surface structure before melting. Figure 61 shows an image of a compacted Al disk after the infiltration process. The image shows the surface that was in contact with the Ti-6Al-4V sample. The liquidlike structures and well as the irregular surfaces indicate that the sample has indeed melted, and it is assumed oxide layers have broken yet not completely. What is interesting to notice is the sphere like structure visible. This is an Al particle from the compaction process. This indicates, as the particle still contains the same shape, that the compact melted at the interface, yet that was extent of the melting that occurs. No melting occurred further within the Al compact.

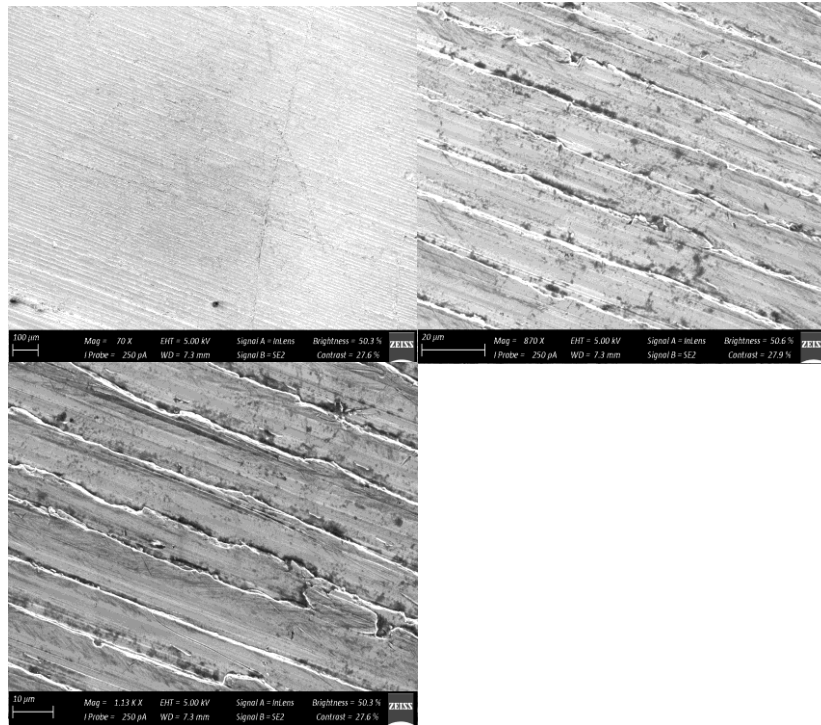


**Figure 60: SEM image wrought Al disk before infiltration**

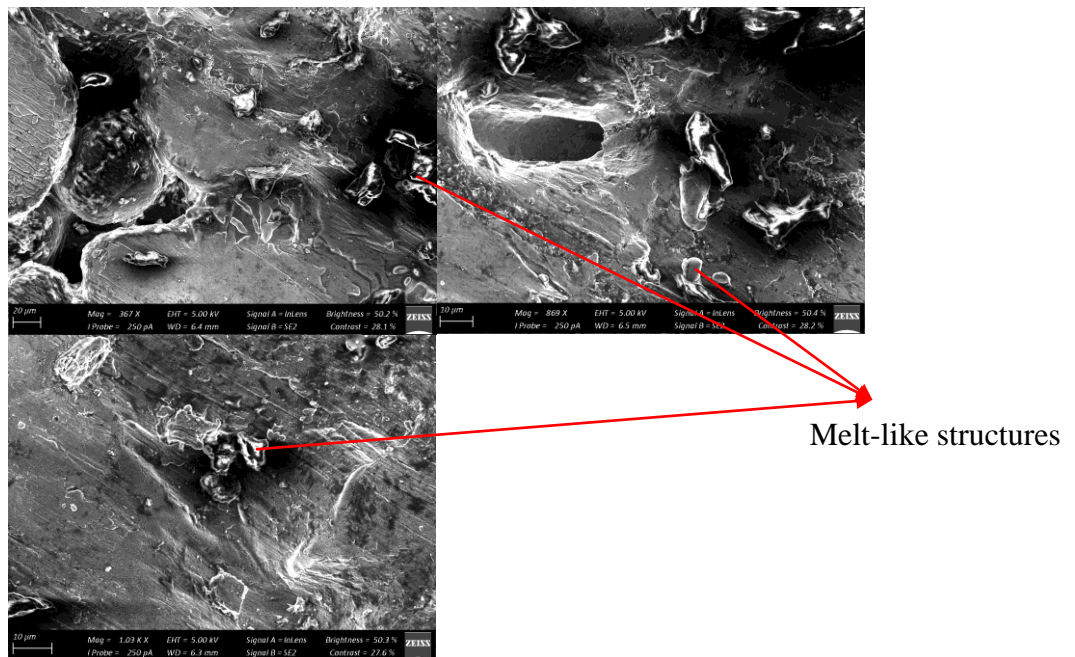


**Figure 61: SEM image Al powder compact after infiltration**



#### 4.3.12 Crack Propagations

From Bjerregaard, L et al (2002), we observe the possibility of crack formation due to the metallographic process coupled with a brittle structure and high forces. Although the possibility of crack formation due to compaction defects are present, there is evidence that points to the metallographic process as the cause for the present cracks due to high process forces. By observing the green densities after compaction, we determine that the green densities for the CPTi+MA and BE samples are fairly similar.

After the sintering and infiltration processes, the samples were cut, grinded and polished. The CPTi+MA samples and BE samples were first subjected to high forces during the preparation process of which cracks were very apparent only on the BE samples. The forces were reduced and it was observed that the BE or CPTi+MA samples did not show prominent crack formation compared to the high force prepared BE samples. This shows that if compaction defects were the underlying factor that contributed to the formation of the cracks present, the CPTi+MA samples would have also contained cracks within the sample.

Another factor that may have contributed to crack formation was the brittle nature of the BE samples compared to that of the CPTi+MA samples. It was seen after etching both samples that the BE samples contained a predominantly  $\alpha$ -phase microstructure due to the lack of diffusion of V throughout the system (as Al is an  $\alpha$ -phase stabilizer) and  $\alpha$ -phase is more brittle than  $\beta$ -phase. The CPTi+MA samples had a much more homogenous distribution than the BE samples, hence due to this brittle BE microstructure coupled with high forces, the formation of crack by metallographic preparation is a viable explanation.

## 5 Discussion of Results

The following results are presented for the CPTi+MA and BE samples with regards to Section 4 and Appendix A and Appendix B and Appendix C: Diffusion graphs.

**CPTi+MA samples:** Powder blends were pressed with relative green densities of approximately 75%. The sintered densities increased as expected from 75% to 85-92% sintered density. Appendix A shows the change in densities as well as the sintering parameters used for each sample. Most remained <92% sintered density as to allow for open pores for infiltration to occur. Upon micro-structural investigation of un-infiltrated sintered samples, the presence of  $\alpha+\beta$  microstructures were present as shown in Figure 62 and Figure 65 in Appendix B at 1100 °C and 1200 °C respectively. It was noted that in powder blends sintered at 1100 °C, upon the external edge of the sintered powder blend there is a lack of  $\beta$  microstructure. This suggests that V did not diffuse fully towards the external edges of the Ti-6Al-4V sample preventing  $\beta$  formation, as V is a  $\beta$  stabilizer. Powder blends sintered at 1200 °C shows complete solid state diffusion of the MA (Al-V) into Ti during analysis; however there are higher concentrations of V in prior MA particles leaving pockets of V within the matrix. This is due to the higher diffusion rate of Al in Ti compared to V in Ti. Al diffuses out of MA particles into the Ti particles leaving behind high V concentrations within the prior MA particle. From literature we see that as Al diffusing out of the MA, this diffusion hinders the diffusion of V into Ti (Lindwall.G *et al*, 2018:731). With samples sintered at 1200 °C, analysis indicates microstructures are completely homogenous, showing an even distribution of Ti, Al, and V throughout the matrix with  $\alpha+\beta$  microstructure present throughout the matrix.

The infiltration attempts of both PM Al powder compacts and wrought Al disks that were heated to temperatures between 700-900 °C and held for times between 0-60 min in a nitrogen atmosphere were performed and all attempts were unsuccessful. It was also observed with EDS analysis that Ti and V diffused from the Ti-6Al-4V sample into the Al disks of which the possibility of an intermetallic is formed which is supported by literature by (Xu, L., *et al* 2006) and (Xu,X., *et al* 2014) with Ti diffusing into Al. Pressing the samples into disks was performed in order to crack the aluminium oxide layer and provide direct contact of the Al powder samples, yet elimination of the oxide films was still yet to be determined. Due to this, slices of wrought Al disks were used. The result was that the wrought disks did melt somewhat, yet also did not infiltrate. The absence of infiltration could be explained by the contact angle between the Al disks and the Ti-6Al-4V samples. The hindered infiltration suggests that the contact angle may have been more or equal to 90° which leads to no wetting of the molten metal on the solid surface yet further research into this phenomenon needs to be investigated.

**Blended elemental samples:** Powder blends were pressed with relative green densities of 72-76%. The sintered densities were not as expected with negligible densification occurring leaving the sintered densities reasonably unchanged to the relative green densities. This is explained by the Al diffusing into the Ti and V, resulting in voids within the Ti-6Al-V blend which was confirmed with EDS analysis. Sample mass before and after sintering was measured and found to be constant, indicating no signs of omission of Al (no evaporation). In Appendix B we see the BE etched microstructure for samples sintered at 1100 °C and 1200 °C. As sintered densities remained fairly constant (no densification), a predominantly  $\alpha$ -microstructure was present throughout the entire Ti-6Al-4V matrix. It was noted that Al diffusion hinders diffusion of V from literature, hence  $\beta$ -microstructure was present surrounding V particles, yet as diffusion of V did not occur throughout, the  $\beta$ -microstructure was limited to those areas. Upon EDS analysis, large pores were visible within the sintered and sintered-infiltrated microstructure. It was also noted that very high Al concentrations were present in regions close to the pore structures. This suggests that the Al particles diffused into the Ti and V, leaving behind pores causing incomplete densification during sintering (Ivasishin.O *et al*, 2002:328). High concentrations of V were present in pocket-like structures. This suggests that V started to solid state diffuse into the matrix leaving behind small pores. As the sintering temperature was below the melting temperature of V, the V did not fully diffuse into the matrix. The diffusion of Al into the matrix has also hindered the diffusion of V thus causing large voids to remain explaining the lack of densification. Large cracks were observed on the sample surfaces due to metallographic preparation. Relatively high forces during this sample preparation may have caused these cracks to form. The brittle structure formed from the predominantly  $\alpha$ -phase Ti produced within the Ti-6Al-4V system also contributed to crack formation. This microstructure together with the high metallographic process was attributed to crack formation. Defects during the compaction process may have also been a contributing factor yet as described in section 4.3.12 the artefact for crack propagation points towards the brittle fracture and high preparation forces.

The infiltration attempts of both PM Al powder compacts and wrought Al disks that were heated to temperatures between 700-900 °C and held for times between 0-60 minutes in a nitrogen atmosphere were performed, and all attempts were unsuccessful. It was observed with EDS analysis in Figure 45 of the BE sample, that Ti and V diffused from the Ti-6Al-4V sintered sample into the Al disks. This raises the melting temperature of the Al disk by possibly creating an intermetallic, which could possibly be the reason for the absence of melting. Slices of wrought Al were used in place of the Al powder compacts to determine whether the compacts had a negative effect on the infiltration process, or whether Al disks in general is prohibited from infiltrating Ti-6Al-4V.

Nitrogen infiltrated the entire system, and as a result along with the infiltration temperatures, diffusion of N into Ti, Al and V seemed to have occurred. Suggested diffusion on the pore surfaces and within the matrix, may have

occurred as seen from the alignment of peaks on EDS line scans of Ti, Al, V and N. Optical microscopy analysis found after etching the formation of mainly  $\alpha$ -Ti within the system. Al is an alpha stabilizer hence the formation of  $\alpha$ -Ti. As V diffusion was hindered by Al, hardly any  $\beta$ -Ti has formed. Small amounts of  $\beta$ -Ti were seen to form around pore surfaces at V rich regions.

**Aluminium disks:** As previously stated, PM pressed and wrought Al disks were used for infiltration. Neither of the two infiltrated the Ti-6Al-4V samples. As mentioned in section 3.4, possible reasons for the absence of melting were described. Ti, V and N from the Ti-6Al-4V sample diffused into the Al disks. As Ti and V have higher melting temperatures than Al, this caused the melting temperature of the Al to increase, which lead to incomplete melting of Al during the infiltration process. By observing the wt% of Ti that diffused into the Al disks and the temperature the samples were heat treated at during infiltration, we could plot this on the Ti-Al phase diagram in Figure 5 and determine that the possibility of an inter-metallic was formed, which had a melting temperature  $>1000$  °C explaining why the disks did not fully melt. These wt% 's can be deduced from diffusion graphs present in Appendix C: Diffusion graphs. Another factor that contributed to the absence of melting was the passive aluminium oxide layer that formed on surfaces of the Al powder particles; hence the compaction process took place in hope to crack these oxide layers. As this did not change the outcome of the infiltrating experiments slices of wrought Al disks were used. The diffusion of Ti and V and N from the sintered samples possibly forming intermetallics into the Al disks still prevented full melting of the disks. In Figure 61 it is visible that the individual powder particle structures within the disks still whole, showing the absence of melting further into the sample. Contact angles need to be investigated to see whether the Al would infiltrate, yet from the results it seems as if the contact angle was a major factor as to the lack of infiltration.

SEM Imaging analysis before and after the infiltration attempt was performed on the interface between the Al disks and the Ti-6Al-4V surface. In Figure 60 before infiltration one could see the flat surface of the disks. After infiltration it is visible that the surface has melted somewhat by examining the uneven surface structures as well as pores on the surface. What should also be noted is that further within the disk, a fully formed Al powder particle still remained. This shows that at the contact region between the Ti-6Al-4V sample and the Al disk, melting occurred yet the heating process did not extend past the contact surface. In Appendix B optical microscopy figures are shown for the CPTi+MA and BE samples of the Al disks. In the compacted Al disks the individual particles are still present. This indicated incomplete melting of the Al disks towards the centre of the sample. On the surfaces we observe that melting has begun to occur to as there is a bigger porosity on the outer edges with some particles forming a liquid like structure.

As seen from the previous literature (Kim. S., et al, 2018 & Che. Z., et al, 2017), the formation of an intermetallic is not uncommon with molten Al and Ti. As in the Kim. S., et al (2018) investigation, it was found that the presence of V in the

Ti-matrix retards the diffusion of Al into Ti. In this study, large amounts of Ti diffuse into the Al disk during the infiltration heat treatment, whereas there is little increase in the Al concentration in the matrix. It is suggested that the presence both Al and V in the Ti-alloy sintered preform prevents the rapid diffusion of Al into the Ti-alloy matrix, and allows for Ti to diffuse into the Al disk. Furthermore, it is suggested that an aluminium-rich Al-Ti intermetallic forms in the disk by solid state diffusion, thereby raising the melting temperature of the Al disk and resulting in the incomplete melting of the Al disk during the infiltration heat treatment. In this investigation as we get high concentrations of Ti diffusing into the Al disk, as the Al disk partially melts at the interface, we have a reaction between the Ti and Al which can be attribute to the formation of an intermetallic.

**Cu Infiltration:** To determine whether the absence of infiltration was due to the Al on the Ti-6Al-4V sample, an experimental run of Cu disks replacing the Al disks was performed. It was observed that infiltration of Cu into the Ti-6Al-4V matrix only took place within the BE sample. The BE samples were found to have the Cu infiltrating deep within the matrix, yet suggests alloying with the Al as the coincidence of EDS line scan peaks lining up with the Al and Cu scans. Within the pores the diffusion of N with Ti and V seems to have occurred, with negligible Cu and Al found supporting the alloying theory. Within the CPTi+MA sample the Ti, Al, V and N have a homogenous distribution with no Cu infiltration in the system. It was seen that Ti, Al, N and V have diffused into the Cu disk. Again this may have increased the melting temperature preventing full melting of the Cu disks. The high sintered density of the Ti-6Al-4V sample reaching 92.1% exceeds the maximum sintered density allowed for infiltration, which could have contributed to the absence of infiltration of Cu for the CPTi+MA sample. Figure 70 in Appendix B: Microstructures shows the micro structure of the CPTi+MA and BE samples infiltrated with Cu. Here we see the colour change within the etched BE sample showing how far Cu has infiltrated within the sample.

## 6 Conclusion

Two Ti-6Al-4V PM powder blends consisting of a CPTi+MA blend and a BE blend, respectively, were pressed and compacted into right cylindrical samples with relative green densities of approximately 75%. These pressed samples were sintered under vacuum in a horizontal tube furnace at various temperatures (1100 °C and 1200 °C) and left to dwell at the peak temperatures for 2 hours, after which the sintered samples were left to furnace cool. The sintered densities of the CPTi+MA samples showed, on average a change in relative density from 74.5% to 90.2%, while the relative density of the BE samples remained essentially the same, changing from 73.6% to 74.9%. The mass of the Al disks was calculated by taking the residual porosity of the sintered Ti-6Al-4V compacts into account, and providing enough molten Al to infiltrate the pores exactly. The infiltration heat treatment took place in a horizontal tube furnace under a nitrogen atmosphere in the system. The Al powder compacted disks were placed above or below the

sintered Ti-6Al-4V samples and heat treated to various temperatures above the melting point of Al and held at various time periods to allow the Al to melt and infiltrate the sintered samples.

The Al powder compacts did not melt completely. An explanation could be the diffusion of Ti and V into the Al disks raising the melting temperature. This is due to an intermetallic being formed which had a melting temperature exceeding the heat treatment infiltration temperature. Another reason that could explain this from literature was the passive oxide layer that is found to be on the surface of all Al particles. The purpose of pressing the Al powder samples was performed in hope to crack this oxide layer. This passive oxide layer affected the melting temperature of the Al compacts and therefore only particles on the surface of the Al compacts or those that were in direct contact with the sintered Ti-6Al-4V sample begun to melt. Slices of wrought Al disks were also used. It was found that the wrought Al disks did not melt completely either, even at higher temperatures. Another possibility for the absence of melting may be due to the high contact angle between molten Al and Ti-6Al-4V. Further investigations into the contact angles need to be performed before a conclusion can be made.

Upon micro structural analysis, namely EDS mapping and optical microscopy (OM), the results confirmed that no infiltration has taken place within any of the samples. With EDS mapping we see the elemental compositions of each element of interest, namely Ti, Al, V and N. An important find was the diffusion of Ti, V and N into the Al disks. This gives reason to the absence of melting of the Al disks. As the melting temperature of Ti and V are much higher than that of Al, as they diffuse into the Al disks the melting temperature of the Al disks tend to rise above the general melting temperature of Al. Other findings included the homogenous composition of the sintered samples. With the CPTi+MA samples, it is observed that samples sintered at 1100 °C gave a fairly homogenous composition, yet there were high concentrations of V within the matrix. This is due to the Al melting out of MA particles and diffusing into the matrix leaving high V concentrations in prior MA particles. Upon OM analysis samples were etched and  $\alpha+\beta$  microstructures were found throughout the sample. It was noted at the sintered sample edge; predominantly  $\alpha$ -microstructure is found suggesting the lack of V diffusing throughout the system. Samples sintered at 1200 °C showed a completely homogeneous composition throughout. OM analysis showed complete  $\alpha+\beta$  microstructures throughout the sample, even at the samples' edges. The BE sintered samples had vastly different results with regards to microstructure. Samples sintered at both 1100 °C and 1200 °C both showed negligible densification. EDS mapping revealed large pore present within the system with high Al concentration outside these pores. This suggests the Al particles rapidly diffused into the system leaving behind voids. High concentrations of V are seen within these systems. From literature it is noted that the diffusion of Al into a Ti-Al-V system decreases the diffusion gradient of V, which implies the diffusion of V is hindered by the diffusion of Al. Large cracks were present within in the sample due to metallographic preparation. OM results shows for both sintered

temperatures the predominantly  $\alpha$ -microstructure present within the system. As mentioned earlier, the lack of V diffusion within the system then caused the reduction  $\beta$ -microstructure present. It is seen at areas of V particles as solid state diffusion begun to occur, small areas of  $\alpha+\beta$  microstructures are present, yet only at these areas. Due to the N source, results for both CPTi+MA and BE blends suggest the diffusion of N with Al, Ti and V upon pore surfaces. This is due to the coincidence of high N concentrations lining up with Ti, Al and V, respectively, upon line scans on the pore surfaces.

Cu disks that are typically used for infiltration for ferrous PM samples were evaluated. Cu disks were used instead of the Al disks to see if infiltration could occur. It was found after heat treatment processes that Cu did infiltrate the BE sintered sample, yet not the CPTi+MA sintered sample. This may be due to the CPTi+MA sintered sample having a sintered density of above 92%, closing off the pore channels for infiltration. It was observed that the Ti, V, Al and N did diffuse into the Cu disks, again raising the melting temperature prevent full melting of the Cu disks. With the BE sample, it seems the Cu alloyed with the Al within the matrix, as the concentrations seems to align on the EDS line scans. The pores then were not filled with the Cu, but rather the Ti and V and N, from which line scans, suggest the diffusion of N with Ti, and V resided within these pores.

This investigation concludes from the mentioned procedures that compacted and wrought Al disks do not infiltrate into sintered PM Ti-6Al-4V compacts. Further investigations into the contact angles need to be performed to determine whether infiltration can physically occur and investigations into other methods which may aid the infiltration process.

## 7 References

Anir, A., Atiq, S., Ibrahim, A., Qamar, A., Habiba, U., Khalil, N., 2017, Modification of the Mechanical Properties of Ti-Al-V Alloys with Variation of Aluminum, Proceedings of the Pakistan Academy of Sciences: A. Physical and Computational Sciences 54 (1): 95-108

Alcock, J., Stephenson, D., (1996), Materials World, [Online]. Available at: <https://www.azom.com/article.aspx?ArticleID=1080>, [Accessed on 22 March 2019]

ASM Aerospace Specification Metals Inc., [S.a]. [Online]. Available at: <http://asm.matweb.com/search/SpecificMaterial.asp?bassnum=mtp641>. [Accessed 22 September 2017]

ASTM B988-13. (2013) Standard Specification for Powder Metallurgy (PM) Titanium and Titanium Alloy Structural Components, ASTM International, West Conshohocken, PA, [www.astm.org](http://www.astm.org)

AZO Materials, 2002, Titanium-Applications, [S.a]. [Online]. Available at: <https://www.azom.com/article.aspx?ArticleID=1297>. [Accessed 11 October 2017]

Bao, S., Tang, K., Tangstad, M., Kvithyld, A., (2011), Wettability of Aluminum on Alumina, Metallurgical and Materials Transactions B, Volume 42, Issue 6, p 1358–1366

Bernier, F., Beaulieu, P., Bailon, J.P., L'Esperance, G., 2011, Powder Metallurgy Vol 54 Issue 3, p. 314-319

Bjerregaard, L., Geels, K., Ottesen, B., Ruckert, M., 2002, Metalog Guide, Struers A/S, Denmark, pp. 81-82

Bolzoni, L., Esteban, P.G., Ruiz-Navas, E.M., Gordo, E., 2011, Influence of powder characteristics on sintering behaviour and properties of PM Ti alloys produced from prealloyed powder and master alloy, Powder Meta. 54(4), p. 543-550

Bosman, H.L., (2016), Influence of powder particle size distribution on press-and-sinter titanium and Ti-6Al-4V preforms, (Masters thesis) SUNScholar <http://hdl.handle.net/10019.1/98709>, Stellenbosch, p.44

Cao, F., Chandran, K.S.R., Kumar, P., 2017, New approach to achieve high strength powder metallurgy Ti-6Al-4V alloy through accelerated sintering at  $\beta$ -transus temperature and hydrogenation-dehydrogenation treatment, Scripta Materialia 130, p. 22–26



Che, Z., Wang, Q., Wang, L., Li, J., Zhang, H., Zhang, Y., Wang, X., Wang, J., Kim, M.J., 2017, *Composites Part B* 113

Chunxiang, C., BaoMin, H., Lichen, Z., Shuangjin, L., 2011, Titanium alloy production technology, market prospects and industry development. *Materials & Design - MATER DESIGN*. 32. 1684-1691. 10.1016/j.matdes.2010.09.011.

Clinning, N., 2012, *Thermomechanical Processing of Blended Elemental Powder Ti-6Al-4V Alloy*, (Master Thesis), University of Cape Town, p. 70

Continental Steel & Tube Company, *Titanium Applications*, [S.a]. [Online]. Available at: <https://continentalsteel.com/titanium/applications/>. [Accessed 11 October 2017]

Coromant, S., (2004), *Application Guide - Titanium Machining*. Sweden

Das, J., Chakraborty, A., Bagchi, T.P., Sarma, B., 2008, Improvement of machinability of tungsten by copper infiltration technique, *International Journal of Refractory Metals and Hard Materials*, Volume 26, Issue 6, Pages 530-539, ISSN 0263-4368, <https://doi.org/10.1016/j.ijrmhm.2007.12.005>.

Dussan, E.B., (1979), On the spreading of liquids on solid surfaces: static and dynamic contact lines, *Annual Review of Fluid Mechanics*, p. 371-400.

Eylon, D., Froes, F. H., and Abkowitz, S., (1998), *Titanium Powder Metallurgy Alloys and Composites*, ASM Handbook Volume 07: Powder Metal Technologies and Applications, p. 874-883

Froes, F.H., 2013, *Powder Metallurgy of titanium alloys*, Woodhead Publishing, Knovel, USA, doi: 10.1533/9780857098900.2.202, p. 202

Froes, F.H., (2015), *Titanium Physical Metallurgy, Processing and Applications*, Ohio, United States of America, ASM International, pp. 353-354

Froes, F.H., Ashraf, M., Derek, F., (2007), Cost Affordable Titanium: The component fabrication perspective, *Journal of the Minerals Metals and Materials Society*, Vol. 59(6), p. 28-31.

German, R.M., (2005), *Powder Metallurgy & Particulate Materials Processing*, Metal Powders Industries Federation, New Jersey, p.63, 83, 229

Goso, X., Kale, A., (2010), Production of Titanium Metal Powder by the HDH Process, *Journal of the Southern African Institute of Mining and Metallurgy*, Vol. 111, p. 292-294.

Groover, M.P., (2011), Professor. In: *Principles of Modern Manufacturing*. s.l.:John Wiley & Sons, pp. 126-128, 335-336.

Groover, M.P., (2011), Principles of Modern Manufacturing, John Wiley & Sons, Asia, pp. 335-336, 343-352

Ivasishin, O.M., Savvakina, D.G., Froes, F., Mokoson, V.C., Bondareva, K.A., (2002), Synthesis of Alloy Ti – 6Al – 4V With Low Residual Porosity by a Powder Metallurgy Method, Powder Metals and Metal Ceramics, Vol 41, p. 382-383

Joubert, H.J., (2008), Investigation of lubrication strategies in Ti6Al4V milling operations, (Master's thesis), SUNScholar <http://scholar.sun.ac.za/handle/10019.1/1936>, Stellenbosch, p. 7-11.

Joong, S., Kang, L., (2007), Sintering Densification, Grain Growth, and Microstructure, Elsevier, p.1-6

Kenny, D.J., Wilhelm, H.A., Carlson, O.N., (1953), Aluminium-vanadium system, AEC Oak Ridge

Khandekar, S., Panigrahi, P.K., Lefevre, F., Bonjour, J., (2010), Local Hydrodynamics of Flow in a Pulsating Heat Pipe: A Review, Frontiers in Heat Pipes, Vol.1

Kim, S., Jung, H., Rim, H.J., Lee, H., Lee, W., 2018, Fabrication of reinforced  $\alpha+\beta$  titanium alloys by infiltration of Al into porous Ti-V compacts, Journal of Alloys and Compounds 768, p. 775-781

Kim, S., Kim, G., Lee, W., Lee, H., Jeung, W., 2017, A novel method to fabricate reinforced Ti composites by infiltration of Al (Mg) into porous titanium, Journal of Alloys and Compounds 715, p. 404-412, <http://dx.doi.org/10.1016/j.jallcom.2017.05.014> 0925-8388

Klar, E.S., Prasan K., (2007), Powder Metallurgy Stainless Steels - Processing, Microstructures, and Properties. ASM International.

Kobelco, Characteristics of titanium, [S.a.]. [Online] Available: <http://www.kobelco.co.jp/english/titan/characteristic/index.html> [accessed on 15 January 2019]

Lenel, F.V., (1980). Powder Metallurgy, Princeton, NJ: Metal Powder Industries Federation.

Lindahl, B., Liu, X.L., Liu, Z., Selleby, M., A thermodynamic re-assessment of Al–V toward an assessment of the ternary Al–Ti–V system, 2015, Calphad, Volume 51, p. 75-88, ISSN 0364-5916, <https://doi.org/10.1016/j.calphad.2015.07.002>.

Lindwall, G., Moon, K.W., Chen, Z., Mengason, M., Williams, ME., Gorham, JE., Zhao, JC., Campbell, CE., (2018), Diffusion in the Ti-Al-V System, J. Phase Equilib. Diffus., Vol 39 p. 731-764

Lohrey, M., Fuessel, U., Tuerpe, M., 2015, Behaviour of the aluminium oxide layer during heat treatment and the resulting effects on brazeability, Weld World 59, p. 225–237, <https://doi-org.ez.sun.ac.za/10.1007/s40194-014-0198-8>

Lorenz, A.M. Sachs, E.M. Allen, S.M. Cima, M.J. S.a, Homogenous metal parts by infiltration, Cambridge, p.70

Liu, J., Qin, Y., Zheng, J., Chen, C., Xiao, P., 2018, New approach to achieve high strength powder metallurgy Ti-6Al-4V alloy through a simplified hydrogenationdehydrogenation treatment, Journal of Alloys and Compounds 763, p.111-119.

Liu, S., Shin, Y.C., 2019, Additive manufacturing of Ti6Al4V alloy: A review, Materials & Design, Volume 164, 107552, ISSN 0264-1275, <https://doi.org/10.1016/j.matdes.2018.107552>.

Materials Evaluation and Engineering Inc., (2014), Energy Dispersive X-Ray Spectroscopy, [Online]. Available at: <http://www.mee-inc.com/hamm/energy-dispersive-x-ray-spectroscopyeds/>. [Accessed 17 October 2017]

Okamoto, H., 2012, Al-V (Aluminum-Vanadium), J. Phase Equilib. Diffus. 33, 491, <https://doi.org/10.1007/s11669-012-0090-4>

Ostwald, P.F., Muñoz, J., (1997). Manufacturing Processes and Systems (9th Edition) - 20.6.1 Important Characteristics of Metal Powders. John Wiley & Sons.

Pierson, H.O., (1996). Handbook of Refractory Carbides and Nitrides - 9.4 Summary of Fabrication Processes, William Andrew Publishing, p. 200-202, 238-239

Qangule, L., 2015, The Influence of Process Route on Mechanical Property Development in Sintered Commercially Pure and Blended Elemental Titanium, (Master Thesis) University of Cape Town, p. 78

Qian, M., Schaffer, G., (2010), Sintering of aluminium and its alloys, Sintering of Advanced Materials, Metals and Surface Engineering, p.289-323.

Raghaven, V., 2012, Al-Ti-V(Aluminum-Titanium-Vanadium), Journal of Phase Equilibria and Diffusion Vol. 33 No. 2, p. 151, <https://doi.org/10.1007/s11669-012-0017-0>

Ramakrishnan, P., (1983), History of Powder Metallurgy. Indian Journal of History of Science, 1(18), pp. 109-114.

Robertson, I.M., Schaffer, G.B., Review of densification of titanium based powder systems in press and sinter processing, 2010, Powder Metallurgy, vol. 52 No. 2, p. 146-162

Saunders, N., 1990, The Ti-V System, Thermotech, Available at: <http://steel.kisti.re.kr/hm/Ti-V.htm>, [Accessed 20 February 2019]

Schaffer, G.B., Hall, B.J., Bonner, S.J., Huo, S.H., Sercombe, T.B., (2006), The effect of the atmosphere and the role of pore filling on the sintering of aluminium, *Acta Materialia*, Vol 54: 1, pp.131-138

Schaschke, C., (2014). Dictionary of Chemical Engineering. (pp. 346). Oxford University Press. Online. Available at: <https://app.knovel.com/hotlink/toc/id:kpDCE00021/dictionary-chemical-engineering/dictionary-chemical-engineering> [07 June 2018]

Scholtz, A.P., (2018), A study of copper infiltration for conventional ferrous powder metallurgy, (Masters thesis), SunScholar, <https://scholar.sun.ac.za/handle/10019.1/105089?show=full>, Stellenbosch

Schuster, J.C., Palm, M., 2006, Reassessment of the binary Aluminum-Titanium phase diagram. *JPED* 27, 255–277, <https://doi.org/10.1361/154770306X109809>

Shewman, P.G., [S.a], “metallurgy”, Available at: <https://academic-eb-com.ez.sun.ac.za/levels/collegiate/article/metallurgy/110658>, [Accessed 18 January 2019]

Skulev, H., Drenchev, B., Mechkarova, T., Drenchev, L., 2014, Kinetics of Surface Layers Growth in Gas Nitriding Ti-6Al-4V by Indirect Plasma Torch, *Journal of Material Science and Technology*. 22. 57-75.

Smith, S.M., Taft, B.S., Moulton, J., (2014), Contact Angle Measurements for Advanced Thermal Management Technologies, *Frontiers in Heat and Mass Transfer*, Vol 5:2

Suresh, S., Mortensen, A., Needleman, A., 1993. Fundamentals of Metal-Matrix Composites - 1.1.1 Description. (pp. 3-5). Elsevier. Retrieved from <https://app.knovel.com/hotlink/pdf/id:kt00579YX1/fundamentals-metal-matrix/infiltration-description>

Tadmor, R., Yadav, P.S., (2008), As-placed contact angles for sessile drops, *Journal of Colloid and Interface Science*, 317, pp. 241-246.

Terblanche, H.D., 2014, Design and Build of an Argon Sintering Furnace for Titanium, (Final year dissertation) Stellenbosch University, p. 14

Titanium-Aluminium (Ti-Al) Phase Diagrams, (2011), [Online]. Available at: <http://www.calphad.com/titanium-aluminum.html>, [Accessed 19 September 2017]

Vladmir, A.J., Vladimir, D., Moxson, V., 2008, Powder metallurgy processes for producing titanium alloy products from hydrogenated titanium powder. TMS Annual Meeting. 1. 363-368.

Wang, H., Wang, S., Gao, P., Jiang, T., Li, C., (2016), Microstructure and mechanical properties of a novel near- $\alpha$  titanium alloy Ti6.0Al4.5Cr1.5Mn, *Materials Science and Engineering: A* 672 p. 170-174

Xu, L., Cui, Y.Y., Hao, Y.L., Yang, R., 2006, Growth of intermetallic layer in multi-laminated Ti/Al diffusion couples, *Mat. Sci. and Engineering A* 345-436, p. 638-637

Xu, X., Lui, G.N., Nash, P., 2014. Sintering mechanisms of blended Ti6Al4V powder from diffusion path analysis. *Journal of Materials Science* , Vol. 49, pp. 994-1008.

Ye, B., Matsen, M.R., Dunand, D.C., 2011, Blended elemental powder densification of Ti-6Al-4V by hot pressing, *J. Mater. Res*, Vol 26, No. 8, p. 965

Yu, P., Schaffer, G.B., (2009), Microstructural evolution during pressureless infiltration of aluminium alloy parts fabricated by selective laser sintering, *Acta Materialia*. 57. 1, pp.163-170

Zhu, M., Zeng, M.Q., Gao, Y., Ouyang, L.Z., Li, B.L., Microstructure and wear properties of Al-Pb-Cu alloys prepared by mechanical alloying, *Wear*, Volume 253, Issues 7-8, p. 832-838, ISSN 0043-1648, [https://doi.org/10.1016/S0043-1648\(02\)00165-5](https://doi.org/10.1016/S0043-1648(02)00165-5).

## Appendix A: Sintering and Infiltration Parameters and Results

Table 7: Vacuum Sintered results and infiltration parameters

	Sample	Green density %	Sintering parameters	Sintered density %	Mass of Al (g)	Infiltration Temp (°C)	Time (hr)	Aluminium
<b>CPTi+MA</b>	1	73.3	1100 °C for 2h	85.4	0.26	0	0	N/A
	2	71.9		89.5	0.18	700	0	Compact
	3	74.1		90.3	0.16	750	1	Compact
	4	75.2	1200 °C for 2h	92.2	0.13	0	0	N/A
	5	76.1		82.3	0.32	750	1	Wrought
	6	75.5		89.9	0.16	900	1	Wrought
	7	74.2	1100 °C for 2h	91.9	0.13	900	1	Wrought (bottom)
	8	75.6		90.6	0.15	900	1	Compact
	9	75.6		92.1	0.12	1150	1	Cu disk
<b>BE</b>	1	71.9	1100 °C for 2h	73.0	0.45	0	0	Compact
	2	74.0		75.0	0.42	700	0	Compact
	3	73.1		73.1	0.46	750	1	Compact
	4	71.5	1200 °C for 2h	74.4	0.42	0	0	Compact
	5	74.0		74.2	0.43	750	1	Wrought
	6	72.9		74.1	0.43	900	1	Wrought
	7	74.6	1100 °C for 2h	73.9	0.44	900	1	Wrought (bottom)
	8	74.6		74.8	0.42	900	1	Compact
	9	74.0		75.6	0.40	1150	1	Cu disk

## Appendix B: Microstructures

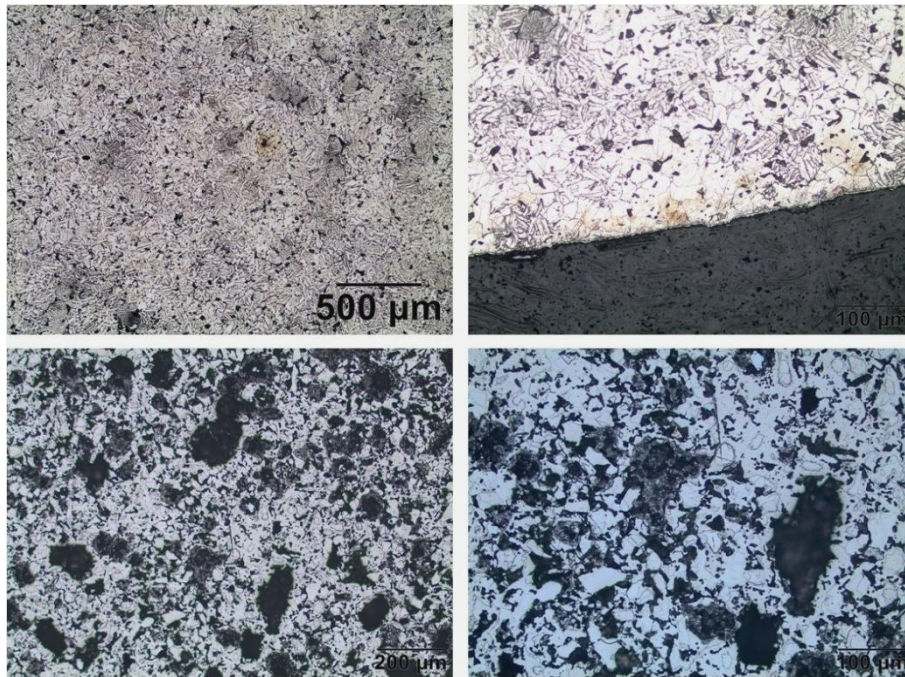


**Figure 62: No infiltration disk (1100 °C sintered): Etched CPTi+MA images (top left and top right) and etched BE images (bottom left) with etched Al disk image (bottom right)**

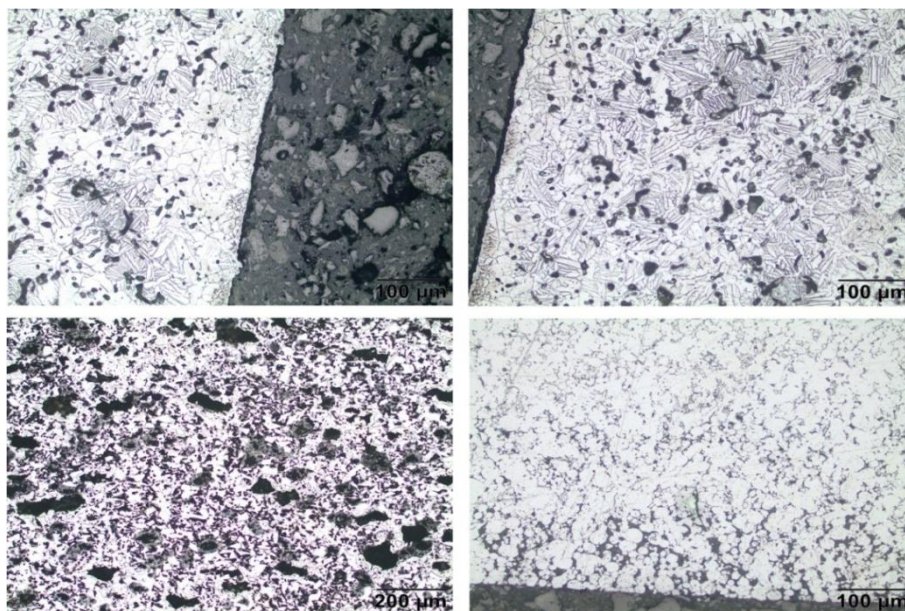


**Figure 63: Al powder compact (1100 °C sintered): Etched CPTi+MA images (top left and top right) and etched BE image (bottom left) with etched Al disk image (bottom right)**

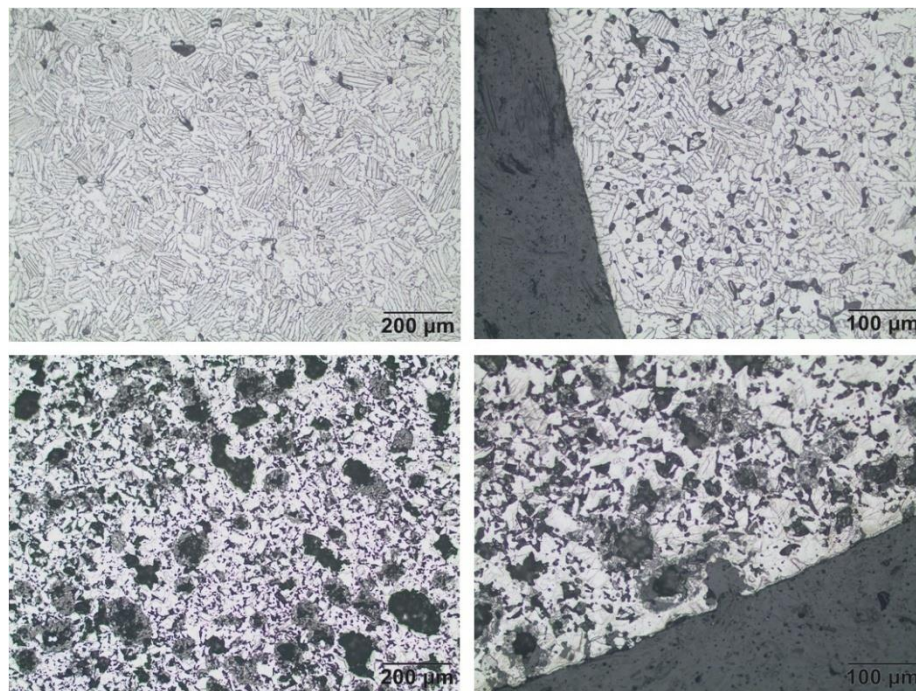


**Figure 64: Al powder compact (1100 °C sintered): CPTi+MA etched image (top left) and Al disk (top right). BE etched image (bottom left) and Al disk (bottom right)**

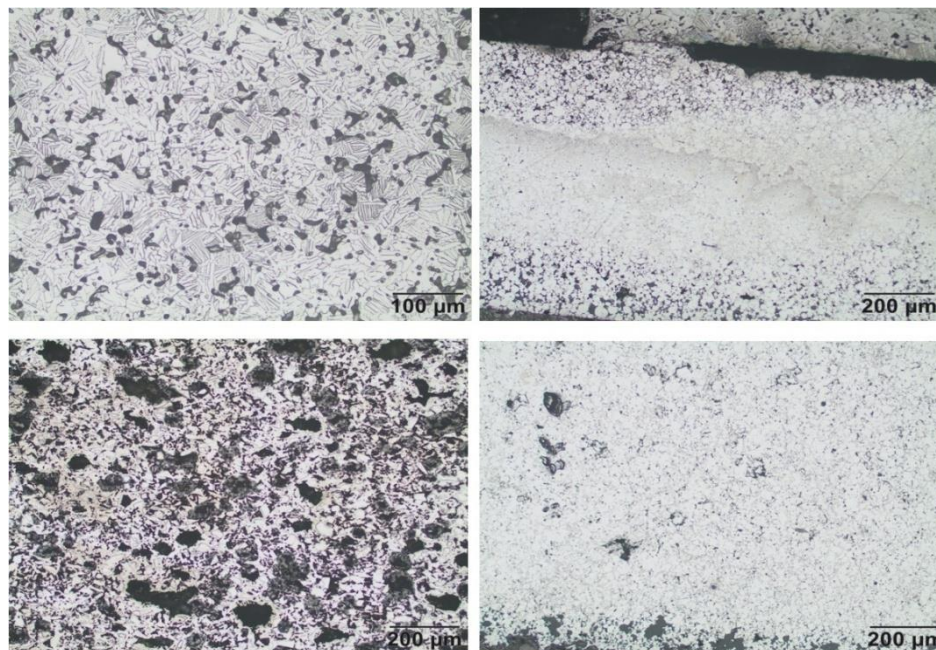


**Figure 65: No infiltration disk (1200 °C sintered): CPTi+MA etched image (top left and right) and BE etched images (bottom left and right)**



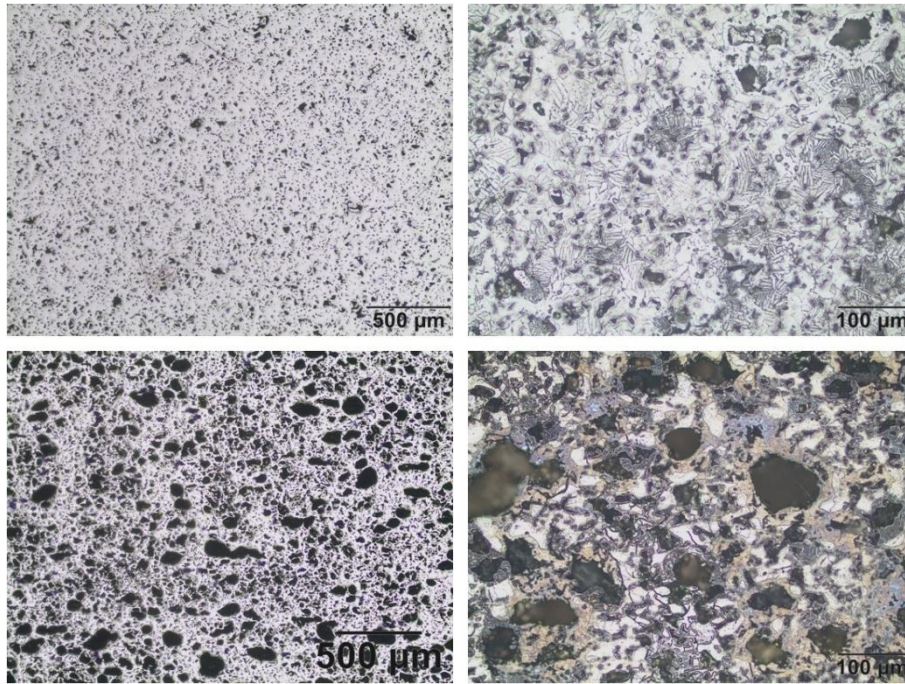


**Figure 66: Wrought Al disk (1200 °C sintered): CPTi+MA image (top left) and etch image (top right) and BE image (bottom left) and etched image (bottom right)**

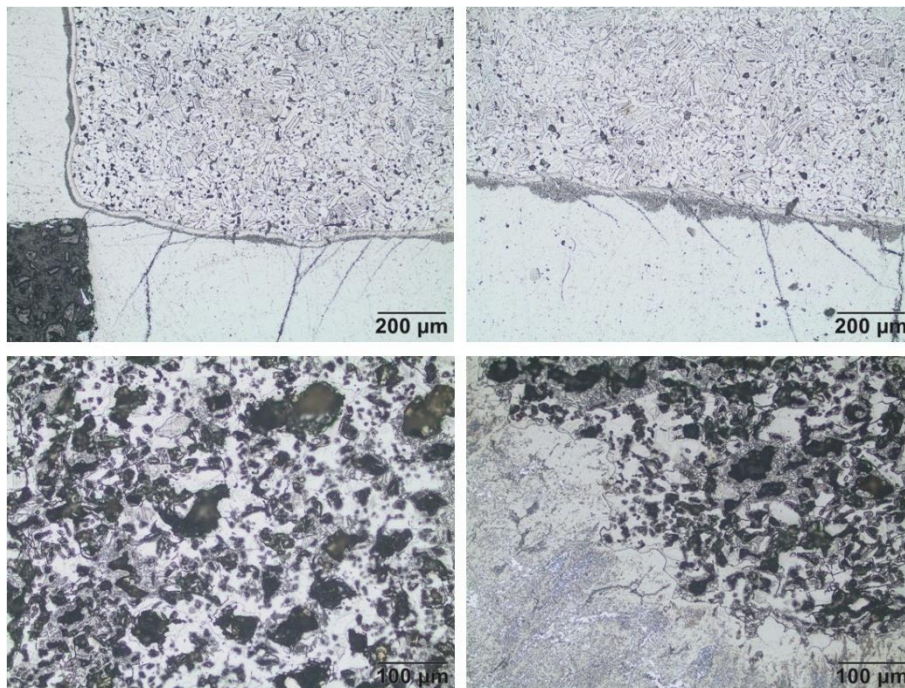


**Figure 67: Wrought Al disk (1200 °C sintered): CPTi+MA etched images (top left and right) with BE etched images (bottom left and right)**

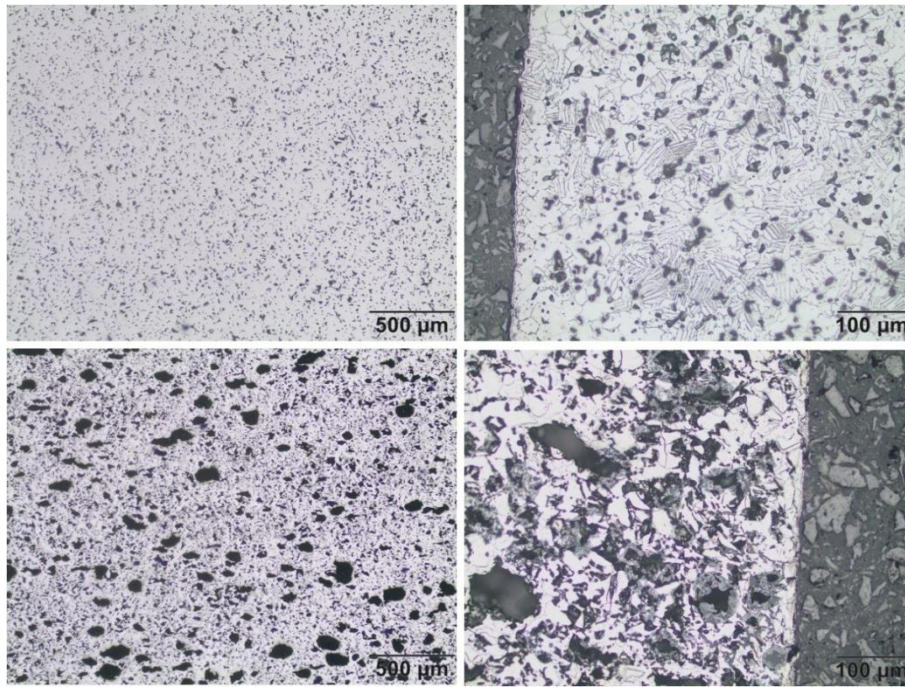


**Figure 68: Wrought Al disk (1100 °C sintered): CPTi+MA image (top left) and etched image (top right) with BE image (bottom left) and etched image (bottom right)**

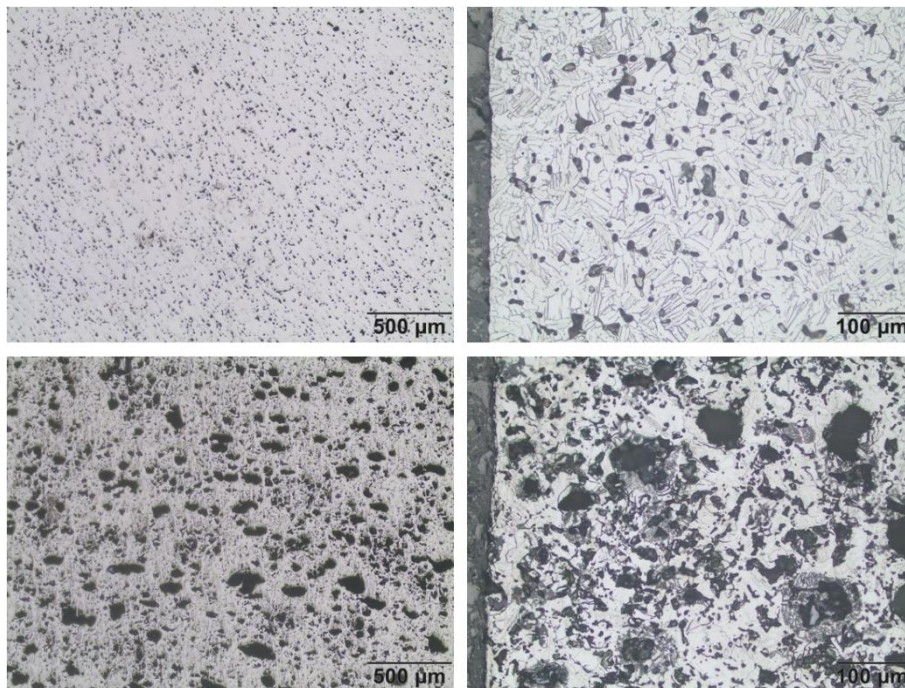


**Figure 69: Wrought Al disk (1100 °C sintered): CPTi+MA image (top left) and etched image (top right) with BE image (bottom left) and etched image (bottom right)**

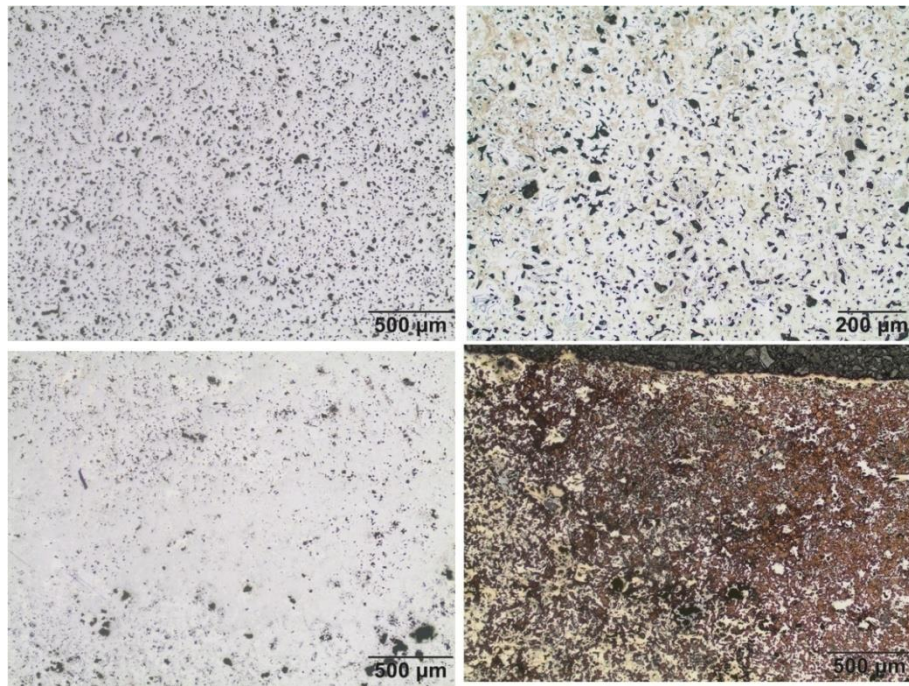


**Figure 70: Cu infiltrated (1100 °C sintered): CPTi+MA image (top left) and etched image (top right) with BE image (bottom left) with etched image (bottom right)**

## Appendix C: Diffusion graphs

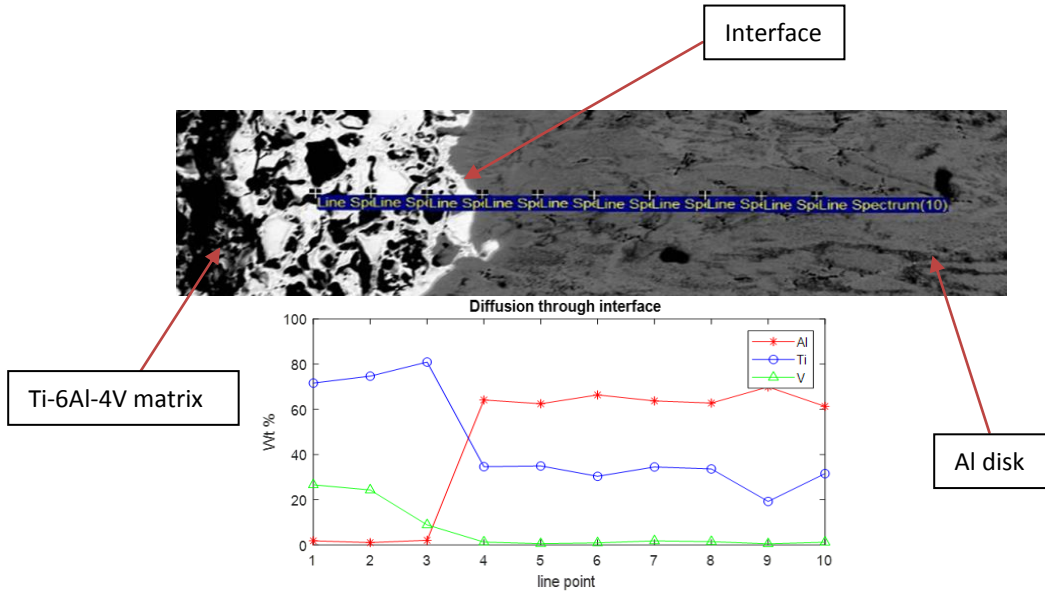


**Figure 71: Diffusion graph of BE sample after infiltration at 900 °C sintered at 1200 °C**

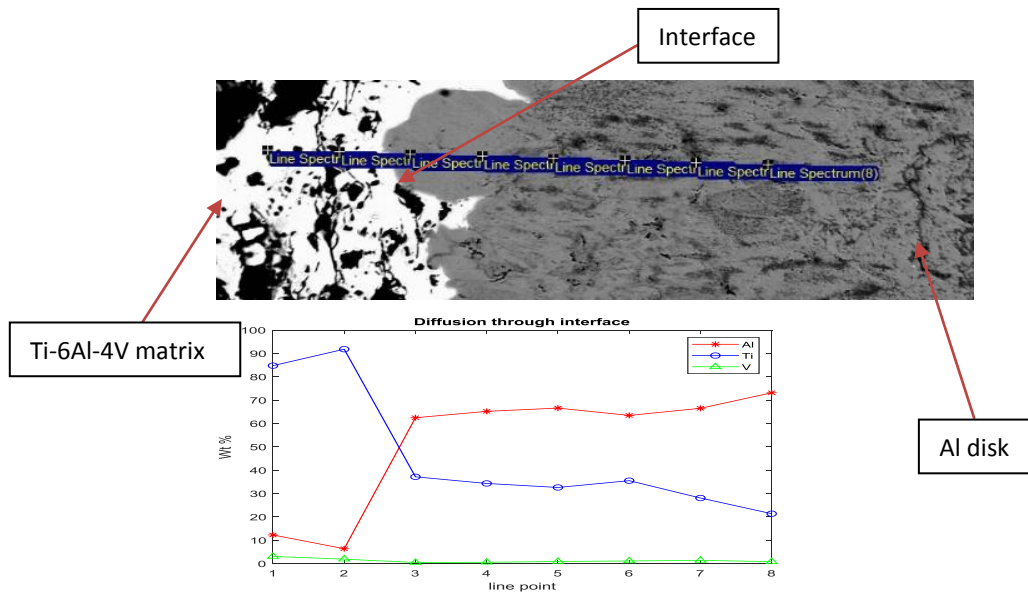


**Figure 72: Diffusion graph of BE sample after infiltration at 900 °C sintered at 1200 °C**

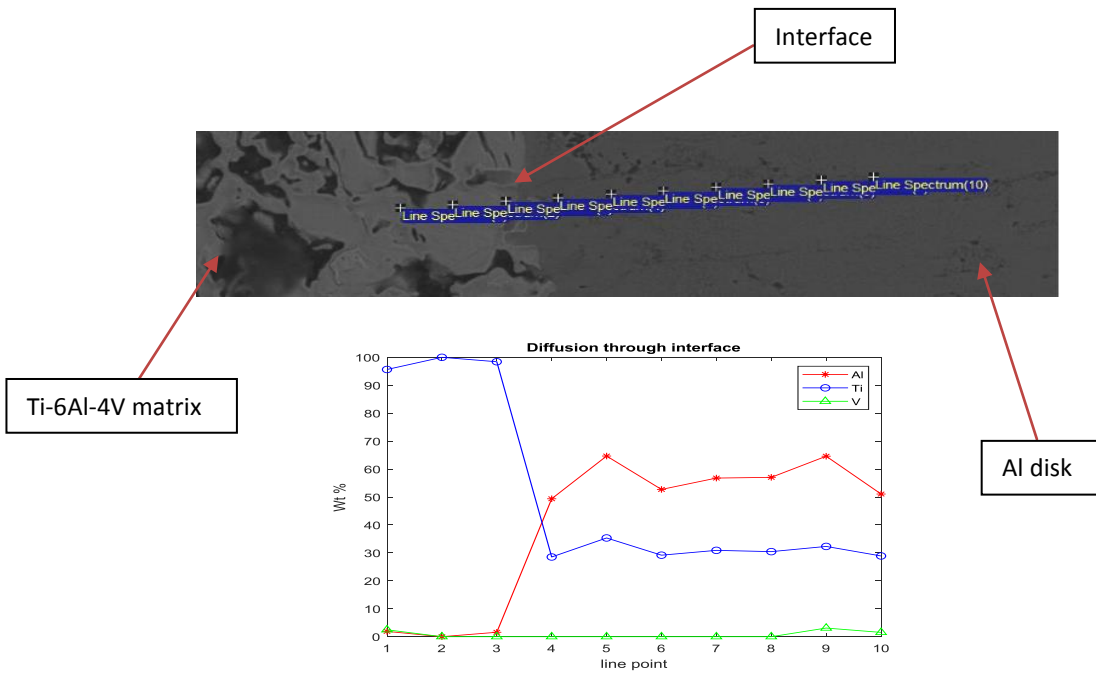


**Figure 74: Diffusion graph of BE sample after infiltration at 900 °C sintered at 1100 °C**

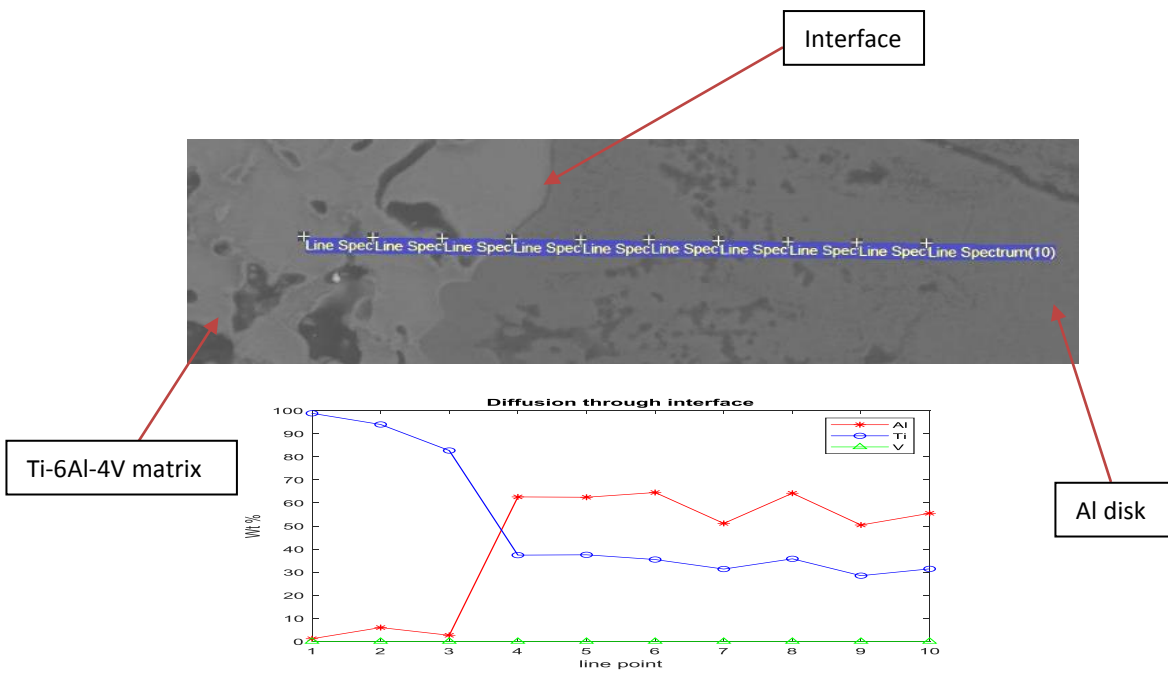


**Figure 73: Diffusion graph of BE sample after infiltration at 900 °C sintered at 1100 °C**

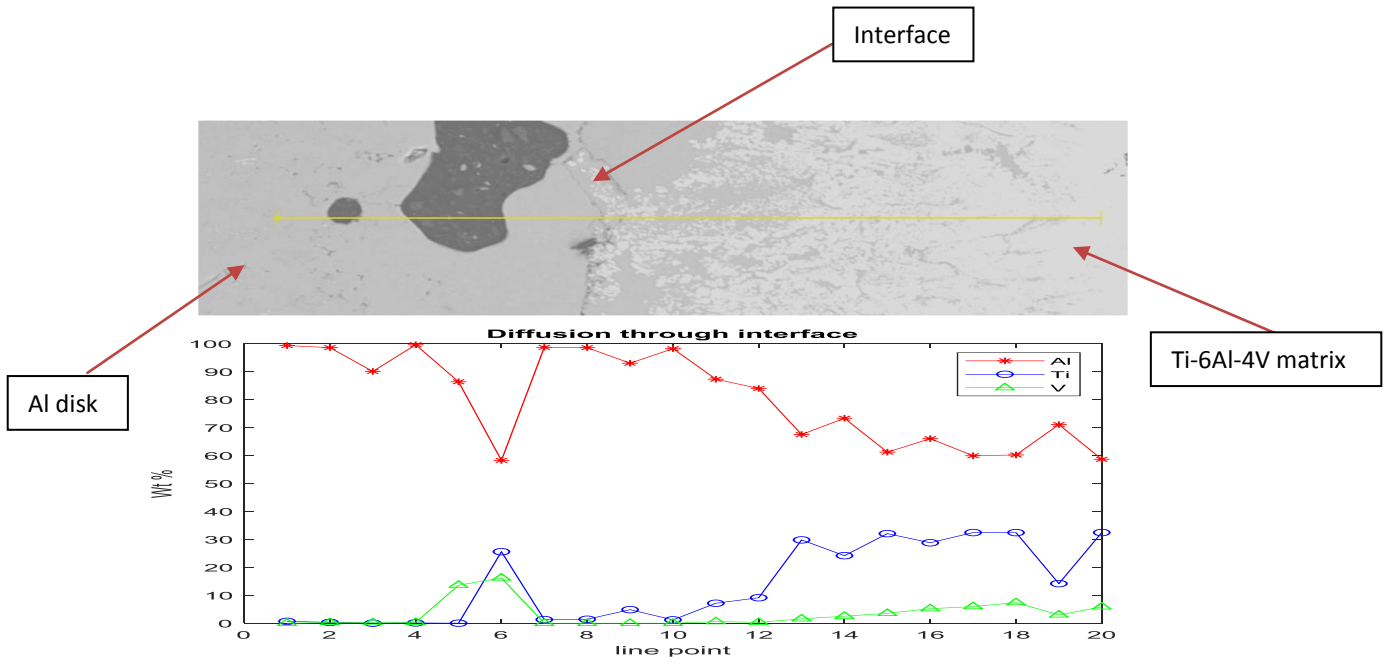


**Figure 75: Diffusion graph of BE sample after infiltration at 900 °C sintered at 1100 °C**

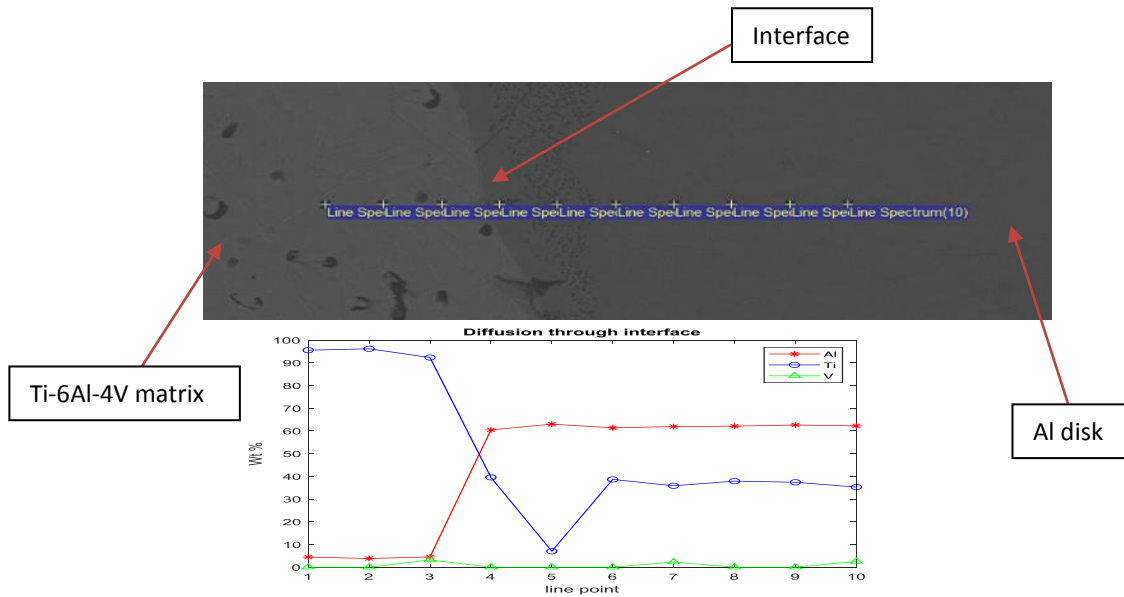


**Figure 76: Diffusion graph of MA sample after infiltration at 900 °C sintered at 1200 °C**

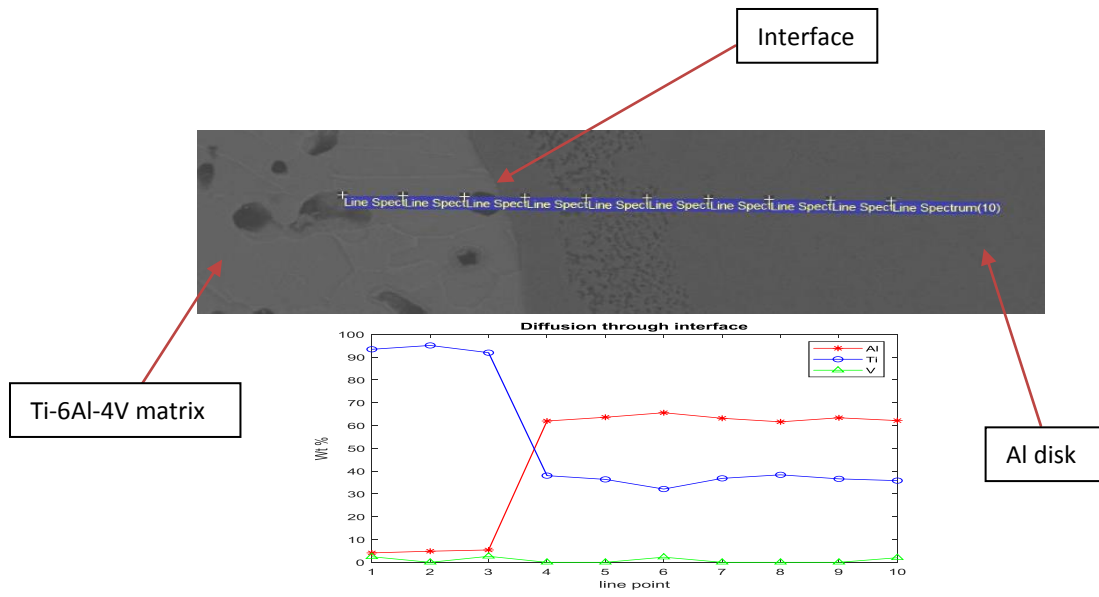


**Figure 77: Diffusion graph of MA sample after infiltration at 900 °C sintered at 1200 °C**

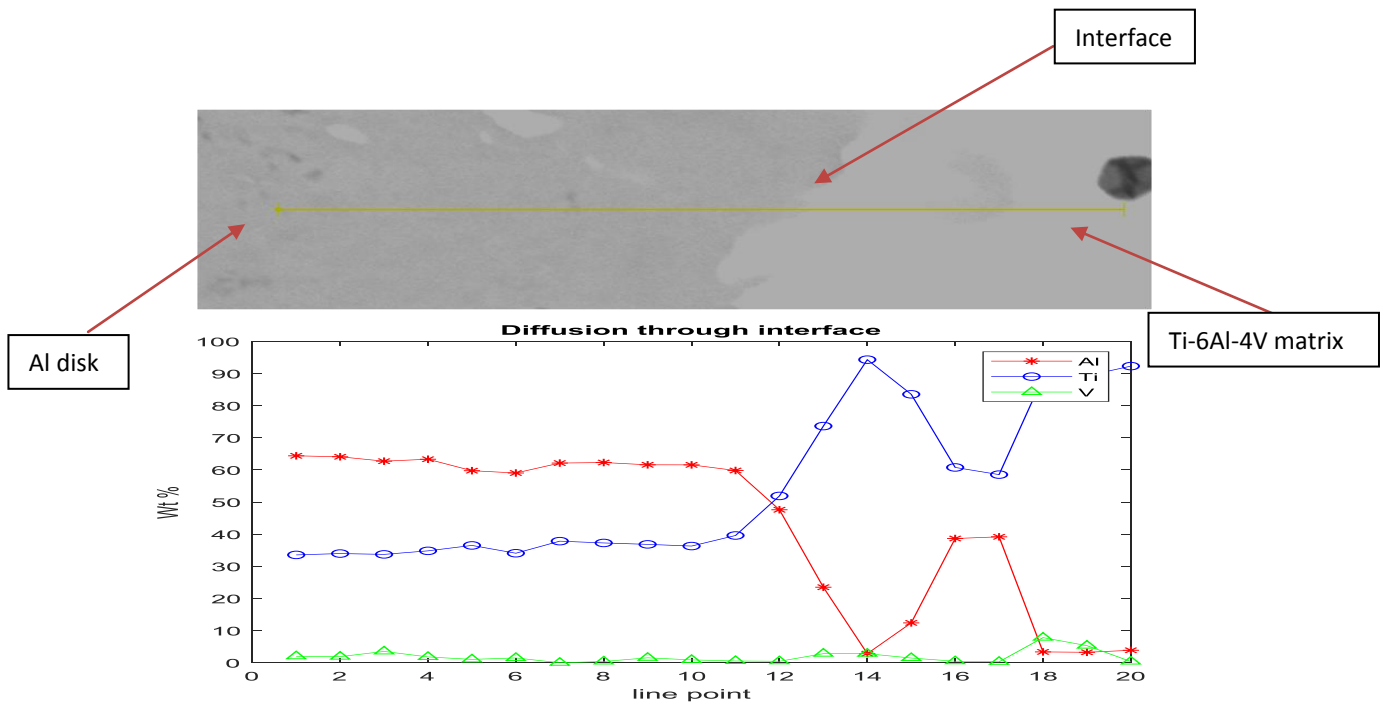


**Figure 78: Diffusion graph of MA sample after infiltration at 900 °C sintered at 1100 °C**